

**Piezo-sensors for in-situ boundary layer monitoring on morphing wings
Development, validation and implementation**

Stuber, V.L.

DOI

[10.4233/uuid:88181e83-edb5-4ed1-ae02-de119786ffbb](https://doi.org/10.4233/uuid:88181e83-edb5-4ed1-ae02-de119786ffbb)

Publication date

2021

Document Version

Final published version

Citation (APA)

Stuber, V. L. (2021). *Piezo-sensors for in-situ boundary layer monitoring on morphing wings: Development, validation and implementation*. [Dissertation (TU Delft), Delft University of Technology].
<https://doi.org/10.4233/uuid:88181e83-edb5-4ed1-ae02-de119786ffbb>

Important note

To cite this publication, please use the final published version (if applicable).
Please check the document version above.

Copyright

Other than for strictly personal use, it is not permitted to download, forward or distribute the text or part of it, without the consent of the author(s) and/or copyright holder(s), unless the work is under an open content license such as Creative Commons.

Takedown policy

Please contact us and provide details if you believe this document breaches copyrights.
We will remove access to the work immediately and investigate your claim.

Propositions

accompanying the dissertation

PIEZO-SENSORS FOR IN-SITU BOUNDARY LAYER MONITORING ON MORPHING WINGS

DEVELOPMENT, VALIDATION AND IMPLEMENTATION

by

Vincent Leo STUBER

1. The electrical conductivity of the polymer matrix plays a vital role in the poling efficiency of piezoelectric composites resulting in different d_{33} values for nominal comparable systems. (Chapter 2)
2. Lead-free piezoelectric composites, when specifically tailored to the application, are capable of replacing state-of-the-art lead-based piezoelectric ceramics. (Chapter 3)
3. The high g_{33} of typical piezoelectric polymer composites can only be utilized if the composite possesses a significant capacitance. (Chapter 4 & 5)
4. The benefit of spanwise distributed morphing surfaces on a typical wing is best utilized when present near the tip of the wing rather than at the root. (Chapter 7)
5. Preparing a batch of lithium doped sodium potassium niobate (KLN) piezo particles with consistent properties depends on countless variables, including stoichiometry, lab humidity and the sleeping position of Tygo¹.
6. The main reason for the development of lead-free piezoelectric materials is the prevention of poisonous waste.
7. A true democracy requires a ban on all political party related advertisement, as otherwise elections are nothing more than a high-school popularity contest.
8. While the aim of social media is to connect people, its contribution to unrealistic expectations and self-doubt actually has an isolating effect.
9. There is no relation between the size of a sensor and the richness of the information it can provide.
10. The ability to meet a set deadline has everything to do with knowing what you cannot do within that period of time.

These propositions are regarded as opposable and defensible, and have been approved as such by the promoters Prof. dr. ir. S. van der Zwaag and Dr. ir. R. De Breuker.

¹Tygo is my cat, who has plenty of sleeping positions at his disposal.

Stellingen

behorende bij het proefschrift

PIEZO-SENSORS FOR IN-SITU BOUNDARY LAYER MONITORING ON MORPHING WINGS

DEVELOPMENT, VALIDATION AND IMPLEMENTATION

door

Vincent Leo STUBER

1. De elektrische geleiding van een polymeren matrix speelt een belangrijke rol bij de efficiëntie van het polen van piëzo-elektrische composieten, met verschillende d_{33} waarden voor nominaal gelijkwaardige systemen tot gevolg. (Hoofdstuk 2)
2. Loodvrije piëzo-elektrische composieten kunnen loodhoudend piëzo-elektrisch keramiek van de hoogste kwaliteit vervangen mits ze specifiek ontwikkeld zijn voor een bepaalde toepassing. (Hoofdstuk 3)
3. De hoge g_{33} waarde van een doorsnee piëzo-elektrisch composiet komt alleen tot zijn recht als het composiet over een significante capaciteit beschikt. (Hoofdstuk 4 & 5)
4. Het voordeel van vervormbare besturingsvlakken die over de spanwijdte van een doorsnee vleugel zijn verdeeld is groter als deze geplaatst zijn aan het uiteinde in plaats van bij de wortel van de vleugel. (Hoofdstuk 7)
5. Het produceren van lithium gedoteerd natrium kalium niobaat (KNLN) piëzo-deeltjes met consistente eigenschappen hangt af van verschillende variabelen, zoals stoïchiometrie, luchtvochtigheid in het lab en de slaaphouding van Tygo¹.
6. De enige reden voor het ontwikkelen van loodvrije piëzo-elektrische materialen is het voorkomen van giftig afval.
7. Een ware democratie vereist dat alle reclame van politieke partijen wordt verboden, omdat de verkiezingen anders niets meer zijn dan een schoolse populariteitswedstrijd.
8. Ondanks dat sociale media beogen om mensen te verbinden, dragen ze bij aan onrealistische verwachtingen en een laag zelfbeeld, hetgeen mensen juist isoleert.
9. Er is geen relatie tussen het formaat van een sensor en de rijkheid aan informatie die deze kan leveren.
10. De mogelijkheid om een deadline te halen, heeft alles te maken met het bewust zijn van wat je binnen de gestelde tijd niet kunt doen.

Deze stellingen worden opponeerbaar en verdedigbaar geacht en zijn als zodanig goedgekeurd door de promotors Prof. dr. ir. S. van der Zwaag en Dr. ir. R. De Breuker.

¹Tygo is mijn kat, die over talloze slaaphoudingen beschikt.

PIEZO-SENSORS FOR IN-SITU BOUNDARY LAYER MONITORING ON MORPHING WINGS

DEVELOPMENT, VALIDATION AND IMPLEMENTATION



PIEZO-SENSORS FOR IN-SITU BOUNDARY LAYER MONITORING ON MORPHING WINGS

DEVELOPMENT, VALIDATION AND IMPLEMENTATION

Proefschrift

ter verkrijging van de graad van doctor
aan de Technische Universiteit Delft,
op gezag van de Rector Magnificus prof. dr. ir. T. H. H. J. van der Hagen,
voorzitter van het College voor Promoties,
in het openbaar te verdedigen op vrijdag 29 oktober 2021 om 10:00 uur

door

Vincent Leo STUBER

Ingenieur Luchtvaart en Ruimtevaart,
Technische Universiteit Delft, Delft, Nederland,
geboren te Amersfoort, Nederland.

Dit proefschrift is goedgekeurd door de

promotor: Prof. dr. ir. S. van der Zwaag

promotor: Dr. ir. R. De Breuker

Samenstelling promotiecommissie:

Rector Magnificus

voorzitter

Prof. dr. ir. S. van der Zwaag

Technische Universiteit Delft

Dr. ir. R. De Breuker

Technische Universiteit Delft

Onafhankelijke leden:

Dr. M. Kotsonis

Technische Universiteit Delft

Prof. dr. C. A. Randall

Pennsylvania State University

Prof. dr. ir. L. L. M. Veldhuis

Technische Universiteit Delft

Prof. dr. H. G. C. Werij

Technische Universiteit Delft

Prof. dr. ir. J. W. van Wingerden

Technische Universiteit Delft



Keywords: Piezoelectric materials, Laminar-to-turbulent transition, Sensors

Printed by: IPSKAMP Printing B.V.

Cover by: Vincent Leo Stuber

Copyright © 2021 by V. L. Stuber

ISBN 978-94-6421-490-1

An electronic version of this dissertation is available at

<http://repository.tudelft.nl/>.

CONTENTS

1	Introduction	1
1.1	Piezoelectrics	2
1.1.1	The piezoelectric effect	2
1.1.2	Piezoelectric materials.	6
1.1.3	Piezoelectric sensors.	8
1.2	Boundary layers on airfoils	9
1.2.1	Boundary layer states	9
1.2.2	Measurement techniques	10
1.3	Thesis outline	12
2	The effect of the intrinsic electric matrix conductivity on the piezoelectric charge constant of piezoelectric composites	15
2.1	Introduction	16
2.2	Fabrication of 0-3 particulate composites.	18
2.3	Results & discussion	20
2.3.1	Dielectric constant.	20
2.3.2	Piezoelectric charge constant	22
2.3.3	Hysteresis loop measurements.	24
2.3.4	The effect of humidity	27
2.4	Conclusions.	29
	Appendices	31
2.A	Polydimethylsiloxane (PDMS).	31
3	Flexible lead-free piezoelectric composite materials for energy harvesting applications	35
3.1	Introduction	36
3.2	Fabrication of aligned knln/pdms composites	39
3.2.1	Preparation of knln fibers	39
3.2.2	Dielectrophoretic alignment of knln fibers.	40
3.3	Piezoelectric constants of aligned knln/pdms composites	42
3.4	Comparison of piezoelectric materials	45
3.5	Conclusions.	49
4	Piezoelectric sensor patch to detect laminar-to-turbulent transition on airfoils	51
4.1	Introduction	52
4.2	Method	52
4.2.1	Piezoelectric sensors.	53
4.2.2	Wind tunnel experiments	54

4.2.3	Data validation.	55
4.3	Results and discussion	56
4.3.1	Static angle of attack measurements	57
4.3.2	Dynamic angle of attack measurements	59
4.4	Conclusions and recommendations	60
Appendices		63
4.A	Pyroelectric Effect.	63
4.B	Pyroelectric Patch.	64
5	Boundary layer state detection using a piezoelectric sensor	67
5.1	Introduction	68
5.2	Method	70
5.2.1	Piezoelectric sensors.	70
5.2.2	Experimental setup	72
5.2.3	Test cases	73
5.3	Results	74
5.3.1	Piezoelectric data	74
5.3.2	Statistical velocity fields	76
5.4	Discussion	78
5.4.1	Boundary layer state from PIV	78
5.4.2	Detection of boundary layer fluctuations	80
5.4.3	How to read the piezoelectric sensor.	84
5.5	Conclusions.	86
Appendices		87
5.A	Composite Bimorph	87
6	Overview of the SmartX wing technology integrator	91
6.1	Introduction	92
6.2	SmartX philosophy	93
6.3	SmartX enabling technologies	95
6.3.1	Trailing edge slow morphing	95
6.3.2	Trailing edge fast morphing	97
6.3.3	Fiber-optic shape sensing	98
6.3.4	Boundary layer sensor	100
6.4	SmartX technology integration	102
6.4.1	Morphing module and actuator system integration	103
6.4.2	Sensor system integration	104
6.4.3	Software and data integration	104
6.4.4	Control system integration.	105
6.5	Summary and conclusions	105
7	In-situ boundary layer transition detection on multi-segmental (a)synchronous morphing wings	107
7.1	Introduction	108
7.2	Experimental setup	110
7.2.1	Hardware setup	110

7.2.2	Piezoelectric signal interpretation	113
7.2.3	The database.	115
7.2.4	Experimental program.	117
7.3	Results & discussion	118
7.3.1	Transition under zero morphing conditions	118
7.3.2	Transition shifting during synchronous morphing	119
7.3.3	Transition during asynchronous spanwise morphing	120
7.4	Conclusions.	126
8	Conclusions and recommendations	129
8.1	Conclusions.	129
8.2	Recommendations for future work	131
	Summary	133
	Samenvatting	137
	References	141
	Acknowledgements	153
	Curriculum Vitæ	157
	List of Publications	159
	Nomenclature	161



1

INTRODUCTION

During the last century the focus in the design of the shape of aircraft wings has been on maximizing the fuel efficiency during cruise flight. Because of the vastly different flight conditions during other flight phases, control surfaces such as flaps are required to extend the flight envelope to these flight phases as well. However, during these flight phases, such a wing will perform less efficiently, which means a higher fuel consumption and/or more noise pollution. Morphing wings, which are wings capable of adapting their shape in-flight, are a potentially better solution. Various morphing techniques exist, such as sweep, camber, span, twist or pitch morphing, or combinations of these [1–4]. Because of their ability to change shape, morphing wings can make a single aircraft perform more efficiently at an extended range of flight conditions (relevant to commercial aircraft), or can increase the maneuverability (relevant to military aircraft). However, morphing wings generally also entail higher costs due to added complexity and structural weight.

The *SmartX* project, initiated at the Aerospace Engineering faculty of the Delft University of Technology (TUD), aims to set a significant step towards making morphing wings a reality. The main objective of SmartX is the integration of smart sensing, smart actuation and smart control into a single hardware demonstrator, with the purpose of achieving the following sub-objectives: drag reduction, load alleviation, aeroelastic stability control and lift control [5]. This dissertation contributes to the first sub-objective: drag reduction. This entails wing shape optimization to fly at minimum drag during various flight phases. The total drag depends on the induced drag and profile drag. Induced drag occurs when an object changes the direction of the incoming airflow, while profile drag can be subdivided into pressure drag, which occurs due to the pressure difference over the entire object, and friction drag. The latter is dictated by the boundary layer flowing around the wing, which can either be laminar or turbulent. While a wing will always experience both types of flow, a larger fraction of laminar flow is preferred as a laminar flow causes a lower skin friction drag compared to turbulent flow. A morphing wing is capable of moving the location of laminar-to-turbulent transition, and thus is

capable to control (to a certain extent) the portion of laminar flow on the wing. A control loop build into the morphing wing can actively push transition towards the trailing edge (TE) of the wing, and thus reduce the total skin friction drag, provided it has the current location of transition as one of its input parameters. Therefore, a smart sensing system is required that is capable of detecting the state of the boundary layer.

This thesis focuses specifically on the development, validation and implementation of such a novel sensor systems installed in the SmartX wing: piezoelectric flow sensors. The aim is to design a sensor system which is able to monitor the boundary layer on the suction side (topside) of the wing, thereby providing information on where laminar-to-turbulent transition takes place. In this work, piezoelectric materials were chosen as viable candidates because of their ability for direct mechanical-to-electrical conversion and high frequency bandwidth. Such materials are quite commonly used in demanding high-tech responsive applications, and over the last few decades also the interest of the aerospace industry has grown for applications such as structural health monitoring and energy harvesting [6–8].

In order to arrive at a functional design of the piezoelectric flow sensors, knowledge about piezoelectric materials and boundary layers surrounding airfoils is required. Both these topics are briefly discussed in this chapter.

1.1. PIEZOELECTRICS

This section briefly dives into details about the piezoelectric effect (1.1.1), provides an overview of typical piezoelectric materials (1.1.2) and discusses how to use piezoelectric materials as sensor materials (1.1.3).

1.1.1. THE PIEZOELECTRIC EFFECT

Parking sensors, fuel injection systems, gas lighters, sonars, and accelerometers, all these applications rely on the phenomenon referred to as the piezoelectric effect. This effect was discovered in 1880 by the French physicists Jacques and Pierre Curie. They discovered that while pressing on certain crystals, such as quartz or tourmaline, these crystals were able to generate an electric charge. Most *piezoelectric* materials used today are *ferroelectric* materials. This is a sub-group of *pyroelectric* materials, which in turn is a sub-group of piezoelectric materials, as shown in Fig. 1.1. This section will briefly explain these three terms.

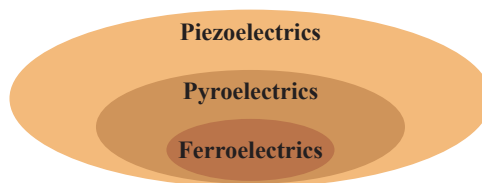


Figure 1.1: Ferroelectrics are a sub-group of pyroelectrics, which in turn are a sub-group of piezoelectrics.

PIEZOELECTRICITY

Piezoelectricity occurs in non-centrosymmetrical, non-conducting (poly)crystalline materials. Non-centrosymmetrical means that there is a repeating order of atoms in that material which does *not* have a point of symmetry at the center of each repeating block [9]. By applying a force, F , to such a material, the deformation of the material results in a dipole moment. This occurs because the electrical charges of the individual atoms in the material do not cancel out in a non-centrosymmetrical material. The created dipole moment results in one side of the material to be slightly positively charged, while the other is slightly negatively charged. By applying electrodes to the charged surfaces, this potential difference can be measured. This is called the *direct* piezoelectric effect; the generation of an electric field upon an applied force. This is visualized in Fig. 1.2. However, the charged outer surfaces will attract free charges such as electrons or ions from the surrounding environment, which will cancel out the created positive and negative charges on the outer surfaces of the sample. Therefore, the measured potential difference will not be maintained under a static force. The electric displacement, or electric charge per unit area, D , which occurs on such a material can be calculated using the following equation:

$$D = dT + \epsilon^T E \tag{1.1}$$

In here, d represents the piezoelectric charge constant, T the applied mechanical stress, ϵ^T the permittivity under constant stress, and E the applied electric field.

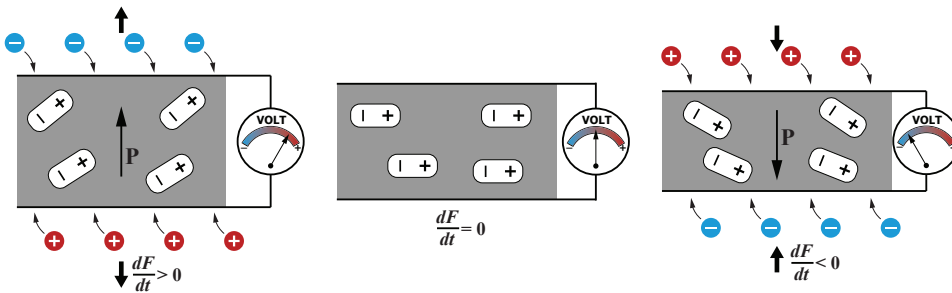


Figure 1.2: Visualization of the piezoelectric effect. While a change in applied force, F , is experienced, a dipole moment, P , is created. Shortly after applying the force, the created dipole gets canceled by the attraction of free ions and electrons.

The piezoelectric effect also works the other way around, which in that case is called the *converse* piezoelectric effect. By applying an electric field to the piezoelectric material its dipole moment is forced to change, which results in an elastic deformation of the material. In this case, the material can be used as an actuator. The generated strain, S , can be calculated using the following equation:

$$S = s^E T + dE \tag{1.2}$$

In here, s^E is the material compliance under constant electric field.

In both equations the *piezoelectric charge constant*, \mathbf{d} , is the material property describing the magnitude of the piezoelectric effect. Normally it is given in the form d_{ij} , in which i and j range from 1 to 6 indicating the direction of the electric field and mechanical deformation respectively, while the polarization direction is always in the 3 direction. Most commonly used is d_{33} , which means that the electric field, mechanical deformation and polarization direction all act in the same direction. It is given in either CN^{-1} for the direct effect, or in mV^{-1} for the converse effect. Another noteworthy parameter is the *piezoelectric voltage constant*, g_{ij} , which describes the output voltage per applied force of a piezoelectric material, specifically for sensor applications, given in VmN^{-1} . It can be calculated using the following equation:

$$g_{ij} = (\epsilon^T)^{-1} d_{ij} \quad (1.3)$$

PYROELECTICITY

A subclass of piezoelectric materials are pyroelectric materials. In these materials spontaneous polarization occurs. This means that even while no force is applied a dipole moment is created, and thus free electrons and ions already sit on the outer surface of the crystal even while $dF/dt = 0$. However, to generate an electric field, a temporary change of the dipole moment is still required. The main difference between purely piezoelectric materials and materials which are both piezoelectric and pyroelectric, is that pyroelectric materials do not only respond to a change of applied force, but also to a change of applied temperature [10]. Increasing the temperature in such materials generally increases the entropy, which in turn decreases the dipole moment. A change of temperature is required, just like a change of applied stress, in order to generate an electric field. The pyroelectric effect can also have contributions from the piezoelectric effect if the piezoelectric material is not clamped, i.e. free to expand or shrink. The material will expand or shrink as a result of the applied temperature, thereby triggering the piezoelectric effect as well. Therefore, the pyroelectric effect is generally quantified into two constants; one concerning the purely pyroelectric response, and one concerning the system induced piezoelectric contribution.

Since most piezoelectric materials are also pyroelectric, piezoelectric sensors might be hard to use in temperature unstable environments. A way of dealing with this is to use a series bimorph, which intrinsically cancels the pyroelectric effect. Such a bimorph consists of two layers of piezoelectric material glued together with their polarization direction opposing each other. This is visualized in Fig. 1.3. If the temperature changes, assuming both piezoelectric elements experience the same temperature change, the net dipole moment stays constant. This happens because the dipole moment in both piezoelectric elements change the same amount in opposite direction. The piezoelectric effect can still be used if one of the piezoelectric elements is in compression and the other in tension. This can for instance be achieved by clamping one end of the bimorph and applying a force perpendicular to the bimorph to the other end. This causes one of the dipoles to increase while the other decreases, changing the net dipole of the bimorph, generating an electric field. This type of mechanical boundary condition also acts as mechanical amplifier, increasing the piezoelectric output significantly in

comparison to a clamped disk configuration [11].

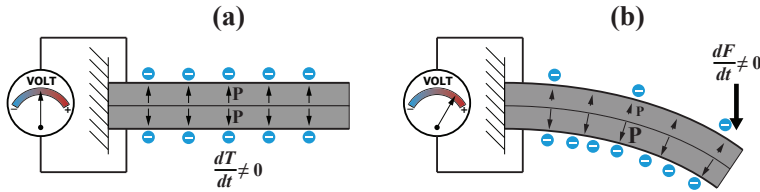


Figure 1.3: Working principle of a series bimorph. (a) When changing temperature, the polarization of both piezoelectric elements changes equally, canceling the pyroelectric effect. (b) Using the correct mechanical boundary conditions, an applied force results in one piezoelectric element in compression and one in tension, which results in a change of the net dipole moment.

FERROELECTRICITY

Up until this point we assumed that the polarization throughout the whole material aligns in the same direction. While this can be true for single crystal materials like quartz, polycrystalline ceramics do not have this feature. The dipole moments of each grain in such a material are randomly orientated, meaning that the net dipole moment is zero. Some of these materials are classified as ferroelectric materials, which are materials in which the spontaneous electric polarization can be reoriented between possible equilibrium directions by application of a high enough electric field [12]. This process is called *poling*, which is the application of a high electric field upon which the dipole moments align. These materials were discovered about 100 years ago [13].

Fig. 1.4 shows a typical hysteresis loop of a ferroelectric material. It shows the overall polarization, P , versus the applied electric field, E . Before poling, the polarization is zero at zero applied field. By applying a sufficiently high electric field, the polarization increases until the saturated polarization, P_s , is reached. The individual dipoles in the material are now aligned to the highest degree possible, providing the highest overall polarization. When the electric field is now removed, the polarization decreases only slightly down to the remnant polarization, P_r . This means that some grains lose their ideal dipole orientation, which happens due to internal stresses. However, most orientations remain, providing a significant overall polarization. The polarization direction can also be changed by applying a similar electric field in the opposite direction, providing the same magnitude of polarization in the opposite direction.

To return back to the unpoled state with zero polarization, the piezoelectric material has to be heated to above its Curie temperature, T_c . Above this temperature all polarization in the material is lost, because the material loses its non-centrosymmetrical structure. Cooling back down from this temperature returns the polarization of each individual grain, but once again each of these is randomly orientated. In order to align the dipoles of the individual grains again, the material should be re-poled.

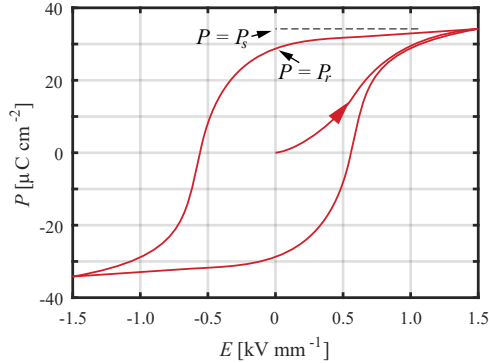


Figure 1.4: Typical hysteresis loop of ferroelectric materials, plotting the polarization, P , versus the electric field, E . This is a modified version of a figure from Holterman and Groen 2013 [9].

1.1.2. PIEZOELECTRIC MATERIALS

This section briefly discusses the most widely used piezoelectric materials, rigid and brittle piezoelectric ceramics, and provides information about the alternative of flexible and ductile materials; piezoelectric polymers. In addition, piezoelectric composites are introduced that combine the benefits of both ceramics and polymers.

PIEZOELECTRIC CERAMICS

Because of their excellent piezoelectric properties, the vast majority of piezoelectric materials used today are piezoelectric ceramics. Ceramics are polycrystalline materials, consisting of single crystals baked together into one material through a process called sintering.

The most popular piezoelectric ceramic is lead zirconate titanate (PZT), $PbZr_xTi_{1-x}O_3$ [14, 15]. Using a specific composition of zirconium and titanium, PZT can be manufactured right at its morphotropic phase boundary (MPB). This is a composition at which multiple phases co-exist, which increases the number of possible poling directions [16, 17]. Therefore, near the MPB the piezoelectric properties, such as the piezoelectric charge constant, d_{33} , reach peak values, typically in the range of 200 to 800 pC N^{-1} . In addition to the high d_{33} value, the T_c of PZT is in the range of 160 to 360 $^{\circ}\text{C}$, making it possible to use this material in a wide range of applications at room temperature or elevated temperatures. It is therefore no wonder that this material is currently the most widely used piezoelectric ceramic. However, there is one major drawback of PZT: it contains a significant amount of the toxic substance lead. Because of this, PZT is classified as a Substance of Very High Concern (SVHC) by the European Community REACH in 2006.

Barium titanate (BT), $BaTiO_3$, is a lead-free material which is one of the most studied piezoelectric ceramics [18]. The d_{33} of BT is typically around 190 pC N^{-1} . However, the main drawback of this material is its limited T_c , which is about 120 $^{\circ}\text{C}$. As a rule of thumb, piezoelectric materials can be used up to about half their T_c (when expressed in

degrees Celsius) in order to prevent depolarization to occur, which limits the application of BT.

The toxicity of PZT and limitations of BT have led to a significant amount of research into lead-free alternatives. Most promising candidates are based on either potassium sodium niobate (KNN), $K_xNa_{1-x}NbO_3$, or bismuth sodium titanate (BNT), $Bi_{0.5}Na_{0.5}TiO_3$ [19–22]. Ever since the work of Saito et al. in 2004, great interest into KNN-based materials was triggered since they were able to show a high d_{33} in combination with a high T_c [23]. Instead of relying on a MPB as is the case in PZT-based materials, KNN-based materials rely on a polymorphic phase transition (PPT), which is a temperature dependent phase boundary where multiple phases exist [24]. Note that a PPT is less ideal as a MPB, as the properties depend on temperature instead of material composition. This means that those materials are ideally used at one specific temperature. Doping KNN-based materials with lithium has proven to be an effective way to lower the PPT to room temperature, while also increasing T_c to over 400 °C. This way, the peak in piezoelectric properties occurs at room temperature, with a d_{33} in the range of 200 to 400 pC N⁻¹ [24]. While this material seems promising, a major drawback is its moisture sensitivity [25].

PIEZOELECTRIC POLYMERS

Although piezoelectric ceramics have excellent piezoelectric properties, they are also brittle and therefore can not be used in applications undergoing large elastic deformations. Piezoelectric polymers on the other hand are flexible, which makes them more robust and usable in, for instance, flexible electronics.

Polyvinylidene-fluoride (PVDF) and its copolymers are the most well-known piezoelectric polymers due to its relatively strong piezoelectric response, yielding a d_{33} value of about 20 to 25 pC N⁻¹ [26–29]. They have the ability to create a dipole moment by aligning the fluorine atoms in its chain in the crystalline parts of the polymer. While the d_{33} of PVDF is relatively low compared to piezoelectric ceramics, their ϵ is also lower. This provides them with a strong g_{33} value of around 200 mV m N⁻¹, which is much higher compared to typical ceramics with a g_{33} value of around 25 mV m N⁻¹. However, major drawbacks of PVDF are the limited T_c , which lies around 100 °C, and the high required poling field of around 60 kV mm⁻¹.

PIEZOELECTRIC COMPOSITES

Another way to obtain effective piezoelectric materials is by combining a polymeric matrix with piezoelectric active ceramic filler particles, yielding piezoelectric composites [30–32]. The benefit of these composites is that their thermomechanical and piezoelectric properties can be tailored to the application. Flexible materials can be obtained by using low volume fractions of filler materials in combinations with an inert flexible polymer matrix, while a high T_c can be obtained by choosing a temperature resistant polymer in combination with a high T_c ceramic filler. To obtain significant piezoelectric properties one could either use a high particle volume fraction or align the particles in

thread-like microstructures [33]. Several studies have already shown that piezoelectric composites are excellent candidates for various, especially sensing, applications [34–39].

1.1.3. PIEZOELECTRIC SENSORS

As explained before, a charge can be created upon applying a force to a piezoelectric material. The created charge causes a voltage over the piezoelectric material, which is equal to the charge divided by the material capacitance. However, the generated current that comes with the voltage is normally low, in range of nA, making a piezoelectric material a high impedance source. This means that it is prone to electrostatic noise, and thus amplification is required in order to obtain a stable noise-insensitive signal [9]. Typically, this can be done either by a voltage amplifier or a charge amplifier, essentially directly measuring the voltage or charge generated by the piezoelectric material. Typical circuit diagrams of these measurement methods are shown in Fig. 1.5. The symbols given in the figure are explained in the next two paragraphs.

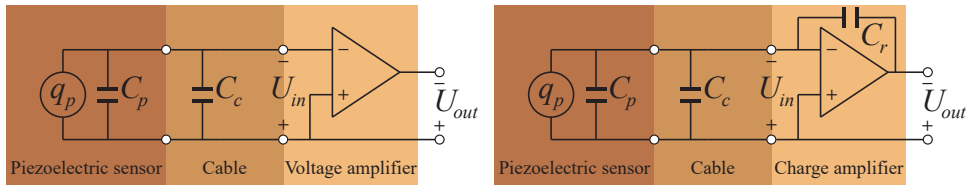


Figure 1.5: Typical circuit diagrams for voltage (left) and charge (right) measurements using piezoelectric sensors [9].

VOLTAGE MEASUREMENTS

The voltage created by the piezoelectric material is defined by the charge generated, q_p , divided by the capacitance of the piezoelectric material, C_p . This is essentially the piezoelectric voltage constant, g_{ij} , which was earlier defined in Equation 1.3. However, the voltage which arrives at the input of the voltage amplifier, U_{in} , also experiences the capacitance of the cables between the piezoelectric sensor and the voltage amplifier. Therefore, the total capacitance becomes the sum of C_p and the capacitance of the cables, C_c . Because of this, U_{in} defined as q_p divided by the sum of C_p and C_c , is lower than the voltage directly created by the piezoelectric sensor. The higher the value of C_c (i.e. the longer the cables), the lower U_{in} becomes. This is why voltage measurements always require the voltage amplifier to be close to the piezoelectric sensor. Finally, the gain of the voltage amplifier determines the value of the output voltage, U_{out} , defined by the values of the resistors of the amplifier.

CHARGE MEASUREMENTS

The charge generated by the piezoelectric sensor is in this case not defined by its own capacitance, but by the capacitor of the charge amplifier, C_r . The output voltage of the charge amplifier, U_{out} , therefore becomes the charge generated by the piezoelectric

material, q_p , divided by C_r . Since the value of C_r is fixed for a certain electronic circuit, U_{out} becomes directly a function of q_p , which essentially is the piezoelectric charge constant, d_{ij} . In this case, the cable capacitance, C_c , does not play a role. Due to the benefit of the cable length independency, charge measurements generally are the preferred measurement technique. The main reason to go for voltage measurements would be if the piezoelectric material has a relatively low d_{ij} but a high g_{ij} . This is the case in for instance quartz, piezoelectric polymers and (most) piezoelectric composites.

1.2. BOUNDARY LAYERS ON AIRFOILS

This section briefly shows how a boundary layer on the suction side of a typical airfoil behaves (1.2.1). The characteristics of its behavior specify the characteristics of the measurement techniques capable of measuring the different states of such a boundary layer, which are briefly introduced (1.2.2).

1.2.1. BOUNDARY LAYER STATES

A boundary layer on an airfoil can be defined as the layer of air surrounding the airfoil in which the air velocity increases from zero at the skin of the airfoil up until the boundary layer edge velocity, U_e , which is generally close to the free stream velocity, U_∞ . Typically, boundary layers can be divided into various states, as is shown in Fig. 1.6.

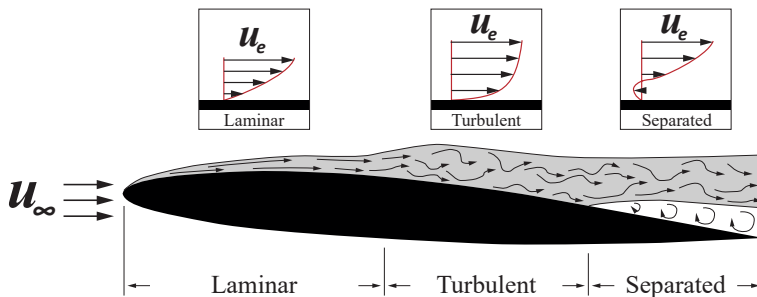


Figure 1.6: Typical states of the boundary layer on the suction side of an airfoil.

A *laminar* flow can be described as a flow containing non-intersecting parallel layers of air. As long as the flow is laminar, the boundary layer thickness is relatively thin, and a gradual increase of air velocity is observed from zero at the airfoil skin to U_e . A laminar flow typically provides the lowest amount of skin friction [40].

Moving downstream, instabilities in the flow start to appear. Because of this, at some point the non-intersecting nature of parallel layers of air is lost. A random chaotic flow takes its place, called a *turbulent* flow. The region in which a laminar flow changes into a turbulent flow is called *transition*. The boundary layer thickness of a turbulent flow is larger in comparison to a laminar flow, and a more steep increase in flow velocity is observed near the airfoil skin. Because of this a turbulent flow induces an increased skin

friction, and this causes a higher overall drag. Other changes in comparison to a laminar boundary layer are the increased heat transfer between the airfoil skin and airflow, and the presence of high frequency (kHz range) oscillations [41].

Under some conditions, while moving downstream even further, the flow can separate from the airfoil. In the separated regime the flow velocity near the airfoil skin actually moves in the opposite direction, accompanied by low frequency (Hz range) oscillations of the flow [42]. A separated flow causes a significant increase in pressure drag, as the pressure differential between the front and rear of the airfoil has increased. This makes a separated flow an unwanted phenomenon since the overall lift-to-drag ratio is significantly reduced. In some cases, separation can also occur directly from a laminar flow. In such a case, the flow could go through laminar-to-turbulent transition after it has separated. Since a turbulent flow has a stronger driving force to stay attached to an airfoil due to enhanced mixing in the boundary layer, it might return back to the airfoil skin as a turbulent flow. If that happens, there is a separated region between the laminar and turbulent flows which is called a Laminar Separation Bubble (LSB) [43]. While a LSB is not as critical as an actual separated flow, it still decreases the overall lift-to-drag ratio of the airfoil. However, problems can arise when these bubbles start to burst, which can occur due to an unstable angle of attack, α , which is the angle between the airfoil chord line and the free stream, or fluctuating air velocities. This can lead to large separated zones or complete separation.

In the case of a fixed airfoil under constant conditions, the location of transition and separation strongly depend on α . Increasing α generally moves transition and separation towards the leading edge (LE) of the airfoil. A similar but smaller forward shift occurs upon increasing the free stream velocity, U_∞ .

1.2.2. MEASUREMENT TECHNIQUES

The measurement techniques presented in this section are subdivided into typical laboratory environment measurements, in which the instrumentation is physically separated from the wing, and measurements which can be performed by sensors installed into the wing (in-situ). Generally, the benefit of laboratory measurements is the higher spatial resolution, while in-situ measurements rely on installed sensors which measure at a limited number of fixed positions. On the other hand, laboratory measurements can rarely be used on actual flying objects.

LABORATORY MEASUREMENTS

One way to identify the boundary layer state is to use Infrared (IR) thermography [44–46]. Since a turbulent boundary layer provides better heat transfer between the airfoil skin and the airflow, the part of the airfoil in the turbulent flow experiences cooling or heating of the air more intensely. Therefore, IR thermography can be used to identify where the flow is turbulent. However, a drawback is that this only works if active heating is applied to either the flow or the airfoil to induce a temperature difference between the two. Another drawback is the long minimally required measurement time in the

order of seconds to minutes, since heating and cooling takes time. The benefit however, is the relative simplistic experimental setup, which entails an external IR camera and a method to heat the flow or airfoil, such as heating lamps.

Particle Image Velocimetry (PIV) is another more complex method to observe the boundary layer [47, 48]. This method requires small particles to be present in the flow which are illuminated using a laser while their motion is captured by a high speed camera. The drawback of this method is the extensive experimental setup and time consuming data processing, while the main advantage is that an actual cross section of the boundary layer can be obtained. This makes it for instance possible to measure the boundary layer thickness.

IN-SITU MEASUREMENTS

A way to identify the boundary layer state in-situ is by measuring high frequency vibrations of the flow. This can be achieved by using pressure or sound transducers [49, 50]. These transducers can be installed at various locations in the airfoil, each probing the boundary layer locally. These high frequency vibrations can show the difference between a laminar and turbulent boundary layer. In addition, these vibrations typically are known to reach peak values near transition. A drawback of using this method is the complication when multiple aerodynamic phenomena, such as transition and separation, spatially coincide.

Another method to identify boundary layer states is by using hot film sensors, which works similar to IR thermography [51–53]. Just like pressure or sound transducers these can be installed on the airfoil, but monitor temperature changes instead of air pressure changes. Just like IR thermography, the disadvantages of this method are the requirement to heat the flow or the airfoil, and the long minimally required measurement time.

Finally we like to mention shear stress measurements [54–56]. The wall shear stress of a turbulent flow is higher compared to a laminar flow. Meanwhile, at separation the shear stress is zero, while it is in the opposite direction in a separated flow. Hence it is potentially easy to detect various boundary layer states using shear stress sensors. The main challenge of this method is the low magnitude of the shear stresses involved, requiring accurate and sensitive sensors.

1.3. THESIS OUTLINE

The main research goal of this thesis is to arrive at a functional piezoelectric based sensor system capable of measuring flow phenomena (such as transition and separation) in the boundary layer of the SmartX morphing wing. In order to translate this goal into more concrete steps, three sub-goals are formulated:

- Investigate the potential to increase the sensitivity of piezoelectric sensor materials and prevent the reliance on lead-based systems (*chapter 2* and *chapter 3*).
- Develop a sensor capable of measuring flow phenomena which can be installed within a wing (*chapter 4* and *chapter 5*).
- Realize a network of sensors (because a single sensor only provides information at its own location) to be installed in the SmartX wing and demonstrate their potential of analyzing the boundary layer under complex morphing patterns. (*chapter 6* and *chapter 7*).

Chapter 2 describes different polymer matrices and ceramic fillers that are used to manufacture piezoelectric composites [57]. Six different composite systems, comprised of two polymer matrices and three ceramic fillers, are experimentally and numerically tested. The main message of this chapter is demonstrating the importance of the matrix electrical conductivity for the use in piezoelectric composites. This is normally not included in analytical models that are used to predict the piezoelectric charge constant of composites.

Chapter 3 specifically focuses on the replacement of monolithic PZT ceramic with polymer-ceramic piezoelectric composites for sensor and energy harvesting applications [38]. The figure of merit for sensors, g_{33} , and energy harvesting, $d_{33}g_{33}$, is maximized by applying dielectrophoresis to small fiber-shaped ceramic filler fragments embedded in a polymer matrix. This process aligns the fibers, improving the properties in the direction of alignment. This, combined with the proper choice of matrix and filler materials as were investigated in chapter 2, results in an energy harvesting figure of merit comparable to that of state-of-the-art PZT. Comparing PZT to these composites, we show that by applying a sinusoidal force to the piezoelectric materials a similar amount of energy is stored in the materials per unit volume. This work shows that under the right conditions piezoelectric composites are capable of replacing piezoelectric ceramics.

Chapter 4 describes a first approach to measure dynamic pressures in a boundary layer of an airfoil using piezoelectric sensors with the aim of finding laminar-to-turbulent transition. A thin patch containing eight PZT ceramic piezoelectric elements is developed to measure oscillations perpendicular to the airfoil surface. Using the patch we are able to locate transition. However, as it turns out, the recorded signal is due to the pyroelectric effect rather than the piezoelectric effect. Details regarding the pyroelectric measurements are added to the appendix of this chapter. In addition, a patch containing eight composite piezoelectric elements is also developed and tested. Although based on

Chapter 2 and Chapter 3 piezoelectric composites were expected to perform as good sensors due to their high g_{33} , they were found not to function properly in these wind tunnel experiments. This is caused by the low dielectric constant of the composite material causing large losses in the electronic circuit behind it.

Chapter 5 follows up on the objective of chapter 4. This time, however, a piezoelectric (PZT) bimorph is located under the skin of the airfoil [58]. Such a bimorph is able to cancel the pyroelectric effect, can be installed more mechanically independent from the wingskin, and can act as mechanical amplifier. A vane piercing the skin mechanically couples the piezoelectric bimorph to the boundary layer, making the piezoelectric bimorph able to sense the vibrations occurring in the boundary layer. Using Particle Image Velocimetry (PIV) measurements as validation technique, we show that we are able to locate transition and separation on a NACA 0012 airfoil in a low Reynolds number regime. In the appendix of this chapter the PZT bimorph used in this work is compared to a manufactured composite bimorph. The composite bimorph has a similar frequency response to the PZT bimorph, and reaches about 75 % of the output voltage of the PZT bimorph. This composite bimorph is therefore potentially able to replace the lead-based bimorph.

Chapter 6 contains an overview of the SmartX wing developed [5]. It motivates the design decisions made and the technologies integrated into the wing. This includes the multi-segmental morphing principle as main actuators, the small fast actuators consisting of piezoelectric bimorphs, fiber optic sensing for wing shape measurements, the piezoelectric flow sensors described in this thesis, and the software and hardware integration into a single wing demonstrator.

Chapter 7 presents the implementation of the piezoelectric flow sensors as developed and validated in chapter 5 into the SmartX morphing wing described in chapter 6 [59]. In total 16 sensors are embedded in the morphing wing, providing information about the boundary layer in both the chordwise and spanwise direction. The effect of the location of transition is measured while morphing the airfoil over various synchronous morphing angles (i.e. morphing all segments equally), and varying the angles of attack. By using the measured amplitudes of each sensor as state variables, it is possible to increase the spatial resolution beyond the number of installed sensors and also assess what happens to the boundary layer while morphing segments individually. This method of treating the data provides an in-situ method of measuring transition on complex morphing wings.

Chapter 8 provides a concluding chapter, reflecting on the degree of realization of the three sub-goals stated in this section. In addition, recommendations are given for further development of the sensors described in this work.



2

THE EFFECT OF THE INTRINSIC ELECTRIC MATRIX CONDUCTIVITY ON THE PIEZOELECTRIC CHARGE CONSTANT OF PIEZOELECTRIC COMPOSITES

Polymer-piezoceramic composites have drawn a lot of attention for sensor and energy harvesting applications. Poling such materials can be difficult due to the electric field getting mostly distributed over the low dielectric constant matrix. During this process, the electrical matrix conductivity plays a vital role. This work shows how two different polymer materials, loaded with various piezoelectric ceramic fillers, have very different poling efficiencies simply due to their intrinsic matrix conductivity. It is shown how temperature increases the matrix conductivity, and hence, increases the piezoelectric charge constant of the composites. By choosing the proper matrix material under the proper conditions, piezoelectric composites can be poled at electric fields as low as 2 kV mm^{-1} , which is identical to that of bulk ceramic fillers. In addition, the matrix conductivity can be altered by aging the composites in a high humidity atmosphere, which can increase the piezoelectric charge constant in a similar fashion. This is a simple method to increase the matrix conductivity, and hence the piezoelectric charge constant, without the need to add any conductive fillers into the composites, which increases complexity, and leads to an increased dielectric loss.

This chapter, with exception of the appendix, has been published in Materials Research Express 7, 015703 (2019) [57]. The composite fabrication was carried out by Y. Akpinar as part of his bachelor internship.

2.1. INTRODUCTION

Piezoelectric materials have the ability to convert mechanical energy into electrical energy, and vice versa. Because of this, these materials can act as actuators, sensors and energy harvesters [9, 60–62]. It is therefore no surprise that these materials have drawn a lot of attention from researches in the field of smart sensors and renewable energy. Popular piezoelectric materials, due to their excellent values for the piezoelectric constants, are inorganic ceramics, such as the widely used lead zirconate titanate (PZT). However, these ceramics contain the substance Pb, and are therefore classified as a Substance of Very High Concern (SVHC) according to the European Community REACH regulation 1907/2006/EEC. Therefore, research is performed to find lead-free alternatives [20, 23]. Another drawback of these ceramic materials is their brittleness, which makes them susceptible to mechanical failure under large cyclic strains. This promotes the research into piezoelectric polymers, such as polyvinylidene-fluoride (PVDF) and its copolymers [26]. However, these have other disadvantages such as a limited curie temperature, T_c , high coercive field, and limited piezoelectric constants.

Piezoelectric composites combine a polymeric matrix with a piezoelectric ceramic filler [30–32]. The polymer matrix yields the mechanical flexibility, while the piezoelectric ceramic filler provides the piezoelectric effect. Since only a portion of the total volume fraction is the piezoelectric active filler, the piezoelectric charge constant, d_{33} , is generally lower compared to that of ceramics. Since d_{33} is accepted to be the figure of merit for actuator applications, composite actuators have a difficult time competing with ceramics. For sensor applications, on the other hand, the figure of merit is $d_{33}/\epsilon_r\epsilon_0$, where ϵ_0 is the permittivity of vacuum and ϵ_r is the dielectric constant. Here, composites have shown to have the upper hand due to their low value of ϵ [36, 37, 63]. For energy harvesting, with the figure of merit being $d_{33}^2/\epsilon_r\epsilon_0$, recent studies have shown that composites and ceramics can perform equally well [38, 64]. The composite systems referred to here are both highly flexible and lead-free. Their high piezoelectric constants are obtained due to the connectivity of the ceramic particles in the direction of applied stress.

An important parameter influencing the composite properties, is the choice of matrix and filler materials. To discuss the effect of various matrix and filler materials, random particulate composites are considered. These composites consist of isolated piezoelectric active particles embedded in a continuous polymer matrix. They are therefore also referred to as 0-3 composites, since the filler is continuous in zero dimensions while the matrix is in all three [33]. These have been investigated for a while already, and countless models have been proposed for modelling their piezoelectric constants [65]. Although the models can vary from one to another quite a lot, the general trends are agreed upon:

- i. By increasing the volume fraction of the filler, φ , both ϵ_r and d_{33} of the composite increases.
- ii. Increasing the bulk dielectric constant of the filler, ϵ_f , generally does not increase the ϵ_r of the composite. Note that this only applies to the case where ϵ_f is far greater than the dielectric constant of the matrix, ϵ_m , which in this field is nearly

always true. Therefore, ϵ_r of the composite is dominated by ϵ_m .

- iii. The d_{33} of the composite depends on the mismatch between ϵ_m and ϵ_f . The smaller the mismatch, although it is generally rather large, the higher the d_{33} of the composite.

These three statements are true assuming that the piezoelectric composites are fully poled. However, poling these kind of composites can be tricky, since most of the applied electric field gets lost in the polymer matrix. Therefore, another important parameter to consider is the matrix conductivity, σ_m .

Earlier work has already shown that the matrix conductivity plays an important role [32]. Increasing the matrix conductivity does not increase the maximum achievable d_{33} , but does decrease the electric field required to fully pole the piezoelectric composites. Various studies have shown that by adding a third conductive phase into the polymer matrix this required electric field indeed decreases [32, 66, 67]. However, by introducing a conductive phase into the composites, the dielectric loss, $\tan(\delta)$, typically increases. Therefore, ideally, one would gain the benefit of the increased matrix conductivity only during poling, while during operation the matrix conductivity is low again, maintaining a low dielectric loss. This can be achieved by considering the conductivity of polymers at elevated temperatures. Generally, the conductivity of polymers increases with increasing temperature, although the exact magnitude strongly depends on the chosen polymer system.

In this work, two different polymers are chosen to act as matrix materials in piezoelectric composites, being an epoxy and a polyurethane (PU) polymer. The two polymers have a nearly identical value of ϵ_m , meaning that, when making piezoelectric composites out of them, their maximum value of d_{33} is nearly identical as well. Both have increased conductivity at elevated temperatures, although to a different extent. It is shown that the higher conductivity polymer reaches its maximum d_{33} already at low electric fields, while the other one does not reach it at all. To make sure that this phenomenon is matrix material independent, three different filler materials are embedded in the polymers, yielding six different composite systems. The filler materials used are BaTiO₃ (BT), K_{0.485}Na_{0.485}Li_{0.03}NbO₃ (KLN) and PZT-5A4 (PZT). The obtained d_{33} values are compared to Jayasundere's model [68, 69]. This model is chosen because it includes both the dielectric constant and the piezoelectric charge constant, does not have any supposed fitting parameters, and includes interactions between neighboring particles. The following equations are given in Jayasundere's work to calculate ϵ_r and d_{33} :

$$\epsilon_r = \frac{\epsilon_m(1 - \varphi) + \epsilon_f \gamma}{(1 - \varphi) + \gamma} \quad (2.1)$$

$$\gamma = \frac{3\epsilon_m \varphi}{2\epsilon_m + \epsilon_f} \left(1 + 3\varphi \frac{\epsilon_f - \epsilon_m}{2\epsilon_m + \epsilon_f}\right) \quad (2.2)$$

$$d_{33} = \left(1 + \frac{3\varphi \epsilon_f}{2\epsilon_m + \epsilon_f}\right) \frac{\epsilon_r}{\epsilon_f} d_{33f} \quad (2.3)$$

In here, φ is the filler volume fraction and d_{33f} is the d_{33} of the filler material.

In addition to the two matrix materials investigated in this work, a third matrix material, polydimethylsiloxane (PDMS), was also investigated. Since we were not able to fully explain the obtained properties using this matrix material, we did not add it to the main body of this chapter. The data is however worth showing due to the high piezoelectric constants obtained, and is therefore briefly discussed in Appendix 2.A.

2.2. FABRICATION OF 0-3 PARTICULATE COMPOSITES

The starting powders are fine BaTiO₃ (BT) (obtained from Sigma Aldrich), pre-calcined K_{0.485}Na_{0.485}Li_{0.03}NbO₃ (KNLN) (obtained from CeramTec, Ruabon, UK) and green PZT-5A4 (PZT) (obtained from CeramTec, Ruabon, UK). All the powders are calcined to obtain single phase materials. The BT is calcined at 900 °C for 2 h (heating rate of 2 °Cmin⁻¹), the KNLN at 925 °C for 10 h (heating rate of 1 °Cmin⁻¹) and the PZT at 1150 °C for 1 h (heating rate of 2 °Cmin⁻¹)[36, 70]. After calcination, the powders are milled in a planetary ball mill (Retsch PM100, Aartselaar, Belgium) for 1 h at 150 rpm using 10 mm yttria-stabilized ZrO₂ balls immersed in cyclohexane. Finally, the powder is dried in a furnace. From scanning electron microscope (SEM) (JEOL, JSM-7500F, Nieuw Venneep, the Netherlands) micrographs, shown in Fig. 2.1, an estimate of the particle size is made. The BT particles are slightly smaller, while the PZT are slightly bigger, and KNLN has a couple of big particles. All filler particles are in the range of 0.5 – 5 μm. Typical properties of the powders involved are shown in Table 2.1.

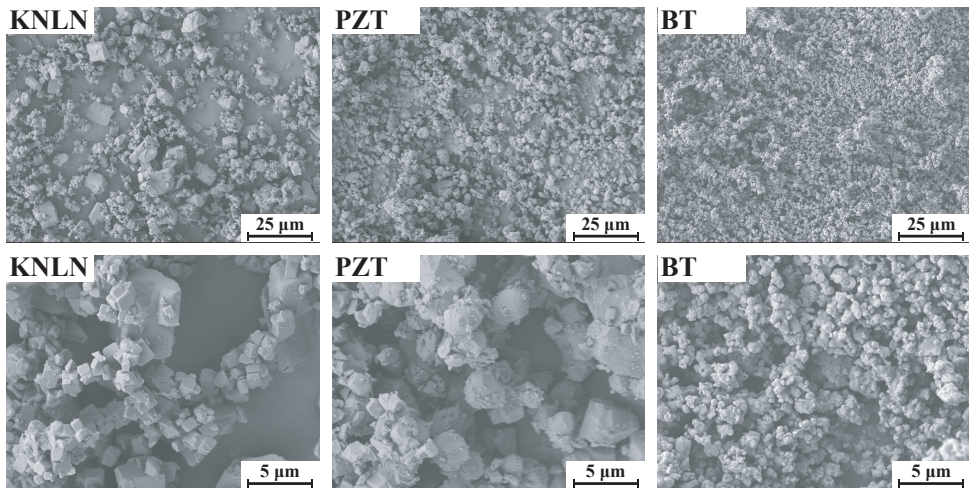


Figure 2.1: SEM micrographs of calcined KNLN particles, PZT particles and BT particles, at a 1000x (left) and 5000x (right) magnification.

All three types of filler particles are mixed into epoxy (Epotek epoxy 302-3M, Epoxy Technology Inc.) and PU (Crystal Clear 202, Smooth-on Inc.), yielding six different types of composite systems. The nearly identical value of ϵ_m of the two polymer matrices are given in Table 2.1 as well. The nearly identical value is chosen on purpose, to make sure

Table 2.1: Filler and matrix material properties.

Material	Function	ϵ_r [-]	d_{33} [pC N ⁻¹]	Reference
KNLN	Filler	360	125	[25, 71]
PZT	Filler	1850	460	[72]
BT	Filler	1800	190	[9]
Epoxy	Matrix	3.4	-	[73]
PU	Matrix	3.3	-	[74]

that their theoretical maximum value of d_{33} , after making composites out of them, is nearly identical as well. The filler particles are added to the polymer matrix in various volume fractions (30, 40, 50 and 60 vol%) and mixed using a planetary speed mixer (DAC 150 FVZ, Hauschild, Germany). In order to fabricate disk shaped composite pellets, the obtained mixture is poured into prefabricated holes punched into a Teflon sheet. Note that the higher volume fraction mixtures do not flow, and therefore could not be poured. These are forced in the holes using a spatula instead. The Teflon sheet is covered on both sides with two other Teflon sheets, without any punched holes, and clamped between two steel plates. While being clamped, the composite slurries are cured at 120 °C for 2 h. This temperature is slightly higher compared to the manufacturer's recommended curing temperature to prevent any ageing or further curing effects during the poling process. Nine composites are manufactured per materials set. However, due to the high volume fraction composites being more difficult to successfully produce, some break during processing. Due to this, at least five out of the nine samples produced were successfully measured.

After curing, gold electrodes are sputtered through a shadow mask on both sides of the composites with a sputter coater (Quorum Q300T, East Sussex, UK). The final step is poling, which provides the composites with their piezoelectric charge constant. Poling is performed in a silicon oil bath, providing control over poling field, time and temperature. The applied electric field is chosen to be as high as possible while having the lowest possible chance of getting short circuits, ruining the samples. The DC electric field is therefore set to 8.5, 8.0, 7.5 and 7.0 kV mm⁻¹ for the 30, 40, 50 and 60 vol% composites, respectively. As for the poling time, it has been shown before that only relatively short periods are required to successfully pole composites [38, 75]. Therefore, all composites are poled for only 5 min. The maximum temperature to pole at is the minimum of the following three temperatures: the T_c of the ceramic filler, the temperature at which the polymer matrix starts to be too conductive, and the temperature at which the polymer matrix starts to degrade. Both the epoxy and PU matrix are able to withstand temperatures of over 150 °C. However, at temperature above 120 °C epoxy starts to become too conductive. This means that at temperatures above 120 °C a relatively high current starts to flow through the sample, which will significantly reduce the poling efficiency, and potentially destroys the samples. Therefore, the poling temperature is set to this maximum of 120 °C. In addition, the BT filler particles have a T_c of 120 °C. Poling near

the T_c requires the electric field to stay applied until the temperature has dropped to at least half the T_c to prevent depolarization from occurring. Therefore, for all BT composites, after the 5 min of poling time at 120 °C, the temperature is lowered to below 50 °C before the electric field is switched off.

2

The composites are aged for at least 24 h at room temperature after poling before measuring the piezoelectric constants. The piezoelectric charge constant, d_{33} , is measured with a Berlincourt-type piezometer on poled capacitors (PM300, Piezotest, London, UK). Rounded anvils are used with a radius of 16 mm. A static force of 10 N is applied, under a 0.25 N peak-to-peak sinusoidal excitation at 110 Hz. We note that the extracted value of d_{33} depends on the boundary conditions, such as the sample aspect ratio [76]. Here all measurements have been performed under identical conditions using 1 mm thick piezoelectric disks with a radius of 12 mm. Therefore the extracted values of d_{33} can be directly compared, resulting in a reliable material comparison. The capacitance and dielectric loss are measured at 1 kHz and 1 V with a LCR meter (Agilent 4263B, Santa Clara, CA, USA). The dielectric constant, ϵ_r , measured under zero stress, was derived from the capacitance. The density of the composites is measured using an Archimedes setup, using distilled water as the liquid medium. The conductivity of the composites and polymer matrix materials is measured using a Broadband Dielectric Spectrometer (BDS) (Novocontrol Alpha Analyzer, Montabaur, Germany). Finally, the polarization is also measured using hysteresis measurements (Radiant Precision RT66c, Albuquerque, USA).

2.3. RESULTS & DISCUSSION

This section discusses the dielectric constant (2.3.1), the piezoelectric charge constant (2.3.2), hysteresis loop measurements (2.3.3) and the effect of humidity on poling efficiency (2.3.4).

2.3.1. DIELECTRIC CONSTANT

The dielectric constant of the composites, ϵ_r , is measured as a function of volume fraction, matrix material and filler material. The results are shown in Fig. 2.2. The epoxy composites are given in blue (Fig. 2.2a), while the PU composites are given in red (Fig. 2.2b). Meanwhile, the three different fillers are given in different shades of blue and red, with different symbols. Jayasundere's model is included with the dashed lines. Note that only two dashed lines are visible since two of them, the PZT and BT line, closely overlap each other. This happens due to their similar value of ϵ_f .

From the figure it can be seen that, in general, the experimental values get near the theoretical prediction. This is especially true for PZT (square data points), which almost perfectly fits the curve. This can be attributed to the homogenous particle size, as shown in Fig. 2.1. In the case of KNLN, the experimental data is slightly higher compared to the predicted curve. Again consulting Fig. 2.1, this can be explained due to the few larger particles, slightly increasing the dielectric constant. Finally, in the case of BT, the experimental values are clearly higher than predicted, by about a factor of two. Again,

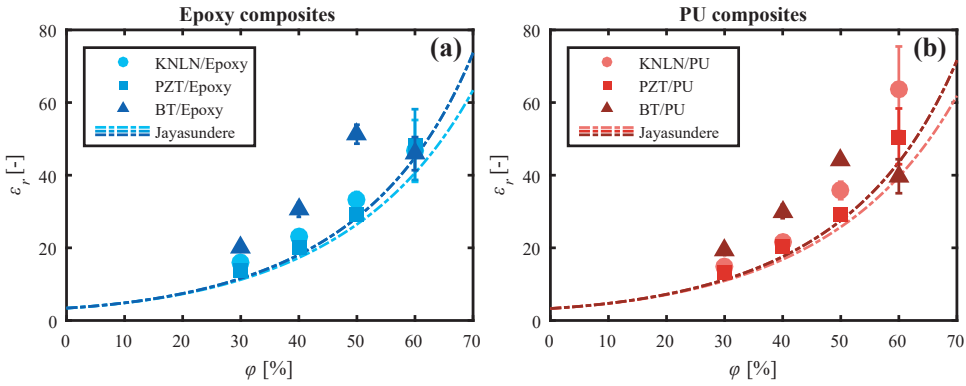


Figure 2.2: Composite dielectric constant, ϵ_r , versus filler volume fraction, ϕ , of (a) epoxy composites and (b) PU composites. The dashed lines are obtained from Jayasundere’s model [68, 69]. Note that only two dashed lines are visible since two of them, the PZT and BT line, closely overlap each other. This happens due to their similar value of ϵ_f . In all cases the dielectric loss, $\tan(\delta)$, was measured to be below 3%, measured at a frequency of 1 kHz.

this can be explained by considering their particle size. Fig. 2.1 shows slightly smaller particles for BT. Smaller particles are more susceptible to static attractions, which in turn agglomerates the particles in the polymer matrix. These agglomerations can increase the dielectric constant, likely due to the lower amount of filler-matrix interfaces. It can also be seen from the experimental data that at a volume fraction of 60 % the dielectric constant of the BT composites suddenly decreases. Due to the agglomerations, it is harder to achieve fully dense composites at higher volume fractions. This is confirmed from the composite densities measured using Archimedes principle, shown in Fig. 2.3. In all cases the density is lower at a volume fraction of 60 %, although the extent of this is clearly more profound for the BT composites. This decreased density has a serious impact on the dielectric constant.

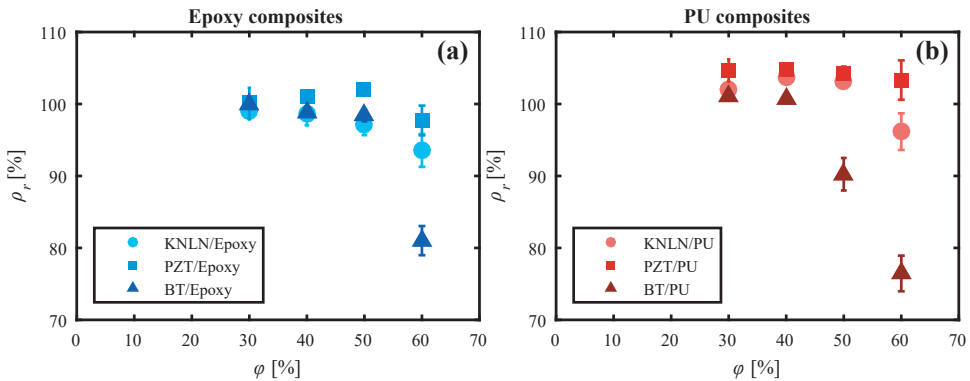


Figure 2.3: Composite relative density, ρ_r , versus filler volume fraction, ϕ , of (a) epoxy composites and (b) PU composites.

From Fig. 2.2, it can be confirmed that ϵ_r is independent of ϵ_f , which is agreed upon by various analytical dielectric models [65]. It is therefore concluded that, for the composites with good homogeneity, the experimental data fits Jayasundere's model almost perfectly.

2.3.2. PIEZOELECTRIC CHARGE CONSTANT

The piezoelectric charge constants of the composites, d_{33} , is measured as a function of volume fraction, matrix material and filler material. The results are shown in Fig. 2.4. The epoxy composites are given in blue (Fig. 2.4a), while the PU composites are given in red (Fig. 2.4b). Meanwhile, the three different fillers are given in different shades of blue and red, with different symbols. Jayasundere's model is included with the dashed lines.

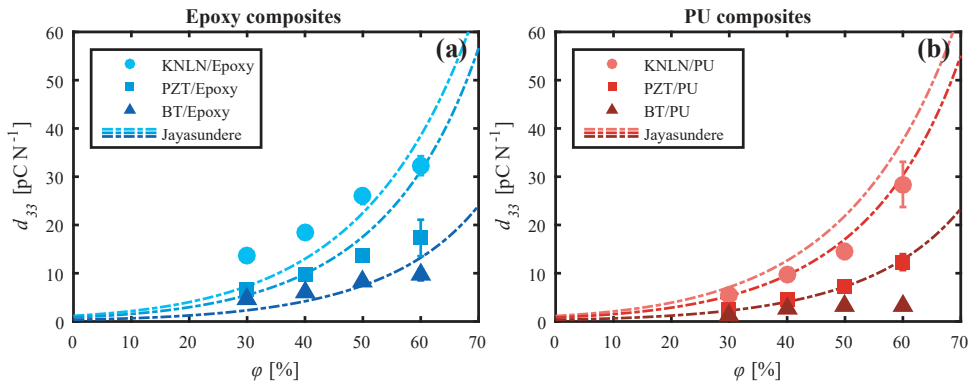


Figure 2.4: Composite piezoelectric charge constant, d_{33} , versus filler volume fraction, ϕ , of (a) epoxy composites and (b) PU composites. The dashed lines are obtained from Jayasundere's model [68, 69].

The first thing to notice from Fig. 2.4 is that the predicted trends are correct; KNLN composites indeed have the highest d_{33} values, followed by the PZT composites, while the BT composites have the lowest d_{33} . This is agreed upon by Jayasundere's model, and can simply be explained by the better d_{33f}/ϵ_f values of the ceramic filler materials, which are 0.35, 0.25 and 0.11 for KNLN, PZT and BT, respectively. Taking a closer look at Fig. 2.4a, it can be seen that the experimental data of the epoxy composites generally lies quite close to Jayasundere's prediction. This is especially true for a volume fraction of 40 – 50 %. At lower volume fractions Jayasundere slightly underestimates, while at higher volume fractions it overestimates. The overestimation at higher volume fractions can be caused due to the decreasing density trend with increasing volume fraction, as was shown earlier on in Fig. 2.3. Taking a look at the PU composites, shown in Fig. 2.4b, a completely different behavior is observed. Since ϵ_m of epoxy and PU is almost identical, the d_{33} of the composites should be identical as well. Still, in all cases, the experimental d_{33} values of the PU composites are lower than that predicted by Jayasundere's model. Still the same trends are observed as is seen with epoxy composites, just with lower d_{33} values.

To understand why PU composites have a lower d_{33} , a more detailed poling study is performed, measuring the d_{33} of composites with a volume fraction of 40 % versus the DC electric poling field. All composites are poled at 120 °C for 5 min. Only the BT composites, due to the low T_c of the ceramic filler, are cooled down to below 50 °C before the electric field is removed. The electric field is varied from 1 to 8 kV mm⁻¹. The results are shown in Fig. 2.5. In all cases, at 1 kV mm⁻¹ d_{33} is found to be zero, which makes sense since this is not enough to pole the ceramic fillers themselves. All epoxy composites, shown in Fig. 2.5a, show a plateau at higher voltages, meaning the maximum possible d_{33} is achieved for these composites. In the case of PU however, shown in Fig. 2.5b, none of the composites seem to reach their maximum value. This seems to indicate, that by simply increasing the electric field more, their maximum would be reached. This theoretical maximum of the PU composites, should, according to Jayasundere's model, have similar values to the epoxy composites. However, in this case it proved to be difficult to reach higher fields, since above 8 kV mm⁻¹ the composites suffered from dielectric breakdown. Therefore, it is not possible to increase the electric field further.

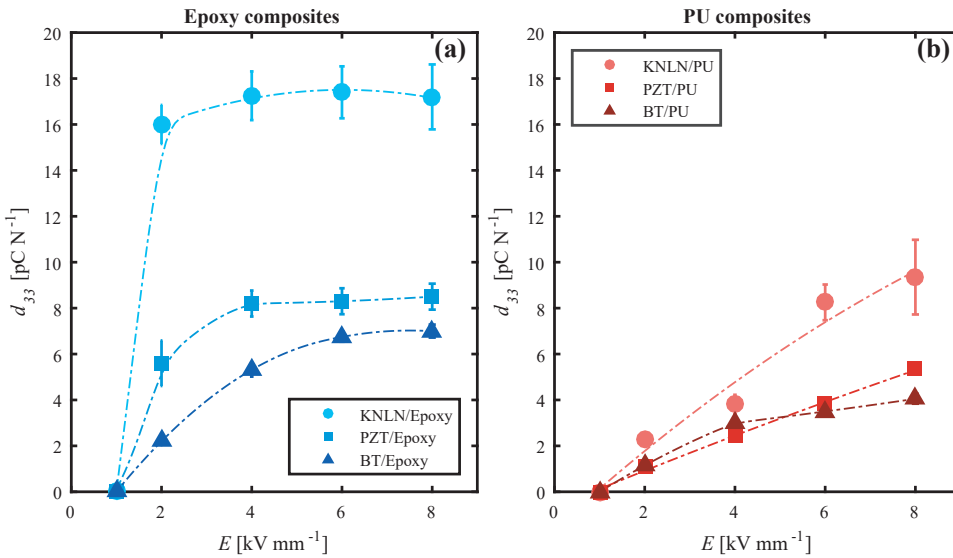


Figure 2.5: Composite piezoelectric charge constant, d_{33} , versus DC electric poling field, E , of (a) epoxy composites and (b) PU composites, both with a volume fraction of 40 %. The dashed lines are obtained using polynomial fitting.

It has been shown before that in order to reduce the required voltage to fully pole piezoelectric composites, one could increase the conductivity of the matrix material [32]. Therefore, the conductivity of the matrix materials is measured using BDS. The results are shown in Fig. 2.6. Since poling is performed with a DC electric field, the bulk DC conductivity needs to be determined. Normally, the AC conductivity decreases as frequency decreases, and finally reaches a plateau at low frequencies. This plateau can be considered as the DC conductivity [77]. At room temperature, such a plateau seems

to be absent, and the AC conductivities of both the epoxy and PU matrices look nearly identical. At the poling temperature, however, both matrix materials do show the DC conductivity plateau. Here it can be seen that epoxy reaches a DC conductivity which is two orders of magnitude larger than PU. This explains why the epoxy composites pole at much lower voltages compared to the PU composites.

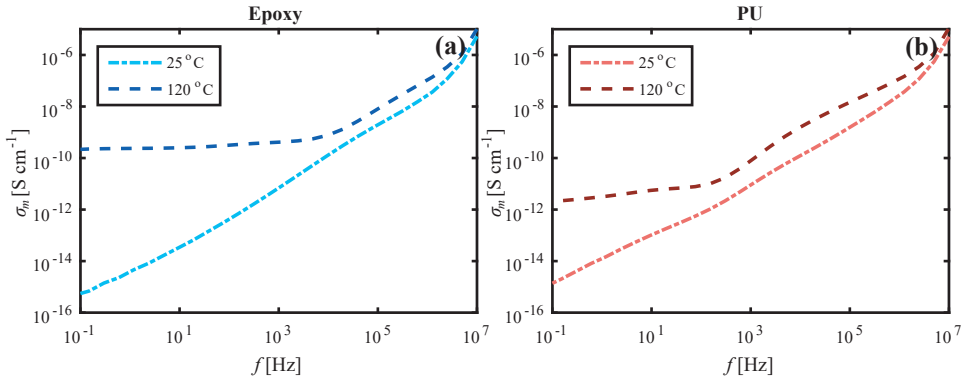


Figure 2.6: Polymer matrix conductivity, σ_m , as a function of frequency, f , for the (a) epoxy matrix and (b) PU matrix. Measurements are both performed at room temperature and the poling temperature of 120 °C.

2.3.3. HYSTERESIS LOOP MEASUREMENTS

To validate the d_{33} values obtained through the conventional DC contact poling, polarization hysteresis measurements have been performed on the composites. The results are shown in Fig. 2.7, where again all the epoxy composites are given in blue, while all PU composites are given in red. All the measurements are performed at the same temperature as the conventional DC contact poling of 120 °C. The same trends are obtained, giving higher polarizations for epoxy composites over PU composites, and higher polarizations for KNLN over PZT and BT. The main difference between conventional DC contact poling and the hysteresis measurements is time. Where the conventional method lasted for 5 min, the total hysteresis time is in the order of seconds, or even less, depending on the frequency. Generally, longer times give higher polarization values. However, from this figure it is hard to judge whether the polarization actually increases, since the loops show a high leakage current at low frequencies.

To understand the nature of the leakiness, hysteresis measurements of a PZT-5A4 ceramic disk are considered, shown in Fig. 2.8. Here it can be seen, that by decreasing the frequency from 30 to 3 Hz, a big increase in polarization is observed. Decreasing it further to about 1 Hz, does not increase the polarization any further. This means that there is a minimum amount of time required for the dipoles to align. When this time is reached, all dipoles have aligned, and maximum polarization has been reached. Here, however, the loop does not become leaky, as was seen with the composites. This can be explained by considering the equivalent circuit diagram of a piezoelectric material

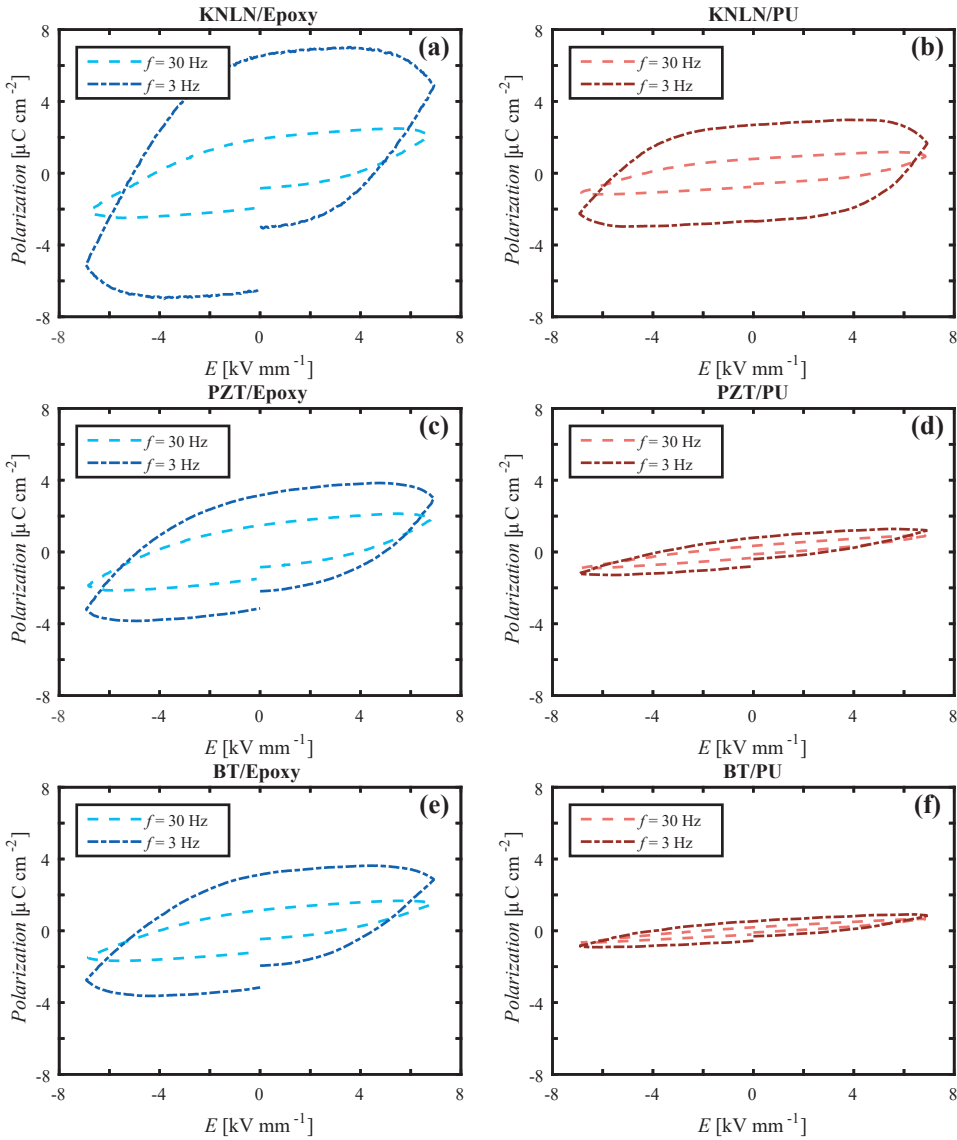


Figure 2.7: Hysteresis loops of (a) KNLN/epoxy, (b) KNLN/PU, (c) PZT/epoxy, (d) PZT/PU, (e) BT/epoxy and (f) BT/PU composites, all containing 50 vol% ceramic filler, varying the applied AC electric field frequency. All measurements are performed at the poling temperature of 120 °C. In all cases the electric field starts at zero, then first goes to the maximum, then down to the minimum, and finally back to zero.

which is exposed to an AC electric field, as shown in Fig. 2.9a. When the frequency decreases, the impedance, Z , increases. Meanwhile, the resistance, R , which is frequency independent, stays the same. Since the applied voltage chooses the path of least resistance, the electric field starts to run more through the resistor R as the frequency continues to decrease. This means that the piezoelectric material starts to exhibit more resistive losses. A typical resistor loop is shown in Fig. 2.9b, showing a very leaky loop. If the electric field runs mostly through the capacitor Z , a ferroelectric loop will be measured, with its typical shape also shown in Fig. 2.9b. Now PZT-5A4, as shown in Fig. 2.8, does not show a leaky loop at low frequencies due to its higher capacitance. Generally, the capacitance of ceramics is about one or two orders of magnitude higher compared to composites, meaning that Z will be one or two orders of magnitude lower. Therefore, the frequency at which composites start to show leaky loops is also orders of magnitude higher compared to ceramics.

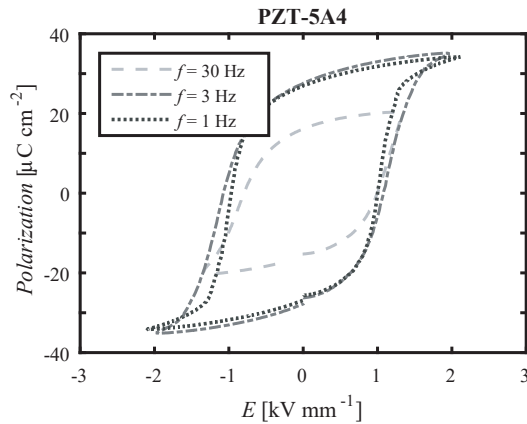


Figure 2.8: Hysteresis loop of PZT-5A4 ceramics, varying the applied AC electric field frequency.

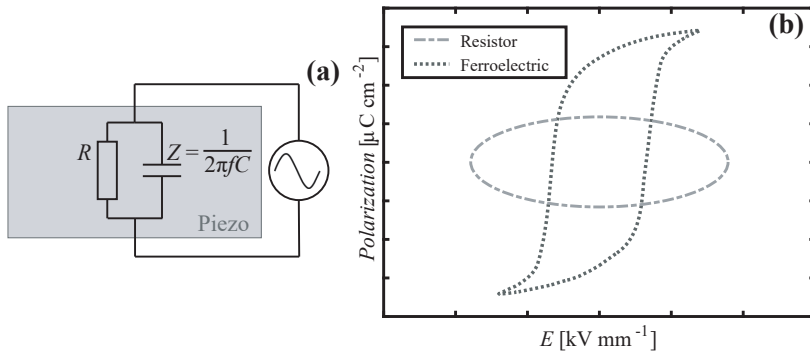


Figure 2.9: (a) Equivalent circuit diagram of a piezoelectric material exposed to an AC electric field is applied. (b) Typical hysteresis loops of a resistor and a ferroelectric [78].

Due to this issue, it becomes clear that it is challenging to accurately measure the polarization of composites such as the ones shown in this work. On the one hand one needs longer times, or lower frequencies, in order to reach the threshold at which all the dipoles had enough time to polarize. On the other hand, one needs high frequencies, or shorter times, to prevent the applied electric field from leaking away in the resistive part of the material.

An estimation of the corresponding d_{33} to the hysteresis loops can be made using Fig. 2.8. The remnant polarization of the PZT is about 30 pCcm^{-2} , which results in a d_{33} of about 400 pCm^{-1} . Applying this to the PZT/epoxy and PZT/PU composites from Fig. 2.7c and d, the remnant polarizations of about 1.5 and 0.5 pCcm^{-2} , obtained from the 30 Hz non-leaky loop, scale to a d_{33} of about 20 and 7 pCm^{-1} , respectively. Comparing this to the actual d_{33} values given in Fig. 2.4, the PZT/epoxy composites have a slightly lower d_{33} while the PZT/PU composites have exactly the same as is estimated from the hysteresis measurements. This means that the 30 Hz polarization measurements appear to be quite correct.

2.3.4. THE EFFECT OF HUMIDITY

A well-known problem of the KNN based system, is its moisture sensitivity [25]. Absorbed moisture in this ceramic filler causes the dielectric loss, $\tan(\delta)$, to increase rapidly, making it problematic to use this piezoelectric ceramic in applications. A polymer matrix around the ceramic filler can solve, or mitigate, this issue. Using BDS, the dielectric loss of KNLN/epoxy and KNLN/PU composites is measured versus aging time after drying the samples in a furnace at 100°C for 2 h . The aging itself is simply performed in laboratory conditions, which generally means a humidity of about $40 - 60\%$, and a temperature of about 22°C . The results are presented in Fig. 2.10. As a comparison, the gray lines indicate bulk KNLN ceramic. It can be seen that epoxy protects the KNLN quite well, while the $\tan(\delta)$ of the KNLN/PU composite is almost identical to that of bulk KNLN after one week of aging. This indicates that the PU matrix is able to absorb moisture, while epoxy barely does so, even after one year of time.

Although the moisture absorbing capabilities of the PU matrix is a clear disadvantage when using KNLN as a filler material, when using another filler such as PZT it becomes a completely different story. PZT is not moisture sensitive, and therefore does not suffer the consequences KNLN does when in contact with a humid matrix. Actually, in the case of PZT, it turns out that the humidity sensitivity of PU can be used to our advantage. By increasing the humidity of the matrix, the matrix conductivity increases. To see the extent of this increased conductivity, the conductivity of PZT/epoxy and PZT/PU composites is measured at ambient conditions, including a measurement where the PZT/PU is aged in a high humidity (humidity of about 90%) atmosphere for a week. The results are shown in Fig. 2.11. From Fig. 2.11b it can be seen that at room temperature, the difference in conductivity between the ambient and high humidity aged PZT/PU composites is barely noticeable. At the poling temperature, however, almost one order of magnitude increased conductivity is found. Comparing to Fig. 2.11a, the conductivity is still one order of magnitude lower than that of PZT/epoxy. Still, this increased

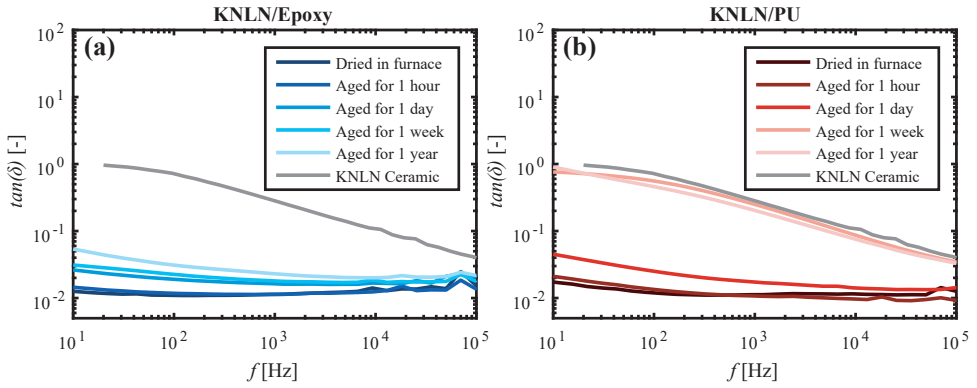


Figure 2.10: Dielectric loss, $\tan(\delta)$, versus frequency, f , of (a) KNLN/epoxy composites and (b) KNLN/PU composites.

humidity in PZT/PU, which in turn increases the conductivity, could increase the poling efficiency, and therefore, the composite its d_{33} .

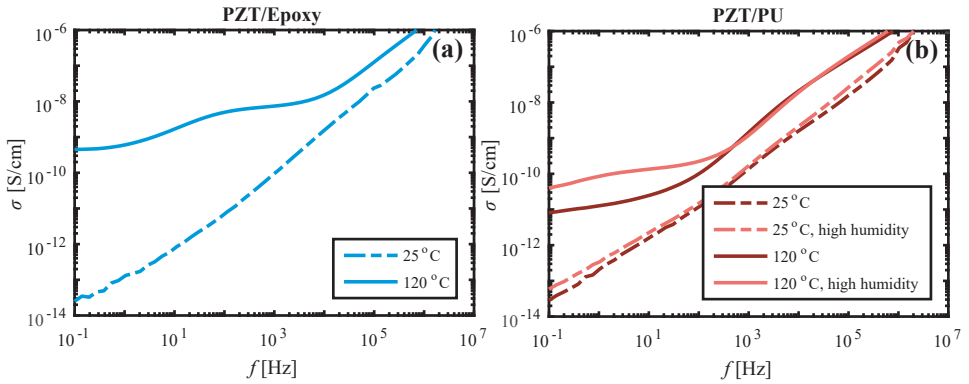


Figure 2.11: Composite conductivity, σ , as a function of frequency, f , for (a) PZT/epoxy and (b) PZT/PU composites, with a volume fraction of 50 %. Measurements are both performed at room temperature and the poling temperature of 120 °C.

After aging the PZT/PU composites for a week in different humidity environments, they are poled using the same poling parameters as before, being a DC electric field of 8 kVmm^{-1} , for 5 min time, at 120 °C. The obtained values for d_{33} are shown in Fig. 2.12. A clear trend is found where d_{33} increases with humidity in which the composites are aged. This can be attributed to the increased conductivity of the polymer matrix due to the presence of moisture. Consulting the 40 volume percent PZT composites from Fig. 2.4, the PZT/epoxy composites reach a d_{33} of 10 pCn^{-1} , which is still slightly higher compared to the 8 pCn^{-1} reached by the PZT/PU aged in high humidity conditions. This means that the PZT/PU composites are still not fully poled, which can be attributed to the slightly lower matrix conductivity of the PU composites shown in Fig. 2.11.

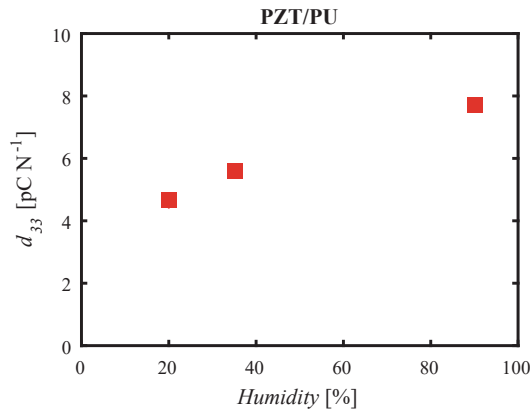


Figure 2.12: Piezoelectric charge constant, d_{33} , of 40 volume percent PZT/PU composites as a function of the humidity in which the composites are aged at for a week.

Note that this trick can only be achieved using ceramic fillers which are themselves insensitive to moisture, in combination with a polymer matrix which is able to absorb moisture. This makes it able to increase the matrix conductivity, while keeping the $\tan(\delta)$ low enough to still be able to apply an electric field without causing shorts.

2.4. CONCLUSIONS

Various polymer-piezoceramic granulate composites, consisting of piezoelectric ceramic filler particles randomly distributed in a polymer matrix, are fabricated. Typically, piezoelectric composites can be difficult to fully pole due to applied electric field getting mostly distributed over the low dielectric constant matrix. Therefore, the electrical matrix conductivity plays a vital role.

It has been shown that the matrix conductivity increases by increasing the temperature, making it essential for these composites to be poled at elevated temperatures. The conductivity of the epoxy matrix used in this work strongly reacts to the increased temperature, making it possible to fully pole these composites at low electric fields. Both conventional contact poling, lasting 5 min, and hysteresis measurements, lasting in the range of seconds, show the same trends. During hysteresis measurements leaky loops are observed when increasing the measurement time. Composites show this behavior, in contrast to most other piezoelectric materials, due to their low capacitance.

The conductivity of the PU matrix used in this work reacts in a less pronounced manner to an increased temperature, making it harder to fully pole composites with this type of matrix. The PU matrix is however able to absorb moisture. By doing this on purpose, by aging the PU composites in a high humidity environment, the composite conductivity can be increased by about one order of magnitude. This increased conductivity leads to an increased poling efficiency, which in turn increases d_{33} .



APPENDICES

2.A. POLYDIMETHYLSILOXANE (PDMS)

PDMS is a compliant matrix material with ϵ_m equal to 2.7, slightly lower compared to that of epoxy and PU which are 3.4 and 3.3, respectively. This slightly lower value of ϵ_m lowers the dielectric constant of the composites, ϵ_r , which can be beneficial for sensors as this increases g_{33} . However, according to various piezoelectric analytical models, this also decreases the composite d_{33} which has a negative effect on g_{33} [69, 79]. However, the latter does not seem to apply to PDMS, which is briefly discussed in this appendix.

For the fabrication of the PDMS composites exactly the same fabrication procedure is used as is described in section 2.2. The dielectric constant of the composites, ϵ_r , and the piezoelectric charge constant of the composites, d_{33} , as a function of volume fraction, ϕ , and filler material are given in Fig. A1a and A1b, respectively. Comparing Fig. A1a to Fig. 2.2, a similar trend is observed. The only difference is the slightly lower values of ϵ_r for PDMS, which occurs due to the slightly lower value of ϵ_m of PDMS. Again, we find that the 60 vol% data point using BT as filler has a lower value compared to the 50 vol% data point, which also here happens due to a decrease of the composite density.

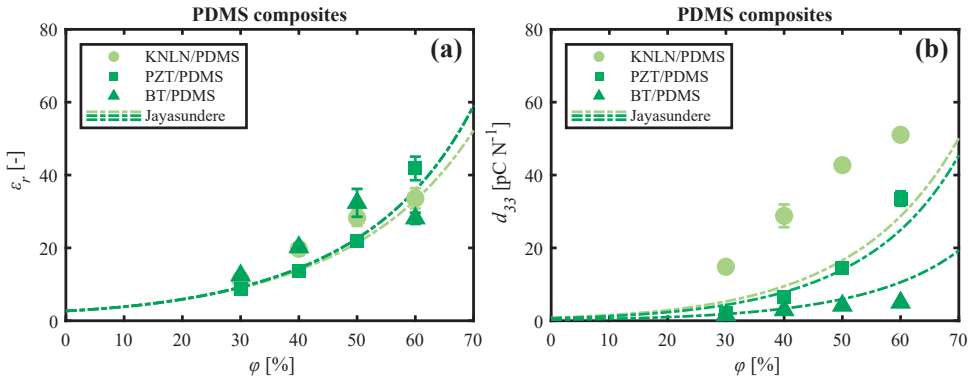


Figure A1: Composite (a) dielectric constant, ϵ_r , and (b) piezoelectric charge constant, d_{33} , versus filler volume fraction, ϕ . The dashed lines are obtained from Jaysundere's model [68, 69]. Note that in a) only two dashed lines are visible since two of them, the PZT and BT line, closely overlap each other. This happens due to their similar value of ϵ_f . In all cases the dielectric loss, $\tan(\delta)$, was measured to be below 3%, measured at a frequency of 1 kHz.

Comparing Fig. A1b to Fig. 2.4, we again find that the BT filler provides the lowest constants while KNLN provides the highest. However, using PDMS as matrix material,

the properties of the KNLN composites reach higher values as is predicted using Jaysundere's model. Since the ϵ_m of PDMS is slightly lower than that of epoxy and PU, one would expect to have lower properties using PDMS. A lower value of ϵ_m will increase the dielectric mismatch between the matrix and filler, and thereby decrease the electric field applied to the filler particles during poling, which would result in a lower value of d_{33} .

The piezoelectric charge constant, d_{33} , versus the DC electric poling field, E , of all composites is given in Fig. A2. In all cases, the epoxy composites seem to reach a plateau where no further increase of d_{33} can be reached by increasing the electric field. Also in all cases, the PU composites seem to not reach a saturated value, and can most likely reach a higher d_{33} simply by turning up the electric field even more. However, in most cases this will cause short circuiting, damaging the samples. In the case of PDMS composites using PZT or BT as filler materials generally the lowest d_{33} is found, which is what one would expect from the low ϵ_m of PDMS. However, the one major exception is KNLN/PDMS. It seems like a certain threshold has to be reached, which is in this case between 2-6 kV mm⁻¹, after which the d_{33} increases drastically with electric field, reaching a plateau at a far larger d_{33} value of about 27 pC N⁻¹.

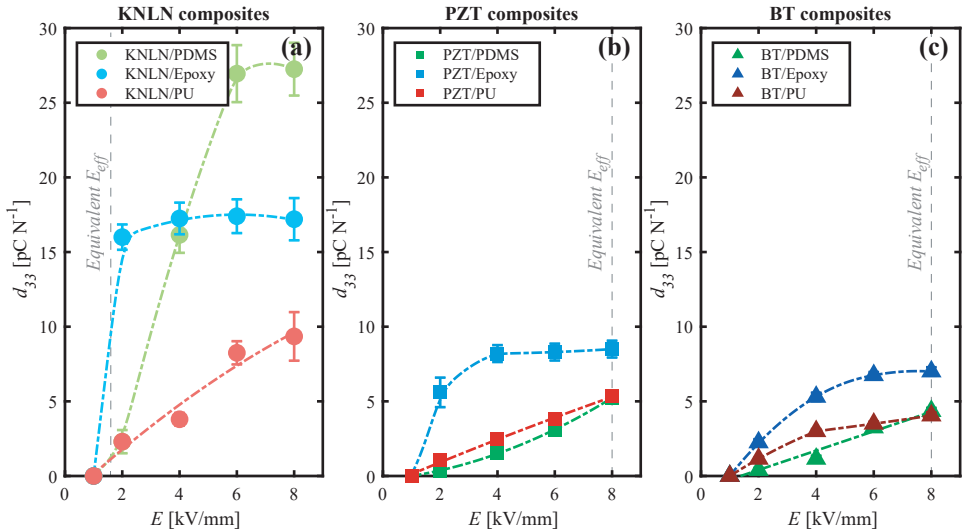


Figure A2: Composite piezoelectric charge constant, d_{33} , versus DC electric poling field, E , of (a) KNLN composites, (b) PZT composites and (c) BT composites, all with a volume fraction of 40 %. The colored dashed lines are obtained using polynomial fitting. The gray dashed lines represent the electric field at which equivalent electric field is applied to the filler particles, E_{eff} .

One way to explain the outlier of Fig. A2 considering all the PDMS composites (green data points), is by considering the effective electric field acting on the ceramic particles, E_{eff} , which is defined by the mismatch between ϵ_m and ϵ_f by the following equation [32]:

$$E_{eff} = \frac{3\epsilon_m}{\epsilon_f + 3\epsilon_m} E \quad (2.4)$$

Using this equation, we find that the E_{eff} of KNLN composites is 5 times higher compared to that of PZT or BT composites due to the significantly different value of ϵ_f . That means that if we want to compare data from KNLN composites to that of PZT or BT composites, it is unfair to consider the same applied electric field, E . Instead, we should compare the same E_{eff} . For instance, the E_{eff} at $E = 8 \text{ kVmm}^{-1}$ of PZT or BT composites is the same as the E_{eff} at only $E = 8/5 \text{ kVmm}^{-1}$ of KNLN composites. This equivalent E_{eff} is also shown in the figures using gray dashed lines. By considering the window up until the equivalent E_{eff} , in both cases the PDMS composites (green lines) follow the same trend as the PU composites (red lines). It is therefore not unthinkable that if the electric field is further increased in the case of PZT/PDMS and BT/PDMS they will actually outperform PZT/epoxy and BT/epoxy, repetitively. Since the d_{33} of KNLN/PDMS composites reach a plateau around $E = 6 \text{ kVmm}^{-1}$, the d_{33} of PZT/PDMS and BT/PDMS composites might reach a plateau at 5 times that field ($E = 30 \text{ kVmm}^{-1}$). Poling at such a field is however physically impossible using this material.

Another major difference between the various matrix materials was observed during hysteresis measurements. Hysteresis measurements of PDMS composites are shown in Fig. A3. Comparing this to the measurements shown before in Fig. 2.7, we see surprisingly low polarization values. In the case of PZT and BT composites this makes sense, since we have seen that the d_{33} of PDMS composites in those cases does not perform better compared to epoxy or PU composites. KNLN composites on the other hand definitely benefits from having a PDMS matrix, but this is not shown at all from the hysteresis measurements. The main reason for the low polarization found here is time, which PDMS requires more of compared to other matrix materials. This is shown in Fig. A4, presenting the relative piezoelectric charge constant, $d_{33,r}$, which is the percentage of d_{33} obtained after only 5 s of poling compared to the d_{33} obtained after 5 min of poling at 120°C and 8 kVmm^{-1} . While epoxy and PU composites have already reached about 80 % of their maximum d_{33} , only 60 % is obtained by PDMS composites.

In conclusion, PDMS can act as excellent matrix material to reach high piezoelectric constants if the right conditions are met. It requires more time to pole compared to epoxy and PU, and it also requires a certain threshold of electric field before the d_{33} starts to increase drastically. However, this does not answer the question why it outperforms epoxy and PU at all, as the opposite is expected due to the low value of ϵ_m of PDMS itself.

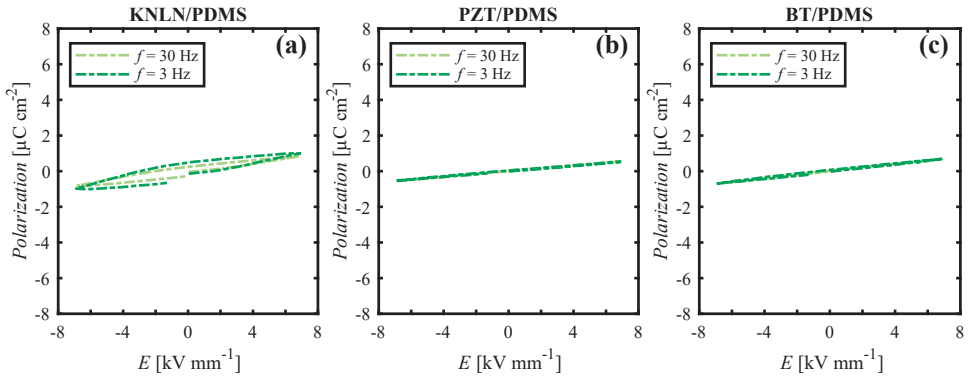


Figure A3: Hysteresis loops of (a) KNLN/PDMS, (b) PZT/PDMS and (c) BT/PDMS composites, all containing 50 vol% ceramic filler, varying the applied AC electric field frequency. All measurements are performed at the poling temperature of 120 °C. In all cases the electric field starts at zero, then first goes to the maximum, then down to the minimum, and finally back to zero.

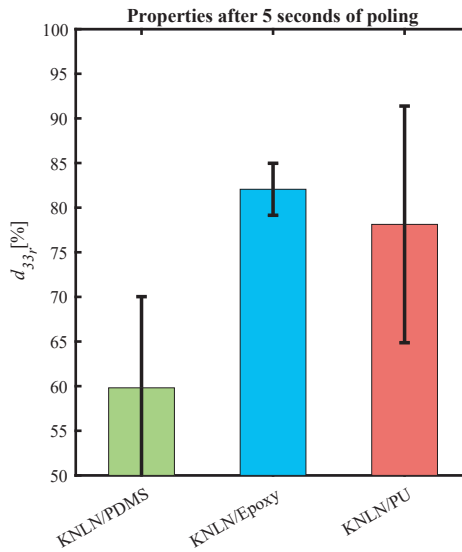


Figure A4: Relative piezoelectric charge constant, $d_{33,r}$, reached after only 5 seconds of poling. All composite contain 40 vol% of KNLN filler particles, and were poled at the poling temperature of 120 °C and electric field of 8 kV mm⁻¹.

3

FLEXIBLE LEAD-FREE PIEZOELECTRIC COMPOSITE MATERIALS FOR ENERGY HARVESTING APPLICATIONS

Vibrational piezoelectric energy harvesters are being investigated to replace batteries in embedded sensor systems. The energy density that can be harvested depends on the figure of merit, $d_{33}g_{33}$, where d_{33} and g_{33} are the piezoelectric charge and voltage constant. Commonly used piezoelectric materials are based on inorganic ceramics, such as lead zirconium titanate (PZT), as they exhibit high piezoelectric constants. However, ceramics are brittle, leading to mechanical failure under large cyclic strains and, furthermore, PZT is classified as a Substance of Very High Concern (SVHC). To circumvent these drawbacks, we fabricated quasi 1-3 potassium sodium lithium niobate (KNLN) ceramic fibers in a flexible polydimethylsiloxane (PDMS) matrix. The fibers were aligned by dielectrophoresis. We demonstrate for the structured composites values of $d_{33}g_{33}$ approaching $18 \text{ pm}^3 \text{ J}^{-1}$, comparable to that of state-of-the-art ceramic PZT. This relatively high value is due to the reduced inter-particle distance in the direction of the electric field. As a confirmation, the stored electrical energy for both material systems was measured under identical mechanical loading conditions. The similar values for KNLN/PDMS and PZT demonstrate that environmentally friendly, lead-free, mechanically compliant materials can replace state-of-the-art environmentally-less-desirable ceramic materials in piezoelectric vibrational energy harvesters.

3.1. INTRODUCTION

More and more embedded sensor systems are employed in our daily lives, such as medical implants, structural health monitoring in civil infrastructure, and the internet of things. These systems are normally powered by batteries, which need to be replaced or recharged, pollute the environment once thrown away, and are in general volumetrically the largest component of the sensor system. One way of dealing with this drawback, is to eliminate the battery and use energy harvesting instead; extracting energy from the surrounding environment and in-situ converting it into electrical energy [60, 80].

3

Depending on the application, our natural environment offers several forms of energy to be converted, such as solar power, wind energy, flowing water and mechanical energy. Here we focus on harvesting mechanical energy, such as vibrations from machines, repetitive body motion or small scale impact [81, 82]. Possible methods that can be used are electrostatic or electromagnetic induction and piezoelectricity [62, 83]. Current emphasis is on piezoelectric materials as they can directly convert mechanical energy into electrical energy, leading to harvesters with high energy density at small volume, while they are also easy to integrate into systems due to their design flexibility [84, 85].

The output of a vibrational harvester strongly depends on the boundary conditions of the applied mechanical load. Numerous mechanical designs are used to optimize the strain per unit of load, such as bimorph cantilevers, unimorph diaphragms and cymbal transducers, but a high strain is a device attribute and does not automatically imply a high energy density. In order to compare the performance of piezoelectric materials themselves, the product of the piezoelectric charge constant, d_{33} , and the piezoelectric voltage constants, g_{33} , is being used [64, 86]. This figure of merit, $d_{33}g_{33}$, is a measure of the energy density per unit volume that can be harvested. We note that $d_{33}g_{33}$ is equal to $d_{33}^2/\epsilon_r\epsilon_0$, where ϵ_0 is the permittivity of vacuum and ϵ_r is the dielectric constant.

Not surprisingly, therefore, commonly used piezoelectric materials are based on inorganic ceramics, such as lead zirconium titanate (PZT), due to the high values of the piezoelectric constants, i.e. $d_{33}g_{33}$ is about $10 - 22 \text{ pm}^3 \text{ J}^{-1}$, and high Curie temperature, i.e. T_c is about $160 - 370^\circ \text{C}$. However, PZT and related materials have two drawbacks [19, 20, 61]. Firstly, ceramics are brittle, leading to mechanical failure under large cyclic strains. Secondly, due to the presence of Pb, the commonly used inorganic piezoelectric material PZT is classified as a Substance of Very High Concern (SVHC) according to the European Community REACH regulation 1907/2006/EEC. To circumvent these drawbacks, alternative non-toxic piezoelectric materials are being investigated. Piezoelectric polymers, such as polyvinylidene-fluoride (PVDF) and its copolymers, have the advantage of being flexible. This implies that large cyclic strains can be repetitively applied without deterioration of the reliability. However, the application of piezoelectric polymers is hampered due to their limited energy harvesting potential, as $d_{33}g_{33}$ is only $5 \text{ pm}^3 \text{ J}^{-1}$. Furthermore, they exhibit a low Curie temperature of about 100°C , and require a high coercive field for poling of 60 MVm^{-1} [27, 28]. Here we demonstrate that piezoelectric composites are a worthwhile alternative.

Piezoelectric composites combine an (inert) polymeric matrix with a piezoelectric ceramic filler [30–32]. The polymeric matrix yields the mechanical flexibility. At a low volume fraction of piezoelectric filler, up to about 10 percent, the Young's modulus of a piezoelectric composite is comparable to that of the polymeric matrix. The ceramic filler renders the composite piezoelectric. The charge constant, d_{33} , increases with filler volume fraction. More importantly however, the charge constant strongly depends on the connectivity, defined as the number of dimensions in which a phase is self-connected [33]. For a composite containing two phases, there are sixteen connectivity patterns, which range from 0-0, where neither phase is self-connected, to 3-3, where each phase is self-connected in three dimensions. In this convention, the first digit refers to the active piezoelectric ceramic phase, while the second digit refers to the polymeric matrix. Representative connectivity schemes are presented in Fig. 3.1a. A 0-3, or random, composite is easy to fabricate. However, at low volume fraction of ceramic particles, the electric field is confined in the low dielectric constant polymeric matrix. There is no electric field over the disconnected piezoelectric particles and, therefore, at low volume fractions a random composite is hardly piezoelectric [79, 87]. On the other hand, a 1-3 composite contains continuous ceramic pillars. The composite therefore exhibits larger piezoelectric constants, but the main drawback is the difficult manufacturing route, as it entails cutting and refilling ceramics [88, 89]. A method to combine the easy manufacturing of the 0-3 composite with the piezoelectric properties of the 1-3 composite is to align discrete ceramic particles in the polymeric matrix while it is in a low viscosity state, obtaining quasi 1-3, or structured, particle composites. By doing this, the inter-particle distance in the field direction is reduced significantly. The smaller the inter-particle distance, the higher the electromechanical coupling. In practice this can be realized in two ways. Firstly, the filler particles can be aligned, the distance between the filler particles is then smaller than in a random composite. Secondly, the number of interconnects can be minimized, for instance by the use of high aspect ratio fibers instead of spherical particles. The limiting case is then again a 1-3 composite. Consequently, at low volume fractions, the improved connectivity of the filler particles rapidly improves d_{33} with volume fraction. At higher volume fractions, the d_{33} increases less and less [36, 37, 87].

Contrary to the charge constant, the dielectric constant, ϵ_r , experiences only a marginal increase due to alignment of the particles. The dielectric constant is dominated by that of the polymeric matrix, hardly depends on the microstructure and increases approximately linearly with the volume fraction of ceramic particles. As an illustration we calculated the figure of merit, $d_{33}g_{33}$, as a function of filler volume fraction for 0-3, 1-3 and quasi 1-3 composites. There are various models that describe ϵ_r and d_{33} as a function of filler volume fraction [79, 87, 90, 91]. All these models give comparable values [65]. We arbitrarily used the Yamada model for random composites, and the Van den Ende model (for d_{33}) in combination with the Bowen model (for ϵ_r) for the structured composites. Using these models, the lines in Fig. 3.1b are calculated. The product $d_{33}g_{33}$ depends on numerous parameters, such as the dielectric constant of matrix and filler, bulk piezoelectric charge constant, poling efficiency, aspect ratio of particles and fibers,

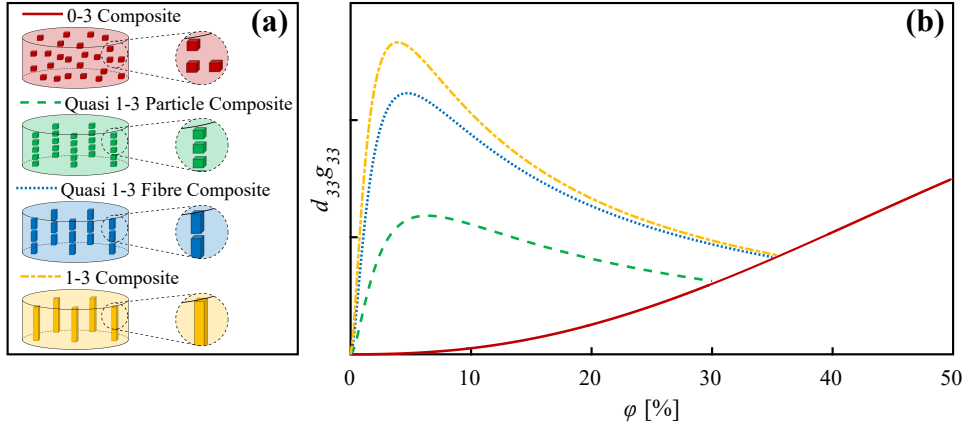


Figure 3.1: (a) Representative connectivity schemes of piezoelectric composite materials. (b) As an illustration, we present the energy harvesting figure of merit, $d_{33}g_{33}$, as a function of volume fraction, ϕ , of piezoelectric filler. The lines are calculated using, arbitrarily, the Yamada model [79] for a random composite, and the Van den Ende model [87] and the Bowen model [90] to calculate d_{33} and ϵ_r , respectively, for structured composites. Model parameters were kept constant as much as possible, to arrive at a qualitative picture in arbitrary units. The piezoelectric properties of the various 1-3 composites are anisotropic. Here we present the longitudinal piezoelectric constants.

and the inter-particle distance. The parameters were kept constant as much as possible to give the qualitative representation of Fig. 3.1b. We note that, at high volume fraction, the predicted value of $d_{33}g_{33}$ of structured 1-3 composites is lower than that of random 0-3 composites. This counterintuitive behaviour is an artefact of the theoretical models; for instance at high volume fraction the dielectric constant is over-estimated. It has been experimentally shown that at high volume fraction alignment is not advantageous for the piezoelectric constants [35]. Therefore, in Fig. 3.1b, at high volume fraction all models should converge to that of the random 0-3 composite.

For a random composite the value of $d_{33}g_{33}$ is small, and monotonically increases with filler volume fraction, as shown in Fig. 3.1b. As expected, a structured composite exhibits a higher value in the low volume fraction region. The figure of merit peaks at about 5 – 10 vol% due to the steep increase of the charge constant at low filler volume fractions. The maximum value of $d_{33}g_{33}$ increases with decreasing inter-particle distance, from quasi 1-3 particle composites, through quasi 1-3 fiber composites [34], to 1-3 composites. Fig. 3.1b clearly shows that, due to the decreased inter-particle distance, the fiber composites are preferred over particle composites. Composites for energy harvesting should preferably comprise a low volume fraction of aligned piezoelectric fibers in polymeric matrix with a low dielectric constant.

Here we fabricate state-of-the-art piezoelectric quasi 1-3 fiber composite materials. We used aligned $\text{K}_{0.485}\text{Na}_{0.485}\text{Li}_{0.03}\text{NbO}_3$ (KNLN) fibers as an environmentally friendly, lead free ceramic filler. Polydimethylsiloxane (PDMS) is used as the polymeric matrix, since it has a low dielectric constant. The Young's modulus of a few MPa leads to

mechanically flexible composites, which can handle multiple cyclic strains without affecting the reliability. The KNLN fibers are aligned through dielectrophoresis, which entails the application of an AC electric field while the polymeric PDMS matrix is still in its liquid state [90, 92]. After alignment, to minimize the inter-particle distance, the PDMS is cured to fix the microstructure. The fabricated piezoelectric fiber composites are fully characterized as a function of filler volume fraction. To compare the fiber composites with state-of-the-art PZT, we measured the output energy in the simple boundary condition of a clamped disc. Although the output energy using this configuration is limited, this is the only reliable way to compare piezoelectric materials [64].

3.2. FABRICATION OF ALIGNED KNLN/PDMS COMPOSITES

This section discusses the preparation of the piezoelectric ceramic fibers (3.2.1) and the alignment of these fibers in the polymer matrix (3.2.2).

3.2.1. PREPARATION OF KNLN FIBERS

Green $\text{K}_{0.485}\text{Na}_{0.485}\text{Li}_{0.03}\text{NbO}_3$ (KNLN) powder was obtained from CeramTec, Ruabon, UK, and calcined at $800\text{ }^\circ\text{C}$ for 2 h (heating rate of $1\text{ }^\circ\text{Cmin}^{-1}$) to decompose the starting oxides and to obtain a single phase material. Afterwards, the powder was milled using 10 mm yttria-stabilized ZrO_2 balls immersed in cyclohexane. The KNLN particles were mixed in a 20 wt% solution of cellulose acetate (MN 30000, Aldrich Chemistry) in acetone, with a volume ratio of KNLN particles to cellulose acetate of 1:1. The mixture was used to spin fibers using the wet spinning technique in a water coagulation bath. After spinning, the fibers were dried and sintered at $1050\text{ }^\circ\text{C}$ for 1 h (heating rate of $5\text{ }^\circ\text{Cmin}^{-1}$) in a closed Al_2O_3 crucible. To allow dielectrophoretic alignment, the fibers were broken into short fragments. A field emission scanning electron microscope (SEM) (JEOL, JSM-7500F, Nieuw Vennep, the Netherlands) was used to determine the fiber thickness and fiber morphology, presented in Fig. 3.2a. It shows that the fibers have a kidney-like cross-sectional shape caused by evaporation of acetone. The fibers have a diameter of $27\text{ }\mu\text{m}$ by $54\text{ }\mu\text{m}$ and a length of about $150 - 200\text{ }\mu\text{m}$, yielding an aspect ratio between 3 and 4.

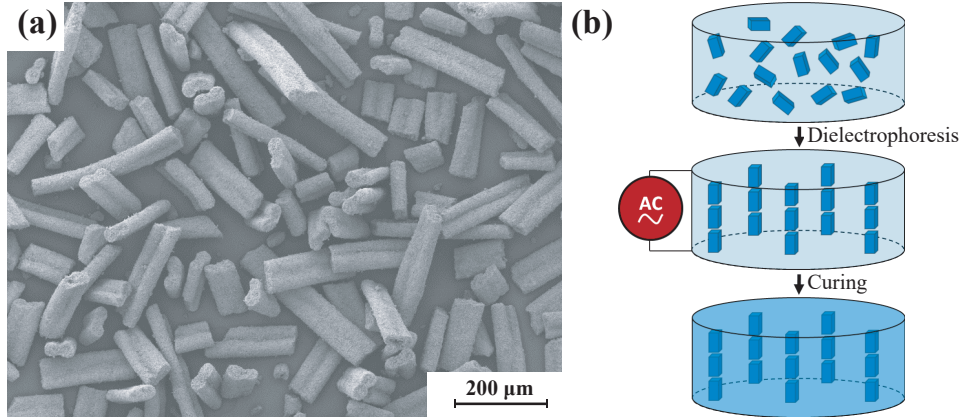


Figure 3.2: (a) SEM micrograph of the sintered KNLN fibers. (b) Schematic representation of the alignment of the piezoelectric fibers using dielectrophoresis.

3.2.2. DIELECTROPHORETIC ALIGNMENT OF KNLN FIBERS

The fibers were mixed in two component polydimethylsiloxane (PDMS) (Sylgard 184, Dow Corning) with varying volume fraction (1 – 8 vol%) in a planetary speed mixer (DAC 150 FVZ, Hauschild, Germany). The slurry was degassed and poured into prefabricated holes punched into a Teflon sheet. The sheet was covered with two aluminum foils on both sides, acting as electrodes for dielectrophoresis, and clamped between two steel plates.

Dielectrophoresis has proven to be a well-suited technique to align a piezoelectric ceramic filler as the active phase, into a low dielectric polymeric matrix as passive phase [36, 37, 87]. The process is schematically depicted in Fig. 3.2b. An AC electric field of 4 kVmm^{-1} was used. The alignment efficiency of dielectrophoresis can be obtained from the phase angle between the applied voltage and leakage current, which depends on frequency. The equivalent electrical circuit of the dielectrophoretic setup is basically a resistor, originating from the uncured polymeric part of the sample, in parallel with a capacitor, originating from the piezoelectric filler part of the sample. At high frequency the capacitor is shorted and there is no driving force for filler particles to align. On the other hand, at low frequencies the direct current through the uncured polymer matrix becomes dominant, reducing the effective electric field on the filler particles. The optimal frequency is obtained when the phase angle in the uncured composite slurry is 90° . The system then is almost purely capacitive, with minimal leakage current. Here, the frequency was varied from 1 Hz to 10 kHz. We obtained, at a frequency of 200 Hz, a maximum angle of about $83^\circ - 85^\circ$, close to the optimum obtainable angle of 90° .

After alignment, the composites were cured at 100°C for 1.5 h to permanently fix the fiber orientation. The AC field remained turned on to prevent sedimentation. The fiber alignment can be inferred from optical images of cross sections of the structured composites. Numerous cross sections of all the volume fractions were investigated.

The optical images are identical, all samples fabricated are macroscopically homogeneous. To demonstrate the details of the microstructure, we present enlarged images of the full cross sections in Fig. 3.3a.

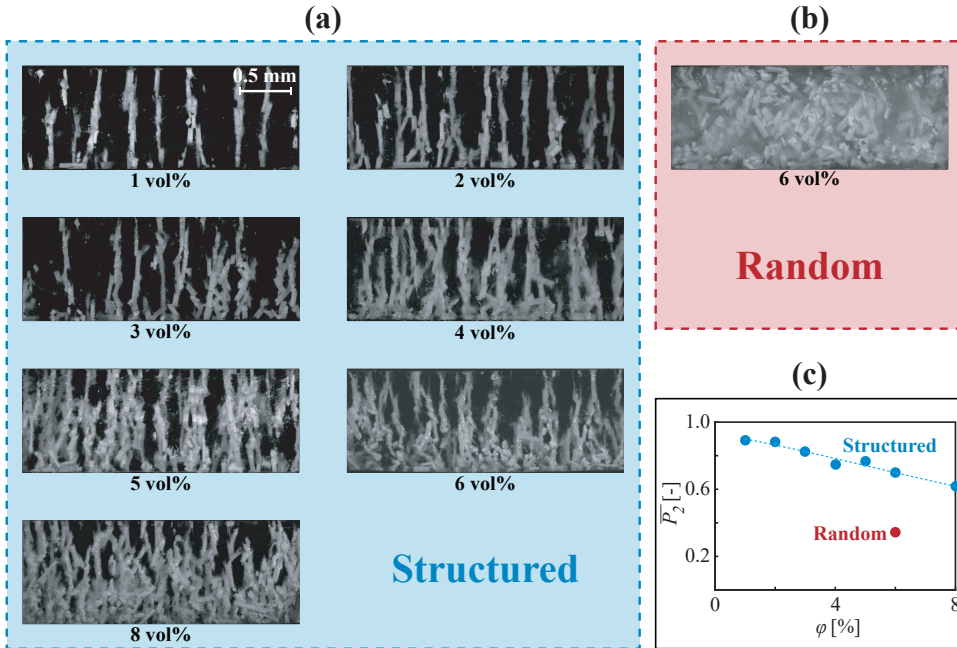


Figure 3.3: Microstructure of dielectrophoretically aligned KNLN fibers in a PDMS matrix. (a) Optical micrographs of cross sections of structured composites as a function of volume fraction. (b) Optical micrograph of the cross section of a random composite. (c) Orientational order parameter, $\overline{P_2}$, as a function of volume fraction, φ . The dotted line is a guide for the eye.

For all volume fractions investigated, i.e. 1 – 8 vol%, the fibers form clear bridges between the top and bottom electrode. However, the alignment decreases with increasing filler volume fraction. Furthermore, gravity effects cannot be fully suppressed; especially at high volume fraction the bottom part of the sample shows more fibers than the top part. To quantify the alignment of the KNLN fibers we extracted the orientational order parameter as the average of the second Legendre polynomial [93]:

$$\overline{P_2} = \overline{\frac{3}{2} \cos^2 \beta - \frac{1}{2}} \quad (3.1)$$

where β is the angle between the fiber chain and the surface normal, which is equal to the direction of the applied electric field. The order parameter varies between 0 for isotropic materials to 1 for perfectly aligned fiber composites. The experimental values of β is determined using ImageJ software. The experimental order parameter is calculated using the found values of β , and is presented as function of filler volume fraction as shown in Fig. 3.3c. It shows a monotonic decrease from 0.9 to 0.6 for volume

fractions between 1 – 8 vol%. Apparently, at higher volume fractions, the fibers obstruct each other's rotation and lateral displacement, which hampers quasi-fibre formation [94]. As reference, a random composite has been prepared with 6 vol% filler. No electric field was applied and during curing the mold was turned upside down every 10 min to prevent sedimentation. The optical image of the cross section is presented in Fig. 3.3b. The extracted order parameter is only 0.3, significantly lower than 0.6 for the structured composite, which shows that dielectrophoresis is a versatile method to align piezoelectric fibers in a polymeric matrix.

3.3. PIEZOELECTRIC CONSTANTS OF ALIGNED KNLN/PDMS COMPOSITES

To make the ferroelectric materials and composites act piezoelectrically, poling is required. To that end, capacitors were fabricated by sputtering gold electrodes through a shadow mask on both sides of the composites with a sputter coater (Quorum Q300T, East Sussex, United Kingdom). We performed numerous poling experiments where the poling time, the poling temperature and the applied electric field was varied deliberately. The optimal conditions obtained were an electric field of 15 kVmm^{-1} , a temperature of 150°C and a poling time of 5 min. Increase in the poling time did not lead to higher values of the piezoelectric constants of the present composites. We note that the constants obtained are in perfect agreement with reported poling studies on comparable KNLN/PDMS composites [37, 75]. Subsequently, the composites were aged for at least 24 h before measuring the piezoelectric constants.

The piezoelectric charge constant, d_{33} , is measured with a Berlincourt-type piezometer on poled capacitors (PM300, Piezotest, London, UK). Rounded anvils are used with a radius of 16 mm. A static force of 10 N is applied, under a 0.25 N peak-to-peak sinusoidal excitation at 110 Hz. We note that the extracted value of d_{33} depends on the boundary conditions, such as the sample aspect ratio [76]. Here all measurements have been performed under identical conditions using rounded anvils. Therefore the extracted values of d_{33} can be directly compared, resulting in a reliable material comparison. The capacitance and dielectric loss are measured at 1 kHz and 1 V with an Agilent 4263B LCR meter (Santa Clara, CA, USA). The dielectric constant, ϵ_r , measured under zero stress, was derived from the capacitance.

Piezoelectric- and dielectric constants of the capacitors are measured as a function of volume fraction. Extracted data points are presented in Fig. 3.4. Blue circles refer to structured quasi 1-3 fiber composites, and red squares refer to random 0-3 fiber composites. The dash-dotted lines are a guide for the eye, calculated with the same arbitrary models as used in Fig. 3.1. The dielectric constant, ϵ_r , and the corresponding dielectric loss, $\tan(\delta)$, as a function of filler volume fraction, φ , are shown in Fig. 3.4a and 3.4b, respectively. The dielectric constant linearly increases with volume fraction due to the dielectric constant of the KNLN fiber being orders of magnitude larger than that of the PDMS matrix. The dielectric constant increases upon alignment, as com-

only observed in dielectrophoretically aligned composites [35–37, 87]. Meanwhile, in all cases the dielectric loss does not exceed 3%, and slightly increases with alignment. The piezoelectric charge constant monotonically increases with volume fraction, shown in Fig. 3.4 c. Furthermore, the values strongly increase upon aligning the fibers. As the increase in charge constant is non-linear, the piezoelectric voltage constant, shown in Fig. 3.4 d, and $d_{33}g_{33}$, shown in Fig. 3.4 e, show a maximum at a volume fraction of only 3 – 6 vol%. The maximum value for $d_{33}g_{33}$ is $18 \text{ pm}^3 \text{ J}^{-1}$, the value of which will be compared to classical bulk ceramics in the next section. To demonstrate the important role of the inter-particle distance, we include as the green triangles, data previously obtained for dielectrophoretically aligned quasi 1-3 KNLN/PDMS particle composites. The piezoelectric constants are in between those of random and aligned fiber composites, in perfect agreement with the qualitative picture of Fig. 3.1. The same trend is supported by reported data on PZT composites [34], which clearly demonstrates that piezoelectric properties can be optimized by using aligned fiber composites.

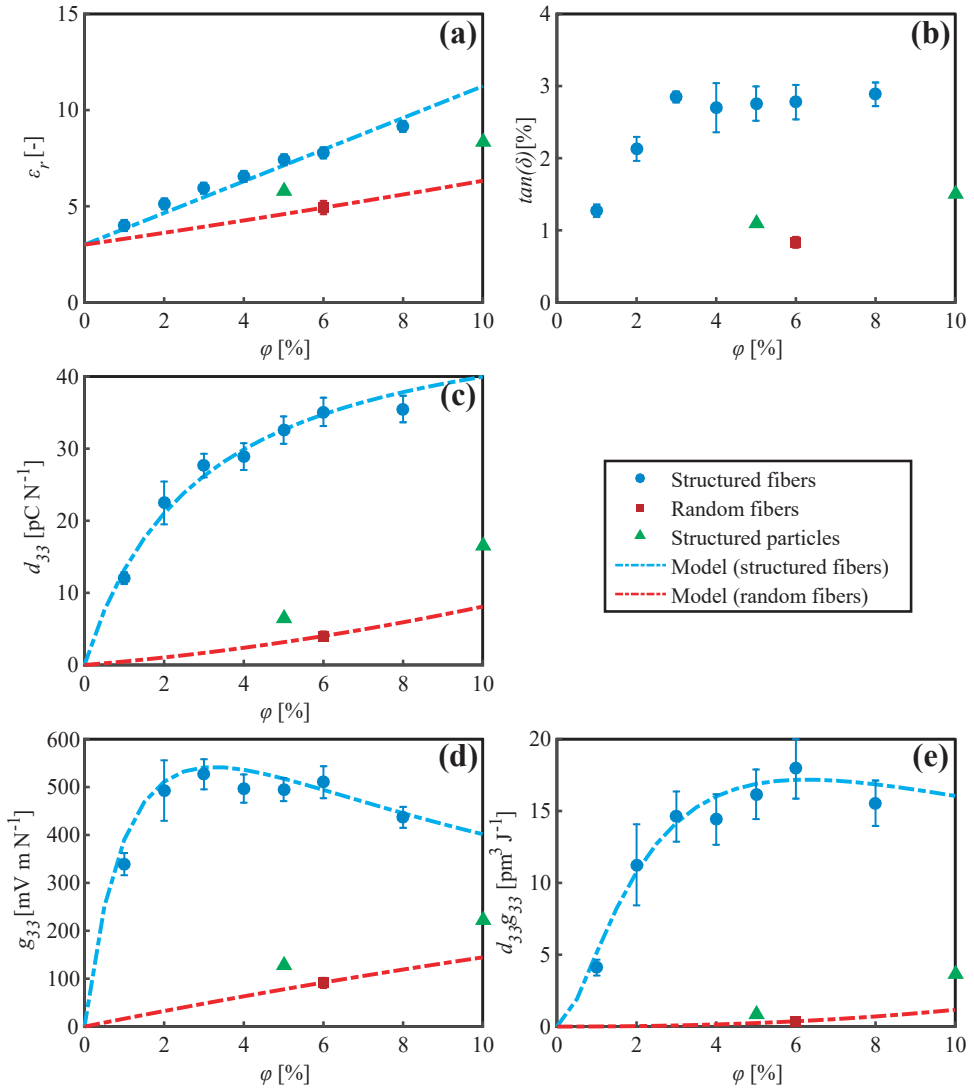


Figure 3.4: Piezoelectric- and dielectric constants of random 0-3 and structured quasi 1-3 KNLN/PDMS fiber composites as a function of KNLN volume fraction, ϕ . Blue circles refer to structured composites and red squares refer to random composites. (a) The dielectric constant, ϵ_r , (b) the dielectric loss, $\tan(\delta)$, (c) the piezoelectric charge constant, d_{33} , (d) the piezoelectric voltage constant, g_{33} , (e) the stress energy density, $d_{33}g_{33}$. For comparison, reported data of quasi 1-3 particle KNLN/PDMS composites are included as the green triangles [37]. The dash-dotted lines are a guide for the eye, calculated with the same models as used in Fig. 3.1.

3.4. COMPARISON OF PIEZOELECTRIC MATERIALS

Table 3.1 gives an overview of a representative number of reported piezoelectric materials. The materials in the table range from bulk materials, through random composites and structured particle and fiber composites, to a 1-3 composite. The ceramic filler comprises lead titanate (PT), PZT and KNLN, and as polymeric matrix PDMS, polyurethane (PU) and epoxy are used. The entries are sorted by $d_{33}g_{33}$. The table shows that bulk ceramic materials typically have a high d_{33} value. However, the large dielectric constant severely limits the g_{33} values. Consequently, for bulk ceramics $d_{33}g_{33}$ varies from 2 to $22 \text{ pm}^3 \text{ J}^{-1}$, where the state-of-the-art value is obtained with PZT507. On the other hand, composites exhibit lower values of d_{33} , but due to the low dielectric constant of the polymeric matrix, their g_{33} reaches state-of-the-art values up to 500 mV mN^{-1} . We note that the 1-3 composite from the table is an exception to this rule due to the high volume fraction and perfect alignment. This causes the d_{33} to be high while the g_{33} stays low, comparable to bulk ceramics.

As stated earlier, for composites the value of $d_{33}g_{33}$ strongly depends on the microstructure. Random composites are piezoelectric, especially at high volume fractions. However, the mechanical flexibility then is impaired. The value of d_{33} can be dramatically improved by aligning the ceramic filler. Due to the low dielectric constant of the composite, g_{33} , and therefore $d_{33}g_{33}$, peak at low volume fractions. The maximum value depends on the inter-particle distance, and therefore, aligned fiber composites are preferred over aligned particle composites. Table 3.1 shows that the highest value obtained with composites is $18 \text{ pm}^3 \text{ J}^{-1}$ for structured KNLN fibers in PMDS. This value is comparable to state-of-the-art PZT ceramics. Additionally, due to the low volume fraction, structured composites remain mechanically flexible, which gives an additional degree of freedom to optimize a vibrational harvester.

To verify the high value of $d_{33}g_{33}$, obtained for the aligned KNLN/PDMS fiber composite, we measured the output energy under sinusoidal mechanical excitation in a recently developed piezometer system [64]. The output energy is subsequently compared to that of state-of-the-art ceramic, PZT507 [72], measured under identical conditions.

The electrical output of an energy harvester increases linearly with the mechanical input energy. This input energy strongly depends on the mechanical boundary conditions. The differences between a clamped disc, a bimorph cantilever, unimorph diaphragms or cymbal transducer can easily differ by many orders of magnitude. Here we measured the stored electrical energy of different material classes in the simple boundary condition of a clamped disk. We stress that this is experimentally the only way to reliably compare a variety of piezoelectric materials under identical conditions. However, we note that this clamped condition is the least efficient at transferring the applied load into elastic strain energy.

The piezometer system is schematically depicted in Fig. 3.5a. The metallized capacitor is placed between two rounded anvils. Rounded anvils are used with a radius of

Table 3.1 : Piezoelectric constants of representative piezoelectric materials, ranked on the value of $d_{33}g_{33}$.

Piezoelectric material	Matrix material	Connectivity	φ [%]	d_{33} [$\mu\text{C}\text{N}^{-1}$]	g_{33} [$\text{mV}\text{m}\text{N}^{-1}$]	$d_{33}g_{33}$ [$\text{p}\text{m}^3\text{J}^{-1}$]	Reference
PZT507		Bulk	100	875	25	21.9	This work ^(a)
Structured KNIN fiber	PDMS	Quasi 1-3	6	35	510	17.9	This work
PT-BFMn	Epoxy	0-3	65	65	230	15.0	[95]
PZT Pillars	Epoxy	1-3	48	475	29	13.8	[96]
PZT5A4		Bulk	100	460	28	12.9	[72]
Structured PZT fibers	PU	Quasi 1-3	5	27	277	7.5	[34]
PVDF		Bulk	100	23	220	5.1	[97]
Structured KNIN particles	PDMS	Quasi 1-3	10	17	220	3.7	[37]
Structured KNIN particles	Epoxy	Quasi 1-3	10	20	180	3.6	[36]
KNN		Bulk	100	120	27	3.2	[98]
BaTiO ₃		Bulk	100	191	11	2.1	[61]
Structured PZT particles	Epoxy	Quasi 1-3	20	10	70	0.7	[87]

^(a) Sintered ceramic disks obtained from CeramTec, Ruabon, UK.

16 mm, identical to the anvils used in the Berlincourt measurement. The PZT507 and KNLN/PDMS samples have a similar surface area of 50 mm² and a similar thickness of 1 mm. The diameter of the anvils is identical to the diameter of the composites. An inductive voice coil supplies a static force of 10 N and a dynamic force of 3 N peak-to-peak, at a frequency of 1 Hz, shown in Fig. 3.5b.

The short circuit current, I_{sc} , is measured using an ultra-low noise amplifier that virtually shorts the sample. The short circuit current is presented in Fig. 3.5c. The current is the derivative of the mechanical force, which explains the observed phase shift between Fig. 3.5b and 3.5c. The short circuit current scales with the value of d_{33} , which explains the higher current of PZT507 compared to KNLN/PDMS. The open circuit voltage, V_{oc} , is measured with an electrometer, and is presented as a function of time in Fig. 3.5d. The voltage is the second derivative of the applied mechanical force, which for a sinusoidal excitation is equal to the original waveform. The output voltage scales with g_{33} , and therefore, a higher voltage is observed for the KNLN/PDMS. The stored electric energy per unit volume, U_{oc} , is calculated from the open circuit voltage by:

$$U_{oc} = \frac{C_p V_{oc}^2}{2A_{elec} t_{disk}} \quad (3.2)$$

where C_p is the sample capacitance, A_{elec} the electrode area and t_{disk} the thickness. The stored electrical energy is presented as a function of time in Fig. 3.5e and 3.5f, for KNLN/PDMS and PZT507, respectively. From U_{oc} , the value of $d_{33}g_{33}$ can be derived, which perfectly agrees with the values presented in Fig. 3.4. As U_{oc} depends on V_{oc}^2 , it oscillates at double the applied frequency. This is as expected from the comparable values of $d_{33}g_{33}$, the stored electrical energy for KNLN/PDMS is comparable to that of PZT507.

We note that the energy density is low, only in the range of nWcm⁻³, due to the fact that the sample is mechanically clamped. However, in order to prevent any ambiguous interpretation, we carefully measured the stored energy in our KNLN/PDMS composite materials and PZT under exactly identical conditions. Therefore we can directly compare these two material systems for energy harvesting application. We show that the under identical clamped conditions, a similar output energy is measured for KNLN/PDMS fiber composites and PZT ceramics. This similarity demonstrates that piezoelectric composites can be a worthwhile alternative for state-of-the-art piezoelectric ceramic materials in vibrational energy harvesters.

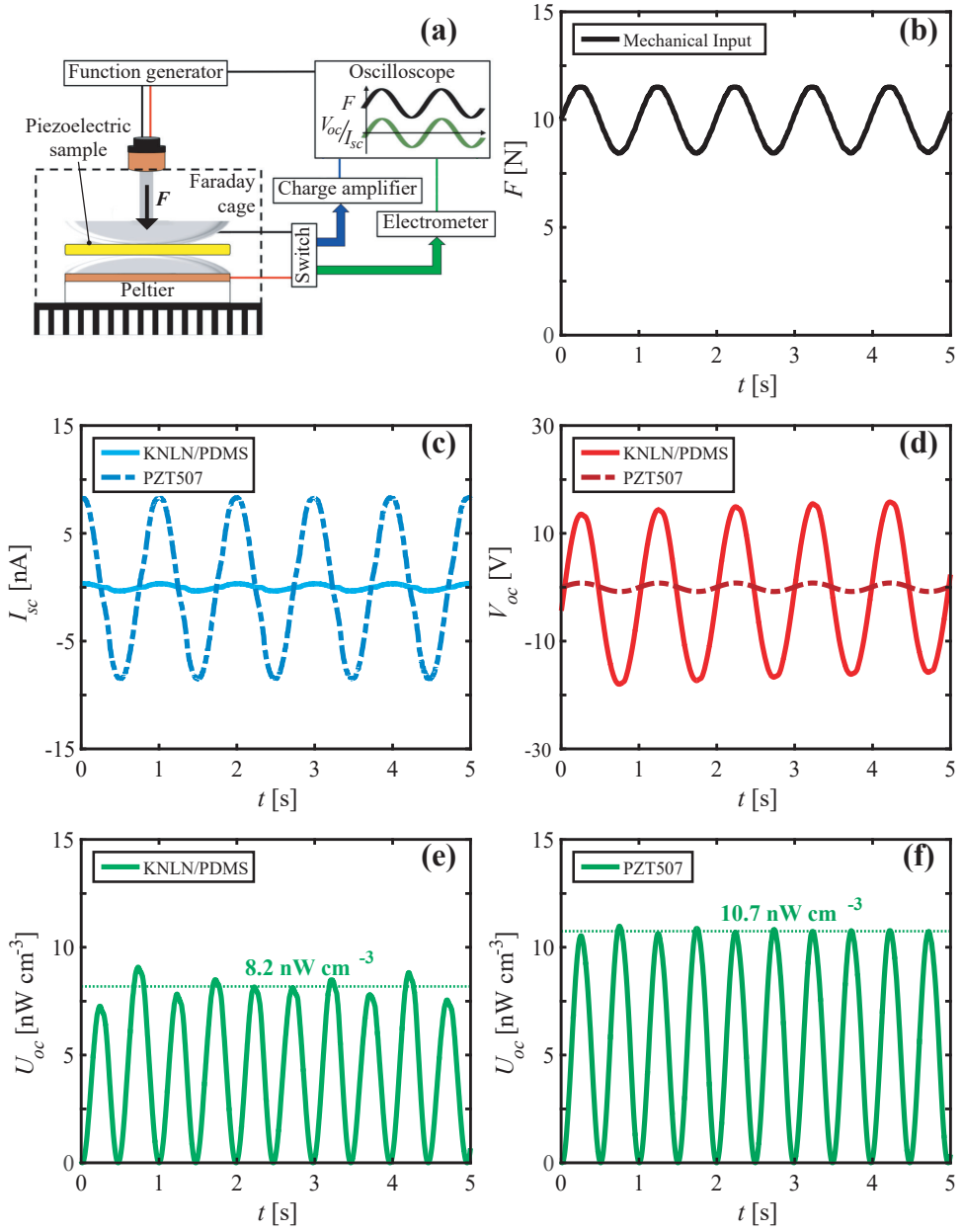


Figure 3.5: Electrical response to a mechanical input of KNLN/PDMS and PZT507, both having a thickness of 1 mm and an area of 50 mm², measured using a specifically designed piezometer system. (a) Schematic representation of the piezometer system [64], (b) the mechanical input, F , (c) the short circuit current, I_{sc} , (d) the open circuit voltage, V_{oc} , and the stored electrical energy, U_{oc} , of (e) KNLN/PDMS and (f) PZT507, respectively.

3.5. CONCLUSIONS

We fabricated quasi 1-3 aligned KNLN ceramic fibers in a PDMS matrix. The fibers were aligned by dielectrophoresis with an orientational order parameter between 0.6 and 0.9. The piezoelectric and dielectric constants were fully characterized as a function of fiber volume fraction. The figure of merit for materials to be applied in vibrational energy harvesters is $d_{33} g_{33}$. Here we demonstrate for the KNLN/PDMS composites values approaching $18 \text{ pm}^3 \text{ J}^{-1}$. This relatively high value is due to the alignment of fibers, instead of particles, leading to a strongly reduced inter-particle distance. The value of $d_{33} g_{33}$ is comparable to that of state-of-the-art PZT ceramics. Using a sensitive piezometer system, the stored electrical energy is measured under sinusoidal mechanical excitation. Under identical clamped conditions, a similar output energy is measured for KNLN/PDMS and PZT, as expected from the similar value of $d_{33} g_{33}$. This unambiguously demonstrates that environmentally friendly, lead-free, mechanically compliant materials can replace state-of-the-art brittle and damage-sensitive ceramics in piezoelectric vibrational energy harvesters.



4

PIEZOELECTRIC SENSOR PATCH TO DETECT LAMINAR-TO-TURBULENT TRANSITION ON AIRFOILS

This work presents an attempt to measure laminar-to-turbulent transition on a NACA 0012 airfoil using piezoelectric sensors. Eight piezoelectric sensors are embedded in a single patch which is bonded to the upper wing skin. The idea is to measure the pressure fluctuations occurring normal to the wing skin to locate transition using the fact that the pressure fluctuations maximize at the location of transition. The wing is tested in the Open Jet Facility of the Delft University of Technology at Reynolds numbers of 132×10^3 and 265×10^3 using angles of attack in the range of -3° to 15° . From the static angle of attack measurements we were only able to find the natural frequency of the wing. The problem originates from the strong mechanical coupling between the sensors and the wing skin. However, when changing the angle of attack while measuring, a large low frequency signal was found at transition. Further analysis revealed that the spotted low frequency signal most likely is not caused by the piezoelectric effect, but by the pyroelectric effect instead. Since this is not in the scope of this work, only a minor discussion is provided in the appendix of this chapter regarding the pyroelectric response. In order to make a piezoelectric sensor work in future experiments, we need to address the strong mechanical coupling between the sensors and wing skin, improve the piezoelectric sensitivity, and deal with the occurring pyroelectric response.

4.1. INTRODUCTION

The boundary layer plays an important role in the lift-to-drag ratio of airfoils. Typically, boundary layers can be classified as either laminar, which can be described as a flow containing non-intersecting parallel layers of air, or turbulent, which can be described as a random chaotic flow. The region in between the two, where laminar flow changes into turbulent flow, is governed by the so-called laminar-to-turbulent transition process.

Locating the transition region online is of interest due to the effect the location has on the amount of skin friction of a turbulent flow compared to a laminar flow [40]. Because of this, a way of increasing the lift-to-drag ratio of airfoils is to make sure that transition is extended as far downstream as possible. This can be achieved by applying a control loop to an overactuated morphing aircraft wing, providing excellent local control over free stream velocity and angle of attack.

4

For such a control loop to work, we require a measurement device that is able to locate transition, ideally in-situ and under relevant flight conditions. The intrinsic differences between a laminar and turbulent flow are the shear stress at the airfoil skin, the heat transfer between the air and the skin, and the magnitude of high frequency pressure fluctuations [40]. Using these differences, various measurement techniques have been developed to locate transition, such as pressure or sound transducers [49, 50, 99] hot film sensors [51–53, 100] Infrared (IR) thermography [44–46], and shear stress measurements [54, 55, 101, 102].

This work presents an introductory study to apply piezoelectric sensors to measure pressure fluctuations in a boundary layer normal to an airfoil skin. At transition, these pressure fluctuations reach a maximum, which in principle can be used to locate transition [50]. The piezoelectric sensors are applied to a NACA 0012 airfoil and tested in a wind tunnel at the Delft University of Technology. A patch containing the piezoelectric elements is manufactured and mounted on top of the airfoil. The benefit of using such a patch is that it retains the smoothness of the airfoil skin, minimizing aerodynamic influences. To verify the data obtained from the sensors, we used a stethoscope and Xfoil modeling to locate transition on the same airfoil independently [103]. Based on the results of Chapter 2 and 3 we expected that sensors consisting of piezoelectric composites work even better than monolytic PZT sensors due to their enhanced g_{33} . However, in this work we discovered (and understood) that this not the case.

4.2. METHOD

This section discusses the piezoelectric sensors installed on the wing (4.2.1), the wind tunnel experiments performed (4.2.2) and the data validation performed using a stethoscope and Xfoil (4.2.3).

4.2.1. PIEZOELECTRIC SENSORS

Eight commercially produced PZT-5A4 ceramic disks with a diameter of 8 mm, a thickness of 330 μm and a d_{33} of 400 $\text{pC}\cdot\text{N}^{-1}$ were used as piezoelectric sensors. A freestanding piezoelectric patch was manufactured embedding the piezoelectric PZT-5A4 ceramic disks in a polymeric foil. This patch was later bonded to the airfoil. The layup of this patch is shown in Fig. 4.1. The base of this patch is a 250 μm polyethylene terephthalate (PET) foil with circular cutouts with a diameter equal to that of the PZT-5A4 disks. The cutouts were diagonally arranged to prevent any turbulent wedges created by any of the piezoelectric disks to influence the measurement of another disk further downstream. A 20 μm thick aluminum foil was bonded on top of the PET as common ground electrode. The aluminum layer will be directly in contact with the airflow and was chosen to be as thin as possible. This will minimize the absorbed mechanical input to the piezoelectric sensors underneath. The aluminum foil also acts as top shielding to outside electromagnetic noise. The piezoelectric disks were bonded to the aluminum foil using conductive carbon paint. Finally, the hot electrodes were added with copper tape and wires. The total patch has a thickness of roughly 350 μm , a length of 190 mm and a width of 170 mm. The sensors have a constant spacing of 25 mm between each other in the chordwise direction.

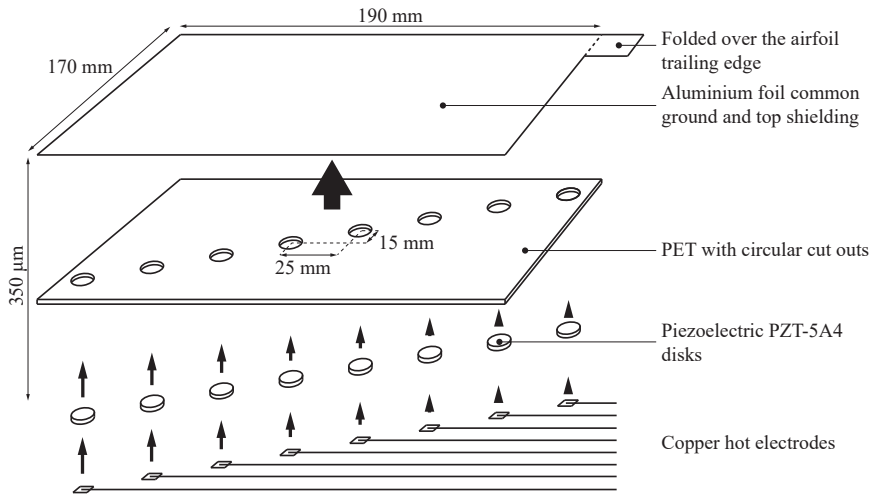


Figure 4.1: Schematic representation of the layup of the piezoelectric patch.

Once the patch was prepared, it was bonded to a carbon fiber reinforced plastic (CFRP) NACA 0012 symmetric airfoil with a chord of 0.2 m and a wingspan of 1.0 m. The positions of the eight sensors along the chord of the airfoil are given in Table 4.1. Double sided tape was used to bond the piezoelectric patch to the airfoil. The tape also acts as an electric insulator between the piezoelectric patch and the conductive CFRP airfoil. The benefit of the CFRP being conductive, is that it can be used as the bottom shielding to prevent electromagnetic noise. To connect the top and bottom shield, a piece of the aluminum foil ground electrode was folded over the trailing edge (TE) of the airfoil

to make electric contact. Upon bonding the piezoelectric patch to the airfoil, a small step near the top side of the leading edge (LE) was created due to the thickness of the piezoelectric patch. This discrete step was removed by filling the gap by plastering and grinding it.

Table 4.1: Sensor positions along the chord.

Sensor	Position x/c [-]
1	0.0875
2	0.2125
3	0.3375
4	0.4625
5	0.5875
6	0.7125
7	0.8375
8	0.9625

The signal of each independent piezoelectric sensor was sent to an ultra-low input current CMOS amplifier, providing a resistive load of 100 M Ω . The amplifier copies the voltage obtained from the piezoelectric sensor, amplifies it with a factor 2, and drives a data acquisition unit without signal loss due to wiring and circuit load. In this study, instead of installed the amplifiers within the airfoil, we decided to place the amplifiers separate from the wing on a pole behind the setup. This can be seen in Fig. 4.2. We tried to keep the wires between the sensors and the amplifiers as short as possible. This prevents losses in signal amplitude and prevents additional noise.

4.2.2. WIND TUNNEL EXPERIMENTS

The wind tunnel experiments were performed in the Open Jet Facility (OJF) of the Delft University of Technology. The OJF has a tunnel outlet of 2.85 x 2.85 m and can provide an airspeed up to 35 ms⁻¹.

The experimental setup is shown in Fig. 4.2. In the picture, the airfoil contains two patches: one is the PZT patch described this work, while the other is a patch containing piezoelectric composite discs instead of PZT ceramic disks. In Chapter 2 and Chapter 3 it is seen that piezoelectric composites generally have a high g_{33} , meaning they possess a high sensor sensitivity. We therefore decided to use such composites here. However, after testing the composite patch under the same conditions as the PZT patch it was found to only measure noise. The reason for this was the low capacitance of the composites, resulting in high signal losses in the electronic circuit containing the amplifiers behind it. Since no useful data could be extracted from the composite patch, the remainder of this chapter only focuses on the PZT patch.

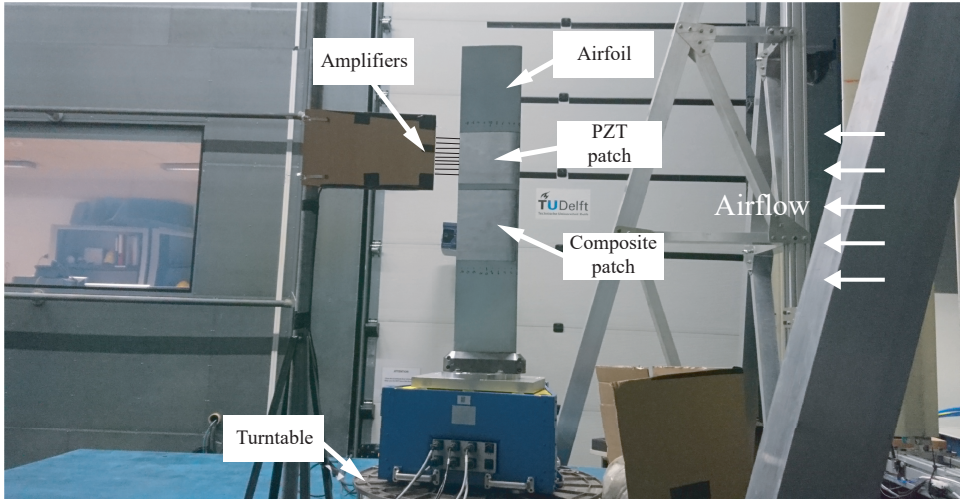


Figure 4.2: Experimental setup in the Open Jet Facility (OJF) at the Delft University of Technology.

The airfoil was placed on a turntable which allows to remotely control the angle of attack of the airfoil. Behind the airfoil a pole was placed which housed the amplifiers connected to the sensors through copper wires. During all experiments all 8 piezoelectric sensors recorded simultaneously over a time period of 30 s at a 2 kHz per channel sampling frequency. First, a set of experiments were performed keeping the angle of attack of the airfoil fixed at angles between -3° and 15° with 3° increments. These experiments were performed at an airspeed of 10 m s^{-1} and 20 m s^{-1} , which corresponds to Reynolds numbers (RE) of 132×10^3 and 265×10^3 , respectively. These Reynolds numbers were calculated using a kinetic viscosity, ν , of $1.5111 \times 10^{-5} \text{ m}^2 \text{ s}^{-1}$, and a chord length, L , of 0.2 m. Following the measurements at a static angle of attack, the angle of attack was varied during the 30 s measurement from -3° to 15° , and vice versa, with angular velocities of 1° s^{-1} , 2° s^{-1} and 5° s^{-1} . These measurements were performed at the same Reynolds numbers as the static angle of attack measurements.

4.2.3. DATA VALIDATION

In order to validate the signals obtained from the piezoelectric patch, the location of the laminar-to-turbulent transition was also obtained experimentally using a stethoscope, and numerically using Xfoil software [103].

A stethoscope measures audio, and picks up the change from the stable low-noise laminar flow to the chaotic high-noise turbulent flow. The stethoscope was attached to an audio amplifier to make transition easily detectable while shifting the stethoscope over the wing in the direction of the chord. The measurement tube was held parallel to the airfoil surface to measure the airflow locally. These measurements were performed on three spanwise locations of the airfoil: one at the composite patch, one at

the PZT patch and one in between the two patches. Only minimal differences were found. Therefore, the average of the three locations is taken. These measurements were performed at the same Reynolds numbers as mentioned before, being 132×10^3 and 265×10^3 . The angle of attack was varied from -3° to 15° with 3° increments.

Using Xfoil [103], the flow around the airfoil can be analyzed numerically. The NACA 0012 airfoil was loaded into the software, and viscous mode was activated using the Reynolds numbers as mentioned in the previous section. The same range of angles of attack was analyzed as those tested with the piezoelectric sensors. The location of transition was extracted from Xfoil for angles of attack of -3° to 15° with 1° increments.

The results of both the stethoscope measurements and Xfoil modeling are combined in Fig. 4.3. According to both the stethoscope measurements and the Xfoil data the location of transition moves towards the LE with increasing angle of attack. Increasing the Reynolds number only slightly moves transition towards the LE. The minor differences observed between the stethoscope measurements and the Xfoil data are most likely caused by the fact that Xfoil uses a perfect NACA 0012 profile, while the actual airfoil was slightly distorted due to the piezoelectric patch applied to the airfoil. This slightly increases the thickness of one side of the airfoil and might introduce some surface imperfections.

4

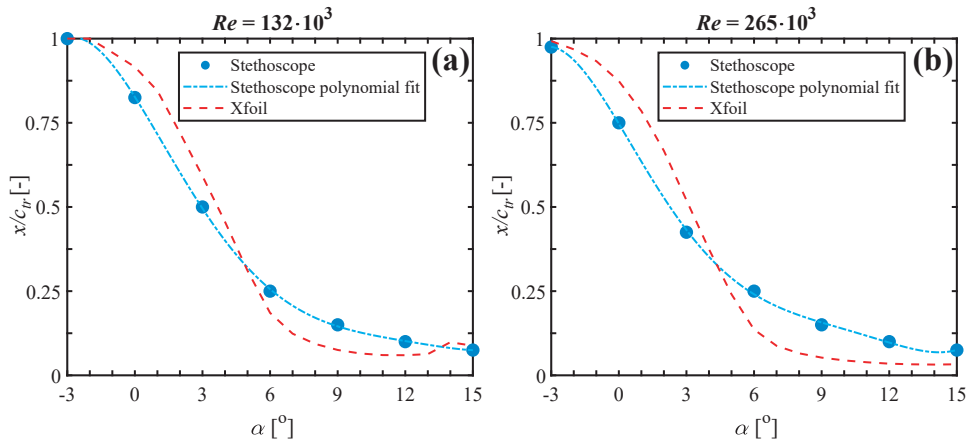


Figure 4.3: Location of transition, x/c_{tr} , versus the angle of attack, α , measured with a stethoscope and modeled using Xfoil at a Reynolds number of (a) 132×10^3 and (b) 265×10^3 .

4.3. RESULTS AND DISCUSSION

This section discusses the piezoelectric signals obtained during the static angle of attack measurements (4.3.1) and the signals obtained during the dynamic angle of attack measurements (4.3.2). These cases are discussed separately because they presented different results.

4.3.1. STATIC ANGLE OF ATTACK MEASUREMENTS

The voltages obtained from the eight sensors as a function of time, t , and signal frequency, f , are shown in Fig. 4.4. These measurements were performed at a fixed angle of attack of 0° . Sensor 1 is located near the LE, while sensor 8 is located near the TE. From the frequency graphs we clearly see two peaks: one at about 20 Hz and one near 30 Hz. These frequencies are the natural frequencies of the wing, as was confirmed simply by applying a mechanical pulse to the wing while the wind tunnel was switched off. Due to the strong mechanical coupling between the sensors and the airfoil skin all sensors clearly measure these frequencies. By increasing the free stream velocity, and hence the Reynolds number, with a factor of 2, we see that the amplitude of these frequency peaks increases with approximately a factor 4. This is expected, since the vibrations will scale with the free stream velocity squared. However, we do not see the same happening for the time domain signals, which only increase with about a factor 2. This indicates that a large fraction of the time domain signal simply contains electrostatic noise, because such noise signals will not scale with the square of the free stream velocity.

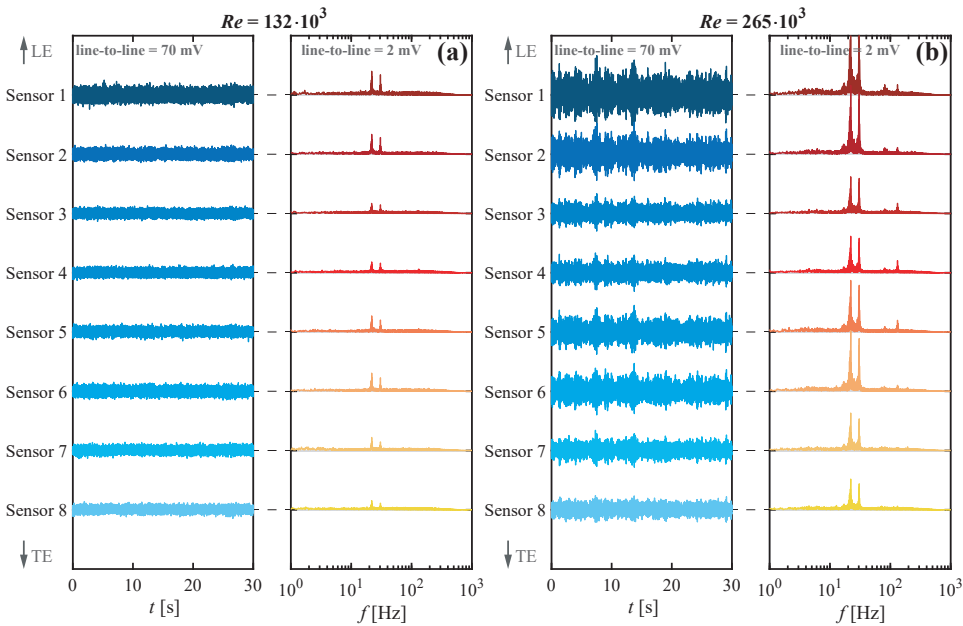


Figure 4.4: Voltage obtained from the piezoelectric sensors as a function of time, t , and frequency, f , for Reynolds numbers, Re , of (a) 132×10^3 and (b) 265×10^3 . The scaling of the two time domain graphs are the same, and the scaling of the two frequency domain graphs are the same. The exact scaling is indicated by the line-to-line voltage in the top of each graph, which signifies the vertical distance between two neighboring sensor-lines within the corresponding graph.

The voltages obtained from the sensors as a function of time, t , and angle of attack,

α , are shown together in Fig. 4.5. The measurements were performed at a constant Reynolds number of 132×10^3 . A constant amplitude is maintained through a wide range of angles of attack, from -3° to 9° . The same was observed in the frequency domain, which is not shown here. Once an angle of attack of 12° is reached, the magnitude of the signals starts to increase. These vibrations are, just like before, at frequencies of about 20 Hz and 30 Hz, which are as stated before the natural frequencies of the wing. This increase in magnitude actually occurred because of flow separation, causing more violent vibrations to occur. The NACA 0012 airfoil used in this work is known to have an abrupt stall behavior [104]. This means that at a certain angle of attack the whole wing stalls uniformly. Therefore, all the sensors detect stall at the same angle. However, the signals measured still relate to the vibrations of the wing, not to an occurrence in the boundary layer.

4

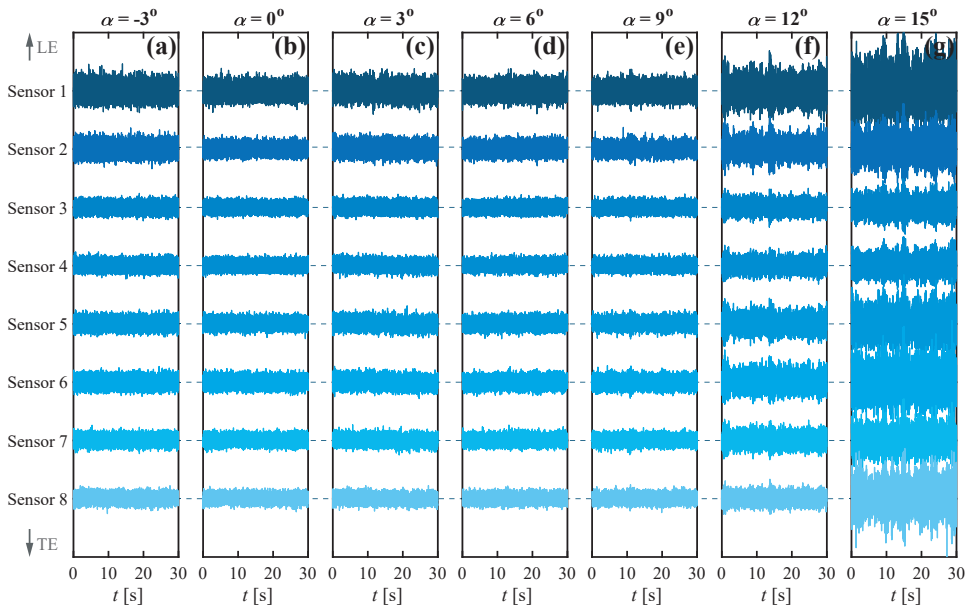


Figure 4.5: Voltage obtained from the piezoelectric sensors as a function of time, t , for angle of attack, α , of (a) -3° , (b) 0° , (c) 3° , (d) 6° , (e) 9° , (f) 12° and (g) 15° . The data shown here was measured at a Reynolds number of 132×10^3 . All the graphs have the same scaling, with a 45 mV vertical distance between two neighboring sensor-lines.

After thorough evaluation of the static angle of attack data, it can be concluded that the piezoelectric sensors only detected the vibrations occurring in the wing, while no boundary layer related phenomena are detected. This is caused by the strong mechanical coupling between the sensors and the airfoil skin.

4.3.2. DYNAMIC ANGLE OF ATTACK MEASUREMENTS

From the previous section we have seen that the mechanical coupling between the sensors and the airfoil skin is so strong that only the mechanical vibrations of the wing are measured. We therefore did not expect to see anything different in the dynamic angle of attack measurements. During these experiments, the sensors measure the output voltage while increasing the angle of attack from -3° to 15° . As it turns out, the dynamic angle of attack measurements did reveal something surprising. This can be seen from Fig. 4.6, showing the voltages obtained from the sensors as a function of angle of attack, α , while increasing α with 2°s^{-1} . Just like in the previous section we see stall occurring at high angles, signified by the simultaneous increased signal amplitude detected by all sensors.

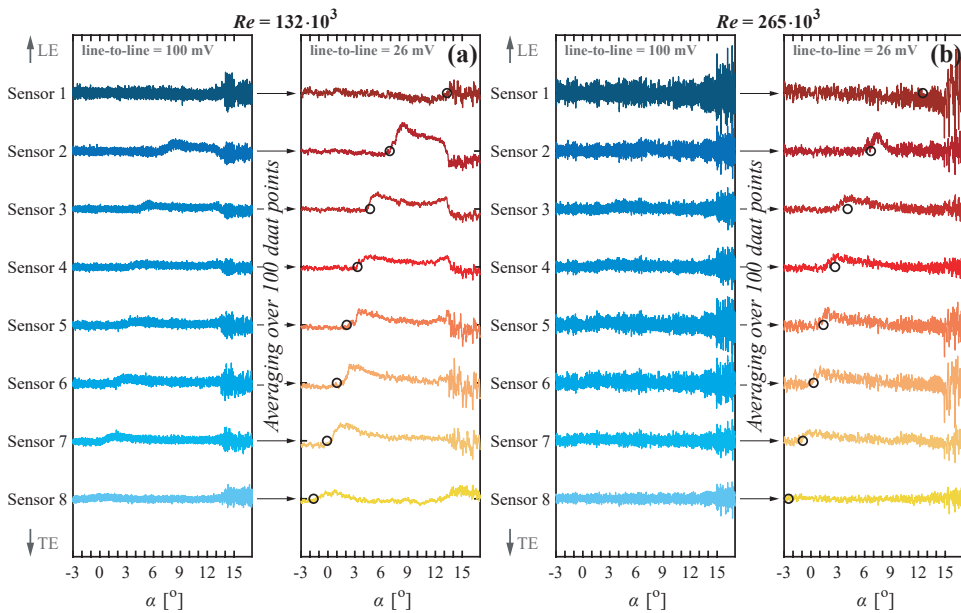


Figure 4.6: Voltage obtained from the piezoelectric sensors as a function of angle of attack, α , for Reynolds numbers, Re , of (a) 132×10^3 and (b) 265×10^3 . These measurements were taken while the angle of attack increased with 2°s^{-1} . To highlight the low frequency signals, averaging is applied to the signals over 100 data points. The scaling of the two not-averaged graphs are the same, and the scaling of the two averaged graphs are the same. The exact scaling is indicated by the line-to-line voltage in the top of each graph, which signifies the vertical distance between two neighboring sensor-lines within the corresponding graph. The black circles indicate transition which are extracted from the stethoscope polynomial fit of Fig. 4.3.

The red color coded graphs present the blue color coded data after passing them through an averaging filter, where each data point in time is calculated by taking the average over 100 data points around it. By doing so, sensors 2 up to 7 show a single low frequency wave signal, while sensors 1 and 8 show it barely or not at all. It can be seen at both Reynolds numbers that sensor 7 first experiences this signal near an angle of attack of 0° , and the signal then moves to higher angles as we move along the sensor positions.

The black circles in the graphs indicate the location of transition, which are extracted from the stethoscope polynomial fit of Fig. 4.3. The shown transition locations strongly overlap with the low frequency waves in the graphs, showing a clear relation.

Upon further assessment of the signals, we noticed that the single low frequency wave not always gave a positive sign with increasing angle of attack, or negative sign with decreasing angle of attack. Instead, this seemed to arbitrarily change from time to time. If the piezoelectric effect would be responsible for the change of sign, it would mean an increasing pressure in the one case, and a decreasing pressure in the other, which seems not possible. In addition, generally piezoelectric materials have a weak response to low frequency mechanical input signals, and therefore are less likely to produce low frequency output signals as are seen in these measurements. Hence it is not possible that we detect an actual piezoelectric response. A more likely scenario is that the low frequency signals originate from the pyroelectric effect instead.

The pyroelectric effect provides a signal as a response to a change in temperature. This requires a (small) temperature difference between the airfoil and the free stream. A change in temperature can occur on an airfoil because of the difference in heat transfer capacity of a laminar and a turbulent boundary layer [40]. When the bulk temperature of an airfoil differs from the temperature of the free stream, the temperature at the skin of the airfoil will be different in the laminar and turbulent region. In the laminar region the temperature tends to be closer to that of the bulk of the airfoil, while in the turbulent region the temperature is closer to that of the free stream. While the angle of attack is kept constant, the temperature of the airfoil and free stream only changes over long time scales, in the range of minutes. This temperature gradient is too small to be measured by the pyroelectric effect. However, when one of the sensors moves from a laminar to a turbulent region, or vice versa, an abrupt change in temperature is experienced, which potentially can be detected by the pyroelectric sensor creating low frequency signals as the ones shown in Fig. 4.6.

Since the pyroelectric effect was not in the scope of this work but still gave interesting results, an analysis about the possibility of the observed behavior being the pyroelectric effect and a further analysis about whether it actually indicates transition, is provided in Appendix 4.A and 4.B.

4.4. CONCLUSIONS AND RECOMMENDATIONS

A patch containing piezoelectric sensors is laminated onto an airfoil to measure pressure fluctuations occurring in the boundary layer, with the aim to detect transition. At static angles of attack, we were not able to see any signals suggesting boundary layer phenomena, as the measurements show only the natural frequency of the airfoil. Measuring while dynamically changing the angle of attack provided low frequency signals occurring while transition passed the corresponding sensor. These signals are however unlikely to be caused by the piezoelectric effect, and more likely occur due to the pyroelectric effect. We were therefore unable to achieve our goal to detect laminar-

to-turbulent transition using the proposed piezoelectric sensor patch.

In order to have a more successful test in the future, three main challenges have to be addressed:

- The mechanical coupling between the piezoelectric sensors and the airfoil skin provides strong natural frequency peaks of the airfoil, making it challenging to identify any other relevant signals underneath.
- The overall sensitivity of the piezoelectric sensors has to be improved in order to overcome the generally produced noise.
- The pyroelectric effect seems to play a major role, and has to be dealt with.

These three challenges might be solved by using a piezoelectric series bimorph. Such a bimorph cancels the pyroelectric effect, amplifies the mechanical input, and can be mounted mechanically isolated from the airfoil skin. This does however mean that the patch-concept, which ideally leaves a smooth airfoil skin, has to be discarded.



APPENDICES

4.A. PYROELECTRIC EFFECT

As briefly stated before, the low frequency signals obtained in this chapter are likely to occur due to the pyroelectric effect. The pyroelectric effect provides a constant output voltage to a constant change in temperature [9]. To determine if the low frequency signals obtained in this chapter could occur due to the pyroelectric effect, the pyroelectric response of the PZT-5A4 disks was experimentally obtained. One of the PZT-5A4 disks was placed on a Peltier element heating the sample from one side. At the same time, the output voltage was measured. Fig. A1 shows the pyroelectric response of a PZT-5A4 ceramic disk under a $1\text{ }^{\circ}\text{C s}^{-1}$ temperature ramp. A short time of about 1 s is required for the output voltage to reach its maximum value of about 220 mV. This time is required for the ceramic disk to experience the same temperature gradient throughout its whole volume. The same time delay occurs when the temperature ramp is removed. This likely occurs since it is only heated on one side of the sample. This figure shows the clearly present pyroelectric response of the ceramic disks, which is commonly known for PZT-5A4.

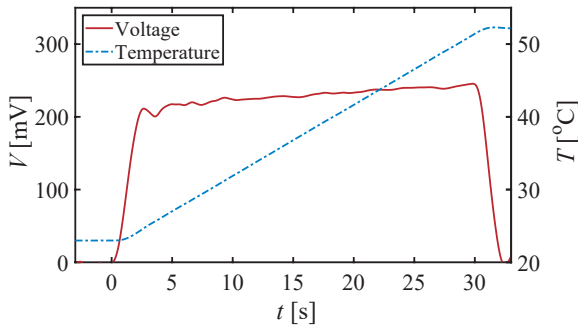


Figure A1: Pyroelectric measurements on a PZT-5A4 ceramic disk, providing the output voltage, V , as a function of time, t , while a $1\text{ }^{\circ}\text{C s}^{-1}$ temperature ramp is applied.

A change in temperature can occur on an airfoil because of the difference in heat transfer capacity of a laminar and a turbulent boundary layer [40]. When the bulk temperature of an airfoil differs from the temperature of the free stream, the temperature at the skin of the airfoil will be different in the laminar and turbulent region. In the laminar region the temperature tends to be closer to that of the bulk of the airfoil, while in the turbulent region the temperature is closer to that of the free stream. While the angle of attack is kept constant, the temperature of the airfoil and free stream only changes over long time

scales, in the range of minutes. This temperature gradient is too small to be measured by the pyroelectric effect. However, when one of the sensors moves from a laminar to a turbulent region, or vice versa, an abrupt change in temperature is experienced, which potentially can be detected by the pyroelectric sensor. Although we were unable to prove this line of reasoning, this could explain why the low frequency signal is observed while the angle of attack changes, while it is not while the angle of attack is fixed.

Another thing that was noticed in the data, is the change of signal sign which arbitrarily occurred. In some cases while having a positive angular velocity and low Reynolds number the low frequency signal had a positive sign, while with the same angular velocity at a higher Reynolds number a negative sign occurred. A possible explanation for this could be the faster rotating wind tunnel engine, creating more heat in the process, and therefore heating the airfoil instead of cooling it at lower speed settings.

Due to these reasons, it seems quite likely that the observed low frequency signals indeed originate from the pyroelectric effect rather than the piezoelectric effect.

4.B. PYROELECTRIC PATCH

Using the low frequency signals generated by the pyroelectric patch, the location of transition can be determined. We defined the onset of the low frequency waves as the location of transition. This is compared to the locations found earlier using the stethoscope, as was shown in Fig. 4.3. This comparison is shown in Fig. A2, showing the location of transition, x/c_{tr} , versus the angle of attack, α .

Fig. A2a presents the measurements at Reynolds numbers of 132×10^3 and 265×10^3 . The stethoscope measurements are performed while the angle of attack is kept constant. The pyroelectric measurements are performed while the angle of attack increased at a rate of 2°s^{-1} . The trends and values of both measurements nearly overlap. We see for both the stethoscope and pyroelectric measurements that the transition moves towards the TE with increasing the Reynolds number.

Fig. A2b presents the measurements using various angular velocities, da/dt . A very clear pattern is observed. The pyroelectric measurement curves perfectly arrange themselves from the lowest angular velocity of -5°s^{-1} , to the highest of 5°s^{-1} . We also see that the stethoscope measurement, which is performed at an angular velocity of 0°s^{-1} , lies near the -1°s^{-1} and 1°s^{-1} , with a small offset (below 1°) towards positive angular rotations. The reason why the angular velocity plays a role is due to the flow hysteresis effect. While the airfoil is at a certain angle of attack, a short amount of time is required for the boundary layer to reach equilibrium, resulting at transition at a certain point on the airfoil. If during that time the airfoil angle of attack increases, the transition point will lag behind. This means that by increasing the rate at which the angle of attack increases, the transition point will lag behind increasingly more. This is why the location of transition of the pyroelectric curve of 5°s^{-1} lies at higher angles of attack compared

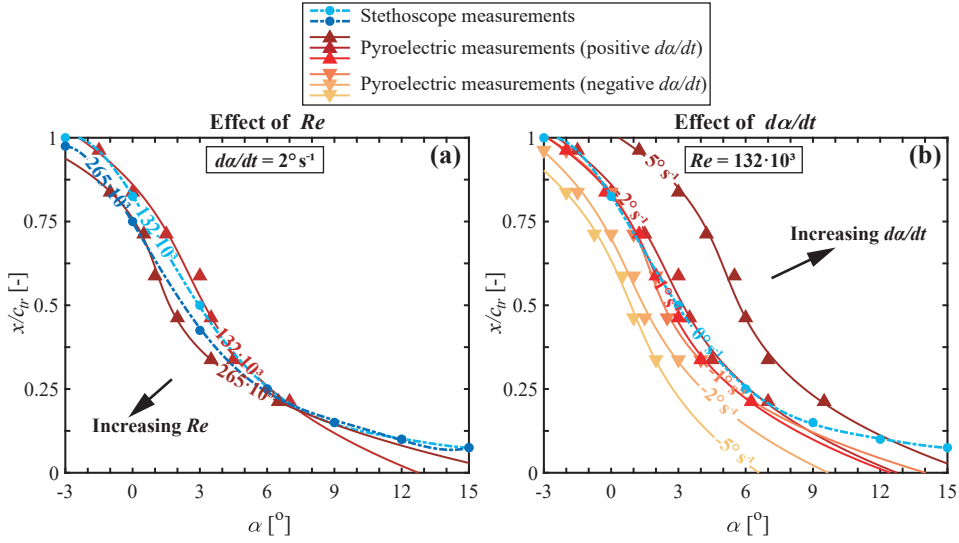


Figure A2: Location of transition, x/c_{tr} , versus the angle of attack, α , measured using a stethoscope and measured using the pyroelectric patch, as a function of (a) Reynolds number, Re , and (b) angular velocity, $d\alpha/dt$.

to the other curves. When the angle of attack is decreasing, the opposite occurs.

The graphs above show that a pyroelectric patch could work in principle, but only if the temperature of the free stream or airfoil constantly fluctuates. While both experience a constant temperature, the patch will not be able to detect transition.



5

BOUNDARY LAYER STATE DETECTION USING A PIEZOELECTRIC SENSOR

Two piezoelectric series bimorph sensors were embedded below the skin of a NACA 0012 symmetrical airfoil to detect the local state of the boundary layer during wind tunnel testing. Small vanes piercing the airfoil skin were glued onto the bimorphs providing a mechanical coupling to the local mechanical force fluctuations imparted by the local unsteady boundary layer flow. The state of the boundary layer at the sensor sites was varied by changing the angle of attack. The objective of this work was to establish the ability of this sensor concept to accurately distinguish among typical boundary layer states such as attached laminar flow, turbulent flow and separated flow. The output of the sensor was compared to concurrent time-resolved particle image velocimetry measurements, which served as a validation technique. Using the developed sensor response envelope, a single data point time series of the piezo electrical signal was proven to be sufficient to accurately detect the boundary layer state on classical airfoils in the low Reynolds number regime. In projected future applications, single or arrays of bimorph sensors can be used to map the boundary layer of more complex or morphing shape airfoils. The fast response of the sensor can in principle be utilized in closed-loop flow control systems, aimed at drag reduction or lift enhancement.

5.1. INTRODUCTION

The boundary layer plays an important role in the lift-to-drag ratio of airfoils, through the coupling of viscous and inviscid mechanisms. Typically, boundary layers can be classified as either laminar, which can be described as organized flow containing non-intersecting smoothly developing and predictable paths, or turbulent, which can be described as an almost random chaotic flow. The region in between the two states, where laminar flow changes into turbulent flow, is governed by the so-called laminar-to-turbulent transition process, typically (but not exclusively) governed by the emergence and growth of shear layer instabilities. Laminar or turbulent, boundary layers can experience so-called detachment or separation. Then they are unable to follow the shape of the aerodynamic surface, creating large recirculating areas.

A major difference between laminar, turbulent and separated flow is the drag generated which increases continuously when going from laminar to turbulent to fully separated [40, 105, 106]. In most aerodynamic applications, a high lift-to-drag ratio is desirable, as it leads to a higher aerodynamic efficiency. One way of increasing the lift-to-drag ratio of airfoils is to postpone transition and separation and to bring their locations as far downstream on the wing as possible. This can be achieved by passive means such as airfoil shape optimization [107] or by active means such as applying a feedback loop to an overactuated morphing aircraft wing, or by operating micro-actuator devices such as jet or plasma actuators [108–111].

In case of active flow control techniques, proper performance of such a feedback loop requires a measurement device that is able to locally detect the state of the boundary layer in real-time. The intrinsic differences between the boundary layer states include the shear stress at the skin of the airfoil, the heat transfer between the air and the skin, and the increased high frequency pressure fluctuations [40]. Given these differences, various measurement techniques to be used in wind tunnel testing have been developed to determine the local state of the flow around the airfoil, such as pressure or sound transducers [49, 50, 99], hot film sensors [51–53, 100], IR thermography [44–46], and shear stress measurements [54, 55, 101, 102]. However, a principal drawback of pressure measurements is the complication when multiple aerodynamic phenomena, such as transition and separation, coincide, as they provide similar pressure signatures. Drawbacks of heat flow measurements are the long minimal measurement time required and the need for active heating, as well as the necessity of having to use off-surface detectors such as IR cameras. Meanwhile, the challenge with shear stress measurements are the extremely low magnitude of the stresses to be measured as well as the reliance on delicate and damage-prone hot-film sensors [101, 102].

A promising and robust alternative to the aforementioned sensor technologies is the use of piezoelectric materials. These can be used to measure the effects described in the previous paragraph, as these materials directly generate an electric signal as response to a dynamic mechanical stress [9]. Although their generated output voltage is generally rather low, specific mechanical boundary conditions can be applied to mechanically amplify the input force signal and hence, obtain significantly enhanced output voltages.

An example of such passive amplification also utilised in the present work, is the use of a so-called bimorph, which in essence is a piezoelectric element clamped on one end, while the mechanical force is applied to the other end. Using this method, the output voltage and signal-to-noise ratio can be increased by an order of magnitude [37].

Earlier work has demonstrated the use of piezoelectric bimorphs for measuring low shear stresses [54]. In that set-up two piezoelectric bimorphs were mounted in parallel, with their tip connected to a rigid plate of a few square centimeters area. By applying a force parallel to the plate, pressure fluctuation values as low as one Pascal were measured, which is well within range of shear stresses typically found in boundary layers. Other research in this field involved the use of a piezoelectric composite bimorph of about 72 mm by 26 mm surface area, flush mounted on a flat plate acting both as a sensor and actuator [112]. While in sensor mode, the bimorph produced similar results to microphone sensors mounted on the same flat plate when tested in a wind tunnel.

While the first efforts in using piezoelectric bimorphs as flow sensors have shown promising results, such bimorphs would be used more optimally in case they were capable of detecting the large variety of boundary layer states. To date, no systematic effort has been spent on establishing these capabilities, neither for nominal (e.g. flat plate) nor more realistic aerodynamic geometries (e.g. airfoils). Considering an airfoil, the entire range of boundary layer states such as laminar, turbulent, separating or attached can appear depending on the Reynolds number, angle of attack and shape of the airfoil. An effective sensor needs not only to locally detect flow fluctuations present in each of these states, but must be also coupled to an informed interpretation algorithm able to distinguish pertinent flow features.

In the present work we set the first step towards the generalization of these piezoelectric bimorph sensors by conducting the first systematic study of their response to several boundary layer states developing on a typical airfoil. The aim of the work is not to develop a holistic sensing strategy (i.e. sensors, sensor placement, algorithms and implementations), rather to reconcile the output signal from an installed sensor to the incoming boundary layer. This forms the first step in characterizing the envelop of this sensor and provides physical insights into the interpretation of the signals.

Two piezoelectric series bimorph sensors, including amplifiers, are installed within a NACA 0012 symmetrical airfoil commonly used in laminar and flow control studies [47, 113]. The piezoelectric sensors are located under the skin of the airfoil, and are attached to a vane piercing the skin to detect flow fluctuations or perturbations in the boundary layer. One sensor is located near the leading edge (LE), while the other sensor is closer to the trailing edge (TE). The local boundary state at each sensor was varied by systematically varying the angle of attack. Concurrent time-resolved Particle Image Velocimetry (PIV) measurements performed on the same setup are used as validation technique. We show that a single data point obtained from the piezoelectric sensor is sufficient to define the state of the boundary layer.

5.2. METHOD

This section discusses details about the piezoelectric sensor design (5.2.1), the experimental setup (5.2.2) and gives an overview of the test cases (5.2.3).

5.2.1. PIEZOELECTRIC SENSORS

The piezoelectric bimorphs were prepared in-house. First, commercially produced piezoelectric PZT-5A4 plates with a size of 74 x 45 x 0.25 mm and silver electrodes on both sides were poled at 150 °C under a 2 kVmm^{-1} DC electric field for 5 min. After poling, two PZT-5A4 plates were bonded to either side of a Pernifer 45 substrate using epoxy (Epotek epoxy 302-3M, Epoxy Technology Inc.) containing 5 wt% Ni-balls with a diameter of about 10 μm . The Ni-balls make the bond conductive, electrically connecting one of each of the PZT-5A4 electrodes to the conductive Pernifer 45 substrate. Both PZT-5A4 plates were bonded in such a way that the poling directions were opposing each other, meaning that both poling directions were either pointing towards, or away from, the Pernifer 45 substrate. This is critically important for a series bimorph to work, because this cancels the pyroelectric effect and adds, instead of subtracts, the voltages generated by the piezoelectric effect [9]. After bonding, the two free electrodes on the PZT-5A4 were covered in carbon paste, acting as a protective electrically conductive coating. Finally, the sandwich structure was sawed using a diamond blade to the desired size of 3 by 10 mm. The layup described in this paragraph is visualized in Fig. 5.1. The capacitance and dielectric loss were measured at 1 kHz and 1 V with an Agilent 4263B LCR meter (Santa Clara, CA, USA), and were found to be 900 pF and 0.02, respectively. While in this chapter we use a PZT bimorph, Appendix 5.A briefly describes the manufacturing and performance of a composite bimorph which is specifically designed for the application of this chapter.

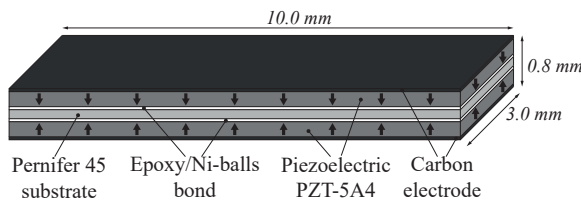


Figure 5.1: Layup and dimensions of the piezoelectric bimorph. The arrows in the PZT-5A4 plates indicate the poling direction which have to be pointed in opposite direction of each other.

Using a 3D printer (Ultimaker 3, Ultimaker B.V., Utrecht, The Netherlands), a polylactic acid (PLA) enclosure was 3D printed to house the piezoelectric bimorph. About 2 mm of the piezoelectric bimorph length was clamped in one of the walls of the enclosure, leaving a free length of 8 mm. On the free end of the piezoelectric bimorph, a 3D printed PLA vane was glued using cyanoacrylate adhesive. This vane was installed such to protrude through an opportune opening in the skin of the airfoil to mechanically couple the external flow to the piezoelectric bimorph. The vane reached a height of about 1.7 mm above the airfoil skin, and had a width of 6.0 mm. A schematic representation

of the piezoelectric bimorph including the vane inside the enclosure is given in Fig. 5.2. Using a shaker, the natural frequency under these boundary conditions in the direction of the flow was measured to be about 3 kHz.

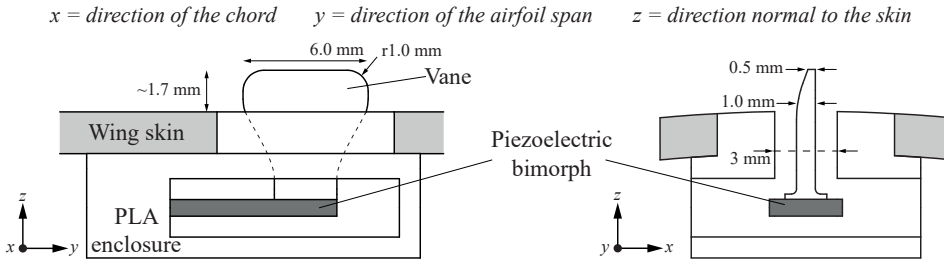


Figure 5.2: Schematic representation of the piezoelectric bimorph inside a PLA enclosure mounted underneath the airfoil skin. The vane is piercing the skin to transfer the oscillations originating from the boundary layer to the piezoelectric bimorph.

An ultra-low input current CMOS amplifier was directly connected to both carbon electrodes of the piezoelectric bimorph, providing a resistive load of 100 M Ω . The amplifier copies the voltage obtained from the piezoelectric bimorph, amplifies it, and drives a data acquisition unit without signal loss due to wiring and circuit load. To minimize environmental noise, the wires between the piezoelectric bimorph and amplifier were kept as short as possible. The amplifiers send the analogue signal to a data acquisition unit, which converts it to a digital signal, at a sampling frequency of 40 kHz per sensor channel. The used data acquisition hardware has a built in anti-aliasing filter which requires one to measure about 10 times higher than the highest desired frequency to measure. We were therefore able to measure accurately up to 4 kHz.

A NACA 0012 airfoil with a chord length of 200 mm and a span of 400 mm was used for the characterization of two separate sensors. One sensor was positioned near the LE of the airfoil, while the other was positioned near the TE, as shown in Fig. 5.3. To prevent the turbulent wedge created by the LE sensor to influence the measurements taken by the TE sensor, the two sensors were positioned 45 mm on either side of the mid-span of the airfoil.

It must be noted that, although the manufacturing was performed as accurately as possible, the actual dimensions of the piezoelectric bimorph and PLA enclosure can vary from sensor to sensor. This in turn can have an influence on the resonance frequency and sensor sensitivity. However, the primary objective of the sensor is to infer the state of the local boundary layer in its vicinity. As will be shown in subsequent sections, this can be performed in a relativistic manner, meaning that the exact values of the resonance frequency and sensor sensitivity are not crucial. The amplitude will be extracted from a range of frequencies, and hence, as long as the resonance frequency stays within the respective range, the exact value is not important. In addition, we do not require an exact amplitude measurement, as we only compare relative values. As such, a detailed

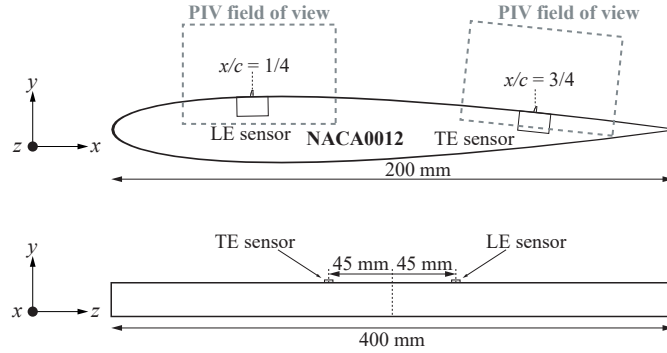


Figure 5.3: Schematic representation of the locations of the piezoelectric sensor located near the LE and the TE of the airfoil. The top image shows the side view with the chordwise locations, including a representation of the respective PIV fields of view, while the bottom image shows the view from the LE with the spanwise locations.

5

uncertainty evaluation of the sensor is not deemed necessary for boundary layer state estimation.

5.2.2. EXPERIMENTAL SETUP

The wind tunnel experiments were performed in the A-Tunnel, at the Low Speed Laboratory of the Delft University of Technology. The A-Tunnel is a low turbulence tunnel with a turbulence intensity of below 0.1% and interchangeable exit nozzles [114]. For the present study, an open-jet exit nozzle with a cross section of 600 mm by 400 mm was used, allowing a maximum free stream velocity of about 35 m s^{-1} . The NACA 0012 airfoil was positioned in the midplane, approximately 200 mm from the exit nozzle. To ensure spanwise invariant conditions, flat side plates of 600 mm width and 1000 mm length were used. During the experiments this free stream velocity was monitored using a pitot-static tube located upstream of the airfoil. For the experiments reported here, the tunnel was operated at 12.5 m s^{-1} , corresponding to a chord Reynolds number of 165×10^3 . The Reynolds number was calculated using a kinematic viscosity, ν , of $1.5111 \times 10^{-5} \text{ m}^2 \text{ s}^{-1}$, and a characteristic length, L , of 200 mm, equal to the chord length of the airfoil. The airfoil angle of attack was digitally controlled and set using an automatic rotation table with a positional resolution of 0.1° . Furthermore, the boundary layer on the pressure side of the airfoil was tripped to turbulence using a zigzag tape. This eliminates any possible influence of pressure side separation on the suction side developing flow.

Time-resolved two-component planar PIV measurements were performed for the characterization of the boundary layer in the vicinity of the sensor. A Photron SA1.1 with a 1024×1024 pixel CMOS sensor was equipped with a 105 mm macro objective, set at aperture number of 5.6. A Quantronix Darwin Duo Nd: YLF high speed laser (30 mJ per pulse) was used in conjunction with a set of spherical and cylindrical objectives to form a laser light sheet of approximately 1 mm thickness. The laser sheet was aligned to the

x - y plane and was positioned such as to intersect the mid of the piezoelectric sensor vane. Pairs of images were captured at 6 kHz sampling rate, over a total measurement time of about 1 second. Inter-pair time separation was set to 60 μ s, resulting in average particle displacement of approximately 14 pixels in the freestream. The flow was seeded with theatrical smoke produced using an atomized water-glycol mixture, resulting in tracer particles of about 1 μ m diameter. Synchronization of camera and laser as well as image acquisition was performed using LaVision Davis software.

The flow developing in the vicinity of the LE and TE sensor was imaged independently. A field of view of approximately 90 x 45 mm was imaged, with a magnification factor of approximately 0.08. Particle image pairs were processed using multi-pass correlation algorithms in Lavisision Davis 10 software. A final interrogation window of 16 x 16 pixels and 75 % overlap was used, producing a final vector spacing of 88 μ m. The random error in the instantaneous velocity fields is estimated to be less than 1 % [115].

Using the PIV data, two boundary layer thicknesses were calculated being the displacement thickness, δ^* , and the momentum thickness, θ [40, 105]. These thicknesses can be calculated using:

$$\delta^*(x) = \int_0^{y_{max}} \left(1 - \frac{u(x, y)}{U_e(x)} \right) dy \quad (5.1)$$

$$\theta(x) = \int_0^{y_{max}} \frac{u(x, y)}{U_e(x)} \left(1 - \frac{u(x, y)}{U_e(x)} \right) dy \quad (5.2)$$

In here, y_{max} is the value of y where 99 % of the local boundary layer edge velocity is reached ($0.99 \cdot U_e(x) = u(x, y = y_{max})$), and $u(x, y)$ is the boundary layer velocity in the x -direction.

5.2.3. TEST CASES

Prior to the PIV measurements, the output of both piezoelectric sensors was measured over a time period of 10 s in static conditions (i.e. at a constant freestream velocity and angle of attack). These measurements were taken at angles of attack from 0° to 18°, with a step size of 0.5°. The measured data was analyzed in Fourier space using Welch's method, splitting the data into 20 segments with a 50 % overlap [116]. The Power Spectral Density (PSD) of the signal is calculated at discrete frequencies with a resolution of 20000 data points. The PSD is further scaled by the equivalent noise bandwidth of each window in order to arrive at an estimate of spectral power at each frequency (given in dB).

The PIV measurements were performed on one of the two piezoelectric sensors at a time to achieve higher spatial resolution. Concurrent with each PIV measurement, the output of the piezoelectric sensor was also measured. The angles of attack for which PIV acquisitions were made were chosen based on the piezoelectric data obtained earlier, such to reveal pertinent features underlying the developing flow. Additional angles with a small step size were taken in regimes of strong variations of phenomena. The imposed

angles of attack for both sensors are listed in Table 5.1.

Table 5.1: Imposed angles of attack for the concurrent PIV and piezoelectric sensor measurements.

	LE Sensor	TE Sensor
Angle of attack, α , [°]	1.0	1.0
	4.0	2.0
	6.0	3.0
	6.5	4.0
	7.0	5.0
	7.5	6.0
	8.0	13.0
	8.5	16.0
	9.0	
	13.0	
	16.0	

5.3. RESULTS

This section discusses the data obtained from the piezoelectric sensors (5.3.1) and the data obtained from the PIV measurements (5.3.2).

5.3.1. PIEZOELECTRIC DATA

Fig. 5.4 shows the spectral analysis of the piezoelectric sensor measurements which were measured prior to the PIV synchronized measurements. The power spectral density of the data is shown versus the frequency, f , for 37 angles of attack, α . As earlier mentioned, the raw voltage data obtained from the piezoelectric sensors are analysed using Welch's method to obtain the frequency domain results, divided into results obtained using the LE sensor and the TE sensor. The row of peaks just below 3 kHz occurs due to the resonance frequency of sensor.

Fig. 5.4b and d show the same data as in Fig. 5.4a and c but now in the form of contour plots to easily distinguish among the different regimes found. Fig. 5.4b shows the measurement of the LE sensor, and shows 3 major regimes of angles of attack respectively named 'regime a' through 'regime c'. For the LE sensor, regime a extends to an α of about 8°, where relatively little activity is present. In regime b, which occurs between about 8° and 14°, the amplitude over the entire range of frequencies increases, with additional sharp peaks just below 3 kHz. Finally in regime c, above 14°, only a broad range of low frequency activity is observed below 100 Hz, while minimal activity is observed above this frequency. Fig. 5.4d, providing the measurements of the TE sensor, reveals a similar regime distribution. The main difference is the border between regime a and b, which in this case lies around 4°.

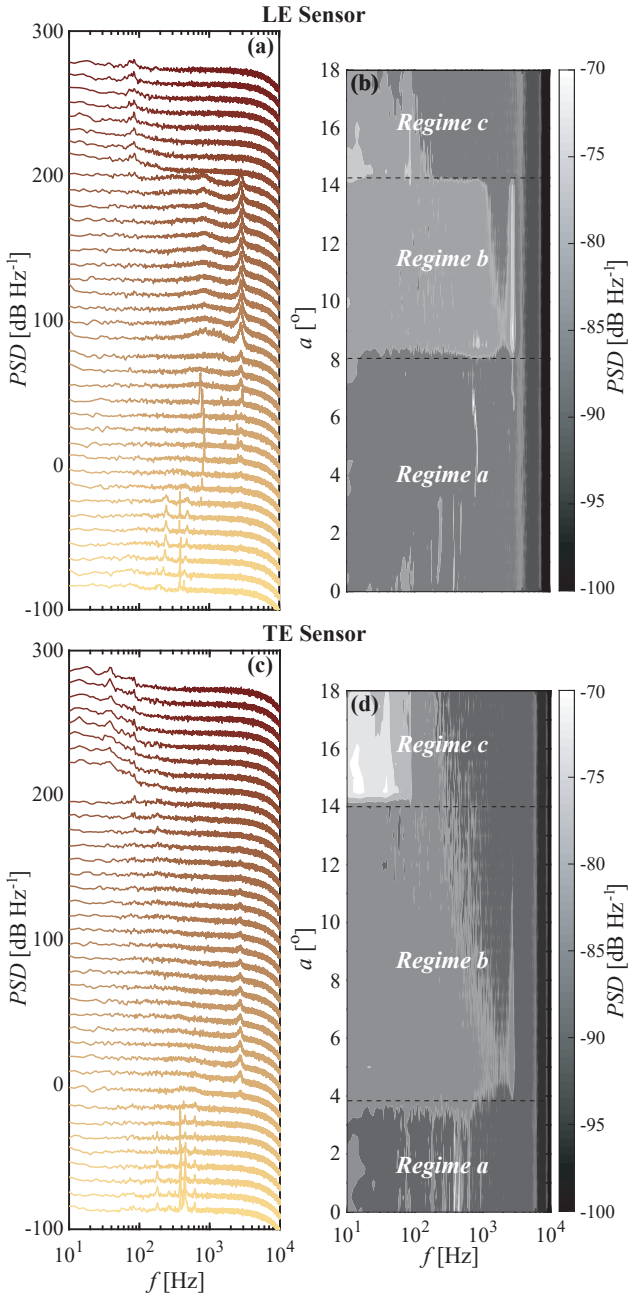


Figure 5.4: Power spectral density, PSD , versus frequency, f , as a function of angle of attack, α . LE sensor data plotted as (a) separated lines and (b) contour plot. TE sensor data plotted as (c) separated lines and (d) contour plot. For clarity, the lines in (a) and (c) are shifted by 10 dB Hz^{-1} per 0.5° angle of attack increase.

In summary, Fig. 5.4 confirms the ability of the piezoelectric bimorph sensor to detect a wide range of events, occurring in distinctly different frequency bands. The dependence of these frequencies on the angle of attack suggests that indeed the sensor is activated by coherent fluctuations in the local flow. In the following sections we will use the time-resolved PIV measurements to identify these fluctuations as well as to infer the local boundary layer state.

5.3.2. STATISTICAL VELOCITY FIELDS

Fig. 5.5 shows an overview of the velocity fields obtained through the PIV measurements also showing the airfoil surface contour and the outline of the sensor. Velocity vectors are time averaged over the full measurement period. The contours of the data points having a negative velocity in the x direction, or negative u , are marked by the blue contour line to highlight reversed flow. The gray scale background presents the normalized standard deviation of velocity fluctuations of u (white background corresponds to standard deviation as for undisturbed flow, dark background corresponds to high standard deviations as for disturbed flow).

5

Fig. 5.5a, which shows the velocity field near the LE sensor, indicates a large wake behind the sensor vane up until 7° , which is considerably reduced at 13° angle of attack. This happens because transition at or near the site of the sensor vane occurs at an angle of attack around 8° . Hence, a developed turbulent flow exists above this angle, which suppresses separation, enhances mixing and results in a smaller wake. At 16° , massive flow separation (i.e. airfoil stall) occurs over the entire airfoil. Interestingly, the effect of the vane on the upstream flow field is rather small, indicating that the vane records the naturally occurring flow phenomena, rather than induces artificial flow phenomena related to the presence of the vane itself.

Taking a look at Fig. 5.5b, which shows the velocity field near the TE sensor, a region of reversed flow upstream to the vane is observed at 1° . This is a typical manifestation of a Laminar Separation Bubble (LSB) for this airfoil [47]. Furthermore, the LSB moves upstream towards the LE at an angle of attack of 4° . We also note the reduced wake behind the sensor at an angle of 4° compared to the 1° case, again indicating a turbulent flow. At higher angles this wake increases again, up until separation happens at an angle of 16° .

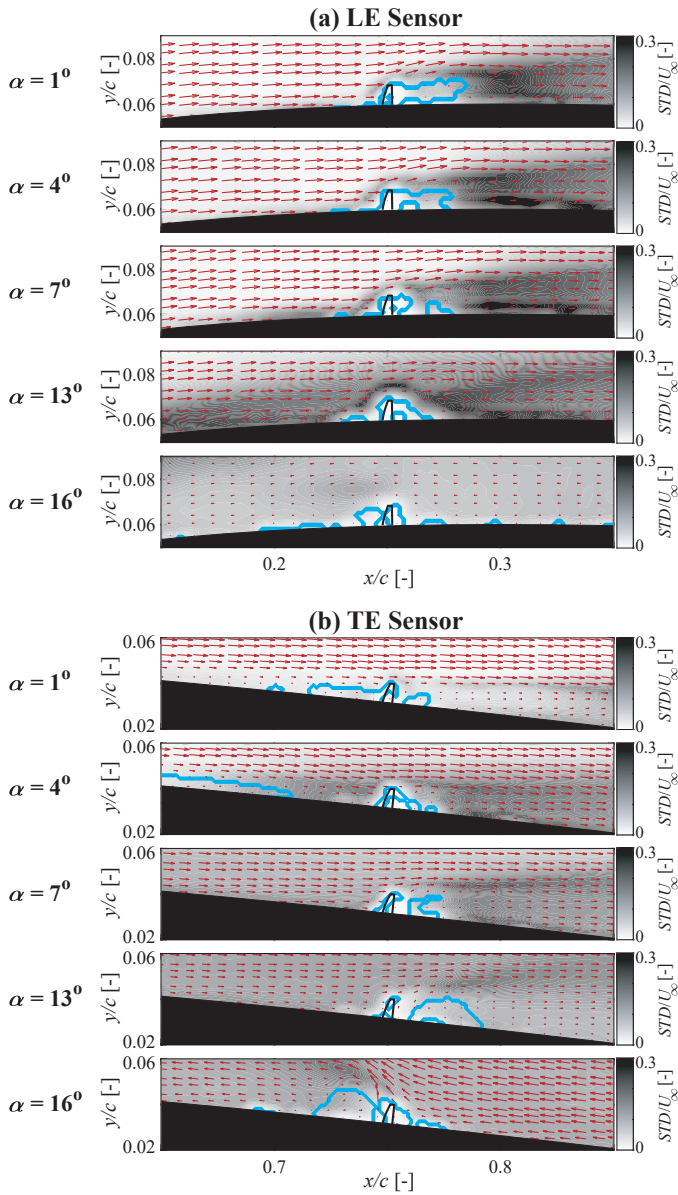


Figure 5.5: Processed PIV images with the piezoelectric sensor vane drawn in it, showing the time averaged velocity fields over the full measurement time, varying the angle of attack, α , of the sensor mounted near the (a) LE and (b) TE. The red arrows show the flowfield, the blue lines the contour of reversed flow, and the grayscale background the normalized standard deviation.

5.4. DISCUSSION

This section discusses the determination of the boundary layer state from the PIV measurements (5.4.1), how the piezoelectric sensor data relates to the PIV data (5.4.2) and finally provides an overview of how to read the data obtained from the piezoelectric sensors (5.4.3).

5.4.1. BOUNDARY LAYER STATE FROM PIV

The state of the boundary layer can be extracted from the statistical PIV measurements in various ways. First, we consider the values of the standard deviation, STD , occurring in the flow. As shown in the previous section, the boundary layer develops a characteristic topology of velocity fluctuations near the wall and in the vicinity of the piezoelectric vane. Generally, the value of STD in a turbulent flow is higher compared to a laminar flow, and peaks around transition, due to the appearance of large coherent structures prior to breakdown [50]. To facilitate proper comparison of cases at different angles of attack we choose an x -coordinate upstream of the sensor to probe the maximum STD , STD_{max} , in the boundary layer. We choose the probing location such that it lies sufficiently close to the sensor, yet is not directly affected by the sensor itself. By inspection of the fluctuation field topology for the majority of cases, the optimum probing location was found to be at $x/c = 0.23$ (LE sensor) and 0.73 (TE sensor), which corresponds to 4 mm upstream of the vane. At this x -coordinate, STD_{max} is found occurring through the entire y range per angle of attack for both u and v velocity components. The results are shown in Fig. 5.6.

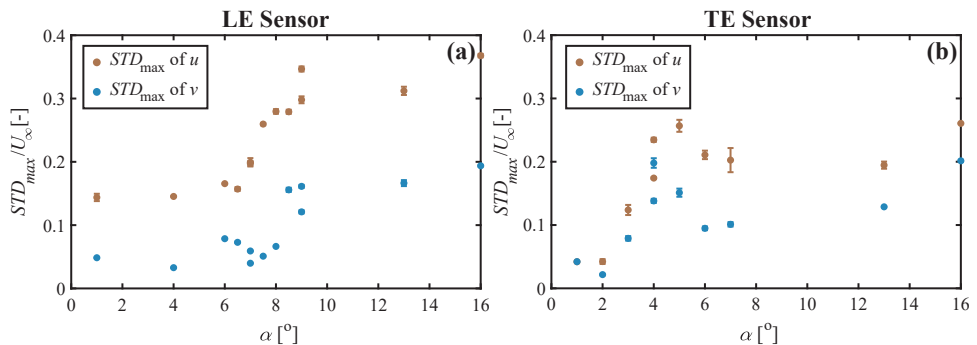


Figure 5.6: Maximum standard deviation, STD_{max} , for both the u and v vector versus the angle of attack, α , measured near the (a) LE sensor and (b) TE sensor. The values are extracted at an x -coordinate 4 mm upstream of the piezoelectric sensor.

In Fig. 5.6a the results near the LE sensor are shown. Both u and v fluctuations show a similar trend, having a relatively low value at low angles, peaking near 8.5° to 9° , and then continue to stay at a higher value compared to before the peak. Typically, the observed evolution of fluctuations confirms expectations on the development of transition, as the latter moves upstream with increasingly adverse pressure gradient (i.e. increasing angle of attack). Based on these observations, transition from laminar to turbulent flow

at the probe location is occurring at the site of the LE sensor in the range of angles of attack between 8.5° and 9° . Fig. 5.6b shows the results near the TE sensor, and reveals a corresponding fluctuation peak at 4° to 5° .

A second independent evaluation of a boundary layer state can be made based on the consideration of integral quantities, such as momentum and displacement thickness, and their respective ratio (i.e. the so-called shape factor). A boundary layer in turbulent state will possess less momentum compared to a respective laminar state due to increased wall shear. This will directly entail a larger momentum thickness. Similarly, due to less momentum, a turbulent boundary layer will also thicken, displacing the outer inviscid streamlines more than when laminar. This will correspond to an increase in displacement thickness. However, due to the increased mixing in a turbulent boundary layer, momentum is largely redistributed in the layer, causing the two thicknesses to increase differently. This results into a different shape factor, $H (= \delta^*/\theta)$, for laminar and turbulent boundary layers, with the latter begin typically lower ($H = 1.4$ for turbulent vs. $H = 2.6$ for laminar states in flat plate conditions). Considering the shape factor of a given boundary layer provides a robust estimate of its state, purely based on time averaged statistical velocity information.

For the present cases, the integral boundary layer thickness and resulting shape factors are estimated based on the PIV velocity measurements at an x -coordinate of 4 mm upstream of the sensor vane. The results are shown in Fig. 5.7.

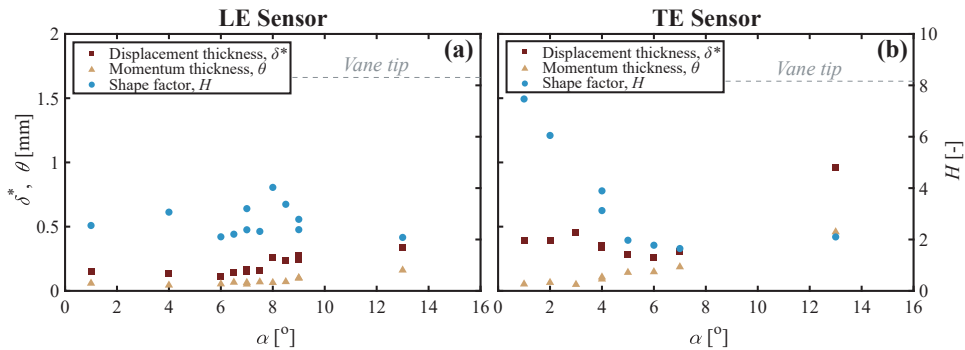


Figure 5.7: Boundary layer displacement thickness, δ^* , momentum thickness, θ , and shape factor, H , versus the angle of attack, α , measured near the (a) LE sensor and (b) TE sensor. The values are extracted at an x -coordinate 4 mm upstream of the piezoelectric sensor.

Fig. 5.7a gives the thicknesses found near the LE sensor, and shows thickening of the boundary layer near 8° to 9° , which is in good agreement with the increase of velocity fluctuations associated to transition. For the case of the TE sensor, the displacement thickness given in Fig. 5.7b shows an early peak around 3° , corresponding to the emergence of a laminar separation bubble (LSB), visible in Fig. 5.5. The appearance of a LSB is well documented for the current airfoil and Reynolds number [47], and increases the

complexity of the fluctuation flow as will be shown later. The momentum thickness further shows an increase around transition near an angle of 4° to 5° . Around 13° a major increase in thickness is observed, corresponding to the eminent global separation of the flow, as was earlier seen in Fig. 5.5. In addition, it becomes evident that in all cases the vane height is considerably larger than the incoming boundary layer thickness, with the exception of the massively separated flow at an angle of attack of 16° .

The results presented up to this point clearly indicated the ability of the used configuration to assume a wide range boundary layer states. Relatively wide ranges of angle of attack are defined in laminar or turbulent states, with a clear transition point while specific angles reveal the appearance of LSBs or fully separated flows.

5.4.2. DETECTION OF BOUNDARY LAYER FLUCTUATIONS

From the aforementioned observations it becomes clear that the piezoelectric bimorph sensor is exposed to a wide range of fluctuations in the identified angle of attack regimes. Similarly, the inspection of the PIV measurements allows proper identification of the boundary layer states as function of chordwise location and angle of attack.

Nevertheless, while the PIV measurements provide a spatio-temporal representation of the flowfield, the bimorph sensor essentially extracts a single time series of data, corresponding to the integrated mechanical force acting on the vane. In order to facilitate the comparison of the velocity fluctuations found in the PIV data to the unsteady output signal of the piezoelectric bimorph, a procedure is devised for the extraction of pertinent velocity information. The chosen method is not unique, however it was found to be effective in facilitating this comparison.

The extraction method is visualized in Fig. 5.8. First, we define xy -coordinates from which to extract u vector. The x -coordinate is fixed at 4 mm upstream of the sensor vane, as this was found to be a sufficient distance to avoid measurement interference originating from the upstream effects of the sensor vane on the boundary layer. An exception was made for the case of an angle of attack of 16° , with the x -coordinate chosen on the downstream side of the vane due to the flow direction reversal, as can be seen in Fig. 5.5. The y -coordinate was chosen to be 1, 2 and 4 mm above the airfoil surface. Although for the majority of the cases the boundary layer is thinner than these values, lower y -coordinate locations were avoided due to areas of high light reflections, which reduce the confidence in the PIV data. The chosen xy -coordinates are visualized in Fig. 5.8a.

The time series of the u vector component is extracted at each of the defined coordinates, as shown in Fig. 5.8b. We use Welch's method to obtain the frequency domain signals. Two frequency bands of interest are defined based on the preceding analysis of the piezoelectric data (Fig. 5.4). The lower band is defined between 50 and 100 Hz. While considerable activity in the piezoelectric signal was present at frequencies as low as 10 Hz, the choice of a higher cut-off was made due to an artefact in the measure-

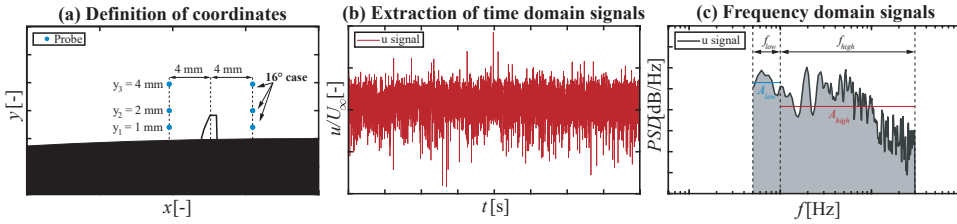


Figure 5.8: Schematic presentation of the method used to extract the oscillations occurring in the boundary layer from the PIV measurements. (a) The PIV sampling coordinates are upstream of the sensor vane (for $\alpha < 16^\circ$) and downstream of the vane (for $\alpha > 16^\circ$). (b) A typical time domain u signal for a particular probing coordinate (in this case the signal at a height of 2 mm measured at the LE sensor at an angle of attack of 9° , corresponding to a turbulent condition) the probe coordinates. (c) The frequency domain signal as obtained with the Welch's method with the power level calculated for the two frequency bands defined (see text).

ment routine. More specifically, the PIV laser was aligned to illuminate the mid-span of the vane, and as such it was found to intensively heat one side of the piezoelectric bimorph for a short time during acquisition. This caused a low frequency pyroelectric contribution to the overall sensor output, which was largely suppressed by the choice of the frequency range boundaries. The higher band is chosen to be from 100 to 3000 Hz, which as mentioned earlier is the resonance frequency of the sensor assembly. By not including the resonance frequency, similar results are obtained. The main difference between including and excluding the resonance frequency, is the signal-to-noise ratio of the piezoelectric sensor signal. We therefore chose to include it.

The frequency bands are shown in Fig. 5.8c. The total fluctuation amplitude within these frequency bands was calculated by integrating the frequency band within this range. The resulting amplitudes correspond to the statistical fluctuation strength within that particular frequency band occurring at the corresponding extraction location coordinate. Equivalent spectral analysis and frequency band definition was followed for the piezoelectric sensor data.

The outcomes of the spectral analysis method applied on both PIV and piezoelectric sensor data are visualized in Fig. 5.9 for the LE sensor. The low and high frequency bands are shown in Fig. 5.9a and b respectively.

An evident dependence of the PIV fluctuation amplitude on the y -coordinate of velocity extraction can be observed for both low and high frequencies. While all three extraction probes reveal similar trends, the lowest coordinate locations ($y = 1$ and 2 mm) reveal the closest agreement with the piezoelectric sensor output. This is largely expected as the majority of flow fluctuations are concentrated near the airfoil surface, as we saw earlier in Fig. 5.7, and because of the height of the sensor vane being in that range. In general, both PIV and piezoelectric data signatures reveal low power values at angles below 8° , with an increase at higher angles. An outlier is present for the angle of 16° where only low frequencies remain, while high frequencies are largely dissipated. This was largely expected as at this angle of attack the location of the sensor vane is deeply in stagnant

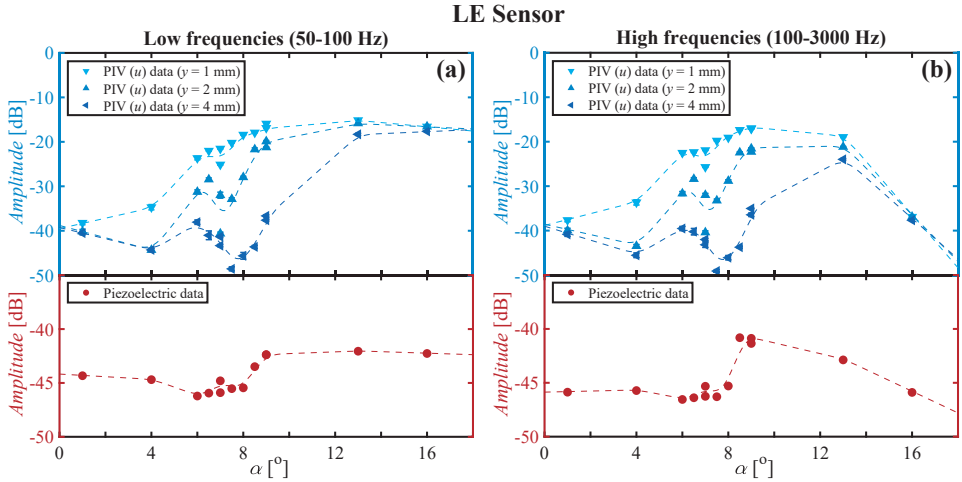


Figure 5.9: Power measured near the LE sensor of the piezoelectric and PIV data between (a) 50 and 100 Hz and (b) 100 and 3000 Hz. The PIV data is extracted from the coordinate about 4 mm upstream of the sensor vane and various y values above the airfoil skin. The general trends are shown by the dash lines, constructed by taking the moving average of the data.

5

low velocity reverse flow, where high frequencies due to turbulent flow are absent [42].

Furthermore, a non-monotonic amplitude behavior is observed in the high frequency band. More specifically, for the probe location of $y = 1$ mm, as well as for the piezoelectric sensor output, a local maximum is registered at angles of attack of 8° to 9° . This is attributed to two separate effects. Firstly, laminar-to-turbulent transition is occurring at these conditions in the vicinity of the sensor as shown in the previous section. For low Reynolds airfoils, transition is known to be forced by the appearance and amplification of coherent boundary layer instabilities such as Tollmien-Schlichting waves [111]. These reach maximum amplitude prior to turbulent breakdown. Furthermore, due to their spanwise coherency and narrow frequency band, the amplitude of these instabilities can well exceed turbulent fluctuations, thus producing local maximum evident in Fig. 5.9b. Secondly, the boundary layer thickness increases at transition, as was seen before in Fig. 5.7, effectively bringing the high fluctuation activity closer to the height of the piezoelectric vane as well as to the PIV probe locations.

In conclusion, the correspondence of piezoelectric sensor output to the PIV measurements is considerable, with strong similarities found in the evolution trend. The agreement further appears to be a function of the wall normal distance, as the sensor is evidently more sensitive to near-wall velocity fluctuations. The general sensing envelope of the LE sensor is characterized by low relative amplitudes in attached laminar flow (low angles of attack), high relative amplitudes in attached turbulent flow (high angles of attack), and considerable low frequency content at flow separation (angle of attack 16°). In addition, the sensor produces a characteristic maximum when the transition

location corresponds to the vane position which happens at an angle of attack of 8.5°.

Fig. 5.10 shows the corresponding comparison of the piezoelectric sensor output data and the data derived from the PIV measurements for the TE sensor. The strong dependence of velocity fluctuations to wall normal probe location is similar to the LE sensor case. Again the output of the piezo sensor captures the same information as in the PIV signals. Yet, qualitative differences can be observed with respect to the readings of the LE sensor. Compared to the LE sensor, the amplitude of the transition peak for the TE piezoelectric sensor is lower. This possible occurs due to the existence of the LSB near the TE sensor, as we saw earlier in Fig. 5.7, damping the effect of the transition peak. At an angle of 4° the downstream end of the LSB extends up until the sensor vane. The height of the vane enables it to still be able to pierce through the bubble thickness and 'sense' the external boundary layer flow. However, only the top portion of the vane is able to sense this, causing a lower overall mechanical input and hence a lower signal amplitude. Furthermore, another difference between the LE and TE case is the magnitude of the low frequency curves of both the piezoelectric output and PIV data. In the case of the TE sensor, stronger low frequencies occur near separation compared to the LE sensor. This simply occurs due to the stronger reversed flow observed near the TE sensor. This was already observed before at the 16° angle of attack cases in Fig. 5.5, where the flow velocity vectors at the TE sensor are clearly larger than those near the LE sensor

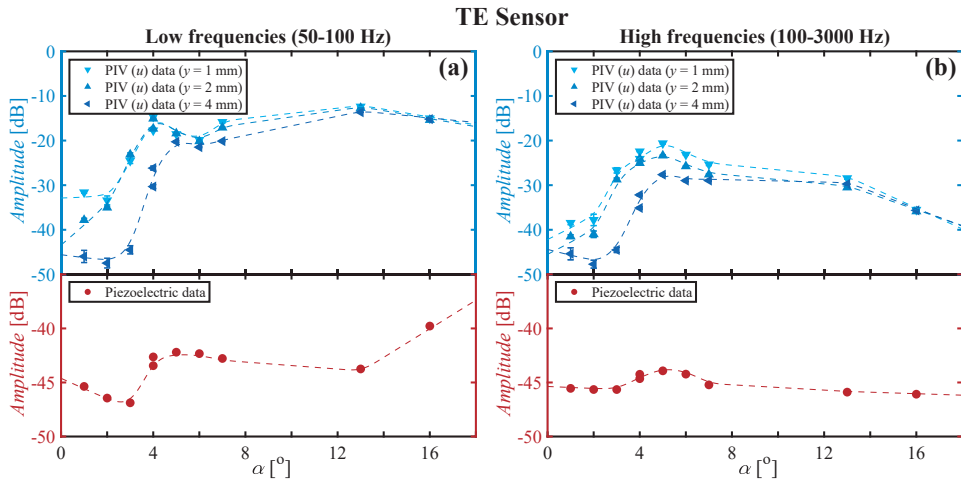


Figure 5.10: Power measured near the TE sensor of the piezoelectric and PIV data between (a) 50 and 100 Hz and (b) 100 and 3000 Hz. The PIV data is extracted from the coordinate about 4 mm upstream of the sensor vane and various y values above the airfoil skin. The general trends are shown by the dash lines, constructed by taking the moving average of the data.

In summary, the frequency intensities measured by the piezoelectric sensor correspond well to the fluctuations found in the boundary layer using PIV. In turn, these fluctuations can directly be related to the state of the boundary layer, indicating that the properly

processed piezo sensor signal indeed can capture the state of the boundary layer.

5.4.3. HOW TO READ THE PIEZOELECTRIC SENSOR

The previous section has identified a clear relation between the boundary layer state and the piezoelectric sensor output. As mentioned in the introduction, the motivation for characterizing this type of sensor in a wide range of flow conditions further serves in construction of a 'response envelope', which can be used for real-time and stand-alone interpretation of the sensor output as reference to the local boundary layer state. It has to be noted that the sensing ability of the sensor is strictly local and only refers to the boundary layer state at the location of the sensor. Based on the aforementioned analysis, this response envelope can be summarized as follows:

- *Laminar attached boundary layer*: the sensor output is mainly characterized by relatively low amplitudes at all frequencies.
- *Transition or eminent turbulent breakdown*: the sensor output indicates a rapid amplitude increase in both low and high frequencies. Transition can be driven by classical boundary layer instabilities (i.e. Tollmien-Schlichting waves) or through the formation of a LSB.
- *Attached turbulent flow*: the sensor registers considerable amplitude increase in both low and high frequencies. In addition the resonance frequency of the sensor (3 kHz for the present configuration) is strongly excited.
- *Massively separated flow*: the sensor registers increased fluctuation amplitude at low frequencies, but reduced amplitudes at high frequencies.

This response envelope is also summarized graphically in Fig. 5.11. It must be stressed that the general applicability of the envelope can be proposed for a relatively broad range of classical airfoil flows at low Reynolds numbers, as the NACA 0012 configuration in this work is fairly characteristic of these regimes. Nevertheless, for significantly different regimes such as encountered in swept wings, multi-element airfoils, high Reynolds or Mach numbers, careful calibration of the sensor response envelope against independent boundary layer state measurements should be performed. Furthermore, if the sensors are to be used outside the wind tunnel conditions, additional effects of changing temperature, humidity, pollution levels etc. need to be taken into account as well.

Finally, the importance of the height of the sensor vane must be noted. If the vane is too small the mechanical input from the flow might be too low and the reach of the vane might not extend to important fluctuation events near the top of the boundary layer. On the other hand, if the vane is too large, it might not be sensitive enough to events near the root of the vane and the influence of the vane on the surrounding boundary layer might be excessive (i.e. increases fluctuations and/or forces transition). In the cases measured in this work the upstream and downstream effects of the sensor vane appeared to be minimal. In future, the optimal size of the sensor vane in relation to both measurement

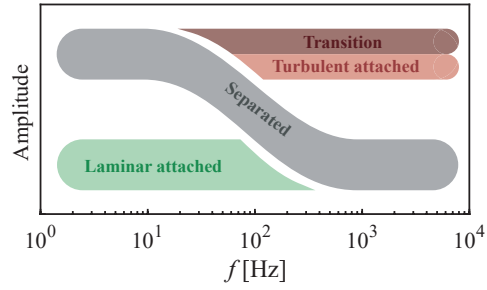


Figure 5.11: Response envelope of the piezoelectric sensor. The narrow mechanical resonance frequency of the sensor is left out as it is not indicative of the aerodynamic state.

sensitivity and downstream effect should receive dedicated investigation for the corresponding conditions of full-scale applications.

5.5. CONCLUSIONS

This chapter presents a piezoelectric bimorph sensor embedded in a NACA 0012 airfoil to measure fluctuations in the boundary layer. The objective was to prove that such a sensor can be used to distinguish among various boundary layer states.

Using PIV measurements as validation technique, we were able to show a clear relation between the piezoelectric sensor data and the boundary layer state. Dividing the signals into two frequency bands, the same signal signatures were found using the piezoelectric sensor and PIV measurements. Using the developed sensor response envelope, a single data point time series appears sufficient to specify the boundary layer state on classical airfoils in low Reynolds number regimes.

In the future, such a sensor might be used to map the boundary layer surrounding a more complex airfoil. It could also be used as an input component in a closed-loop control system to delay transition, and therewith reduce skin friction, possibly optimizing the overall lift-to-drag ratio of an airfoil.

APPENDICES

5.A. COMPOSITE BIMORPH

Due to the toxicity of the substance lead, which is used in the production of the piezoelectric material PZT, ways to replace PZT with other piezoelectric materials is widely investigated. This appendix briefly discusses the possibility to replace the PZT used for the application described in this chapter with piezoelectric composite material. First we manufactured a composite bimorph with identical dimensions to the PZT bimorphs used in this work. Next, identical mechanical boundary conditions are applied to both materials while the output voltages are measured and compared.

The composite material is composed of a high filler fraction piezoelectric KNLN particles randomly orientated in an epoxy matrix (Epotek epoxy 302-3M, Epoxy Technology Inc.). We choose to use KNLN as ceramic filler because of its low dielectric constant, ϵ_f , and high Curie temperature, T_c . The low dielectric constant of the filler increases the piezoelectric charge constant, d_{33} , of the composite, as was shown in Chapter 2. The high Curie temperature makes it possible to repeatedly perform curing steps at temperatures of about 100 °C without losing the polarization of the piezoelectric material. This was required to be able to bond the individual bimorph layers together and to bond protective electrodes to the outer surfaces of the bimorph after the individual bimorph layers were poled. The motivation to use epoxy as matrix material is because of its high stiffness, easy of adhesion to other materials, and low required poling field as was also shown in Chapter 2. Finally, we choose to go for a high filler fraction random composite to obtain a material with a (for composites) relatively high dielectric constant. This is done for two reasons. The first reason is that a higher dielectric constant significantly reduces the suffered voltage losses which occur in the wires between the piezoelectric element and the amplifier. This effect can, and is, also reduced by choosing short wires, which in this case was chosen to be in the range of a couple of centimeters. The second reason is due to a resistive load added to the amplifier. This resistor limits the DC offset to prevent the amplifier from overloading. This DC offset can occur due to the pyroelectric contribution, which in the case of a bimorph is significantly reduced but still not zero when the bimorph is heated asymmetrically. This resistive load has a side effect of reducing the gain at low frequencies. This effect is even more pronounced when using a piezoelectric element with a low capacitance. Therefore, a composite with a higher dielectric constant is preferred. An alternative approach is to change the value of the resistive load. This is also briefly investigated here.

Composite layers were manufactured by embedding 55 vol% of KNLN particles with a particle size ranging from 1 to 100 μm in the epoxy matrix. After poling the cured composite, we obtained a 99 % density composite with a dielectric constant, ϵ_r , of about

57, a dielectric loss, $\tan(\delta)$, of about 0.03, and a piezoelectric charge constant, d_{33} , of about 36 pC N^{-1} . With this, the composite has a piezoelectric voltage constant, g_{33} , of 71 mV m N^{-1} , which is about 3 times higher compared to the g_{33} of PZT. This means that the composite should generate 3 times more output voltage per applied force.

The bender box shown earlier in this chapter is made for both the PZT and composite bimorph, including the vane, with identical dimensions. Both of these are attached to a shaker moving the whole bender box in the direction perpendicular to the vane, which is the direction of the airflow when installed in the wind tunnel. The shaker was set to do a frequency sweep from 1 to 5 kHz. An accelerometer was attached to the shaker to measure the acceleration. Just as was used in the wind tunnel, an ultra-low input current CMOS amplifier was connected to the bimorph with a resistive load of $100 \text{ M}\Omega$. As stated before, this resistor has the aim to limit pyroelectric contributions causing large offsets in DC electric field which might result in overloading the amplifier. This resistor has the effect of a low cut filter, and the cutting frequency depends on the resistance of the resistor in reference to the capacitance of the piezoelectric element. Since the capacitance of the PZT and composite bimorph are vastly different (about a factor 30 apart), ideally an optimized resistance is chosen for each bimorph. In the case of the PZT bimorph, the resistance is chosen to be $100 \text{ M}\Omega$, while the resistance for the composite bimorph is ideally 30 times higher. However, a higher resistance also results in a more unstable signal more easily affected by environmental noise, and thus a 10 times higher resistance is chosen instead (i.e. $1 \text{ G}\Omega$). For a complete overview, both bimorphs are connected to both amplifiers. The output voltages of the piezoelectric bimorphs normalized to the measured acceleration is given in Fig. A1.

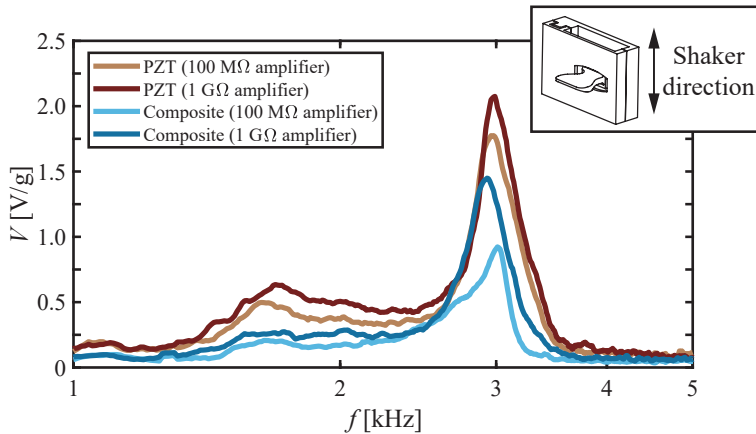


Figure A1: Bimorph output voltage, V , normalized to the mechanical acceleration versus frequency, f , comparing the PZT bimorph from this chapter to the manufactured composite bimorph having identical dimensions.

Firstly, the figure shows a clear resonance frequency of 3 kHz. This is, interestingly, nearly independent on the bimorph material. We have seen that if we remove the vane from the bimorph the peak almost completely disappears, and thus the resonance peak

is caused by the vane rather than the bimorph material. Considering the bimorphs connected to the 100 M Ω amplifiers, a difference of about a factor 2 is found between the composite and the PZT. Although the composite has a higher g_{33} , the high capacitance of the PZT bimorph still causes it to outperform the composite. Considering the bimorphs connected to the 1 G Ω amplifiers, both the PZT and composite bimorph output voltages are increased. However, the PZT output voltage increases with a smaller amount compared to the composite bimorph. Because of this, the difference between the PZT and composite bimorph becomes smaller, only a factor 1.5.

An interesting feature of the composite bimorphs is the small difference in frequency at which the peak voltage occurs. It actually looks like part of the peak of the composite bimorph using the 100 M Ω amplifier experiences a low cut filter, shifting the maximum to a slightly higher frequency. As stated before, this can occur due to the restive load, which has a low cut filter effect. This would also explain the larger gain in voltage experienced by the composite bimorph compared to the PZT bimorph.

In short, it seems that the low capacitance of the composite makes it unable to outperform the PZT, even though the g_{33} is higher. When using a bimorph with a larger area, it might be able to do so, because the area directly relates to the capacitance while it does not influence the g_{33} . The frequency spectra of the composite signal does look quite comparable to that of the PZT bimorph, and therefore it might work to use such materials instead for the application given in this chapter. However, for the remainder of this thesis we chose to continue to work with PZT bimorphs as they increase the chance of measuring the boundary layer accurately during the final part of this work, which is presented in Chapter 7.



6

OVERVIEW OF THE SMARTX WING TECHNOLOGY INTEGRATOR

This chapter describes the challenges of integrating smart sensing, actuation and control concepts into an over-sensed and over-actuated technology integrator. The hardware integration platform is chosen to be a wind tunnel model of a low-speed aircraft wing such that it can be tested in a large university-level wind tunnel. This hardware technology integrator is designed for multiple objectives. The nature of these objectives is aerodynamic, structural and aeroelastic, more specifically drag reduction, static and dynamic loads control, aeroelastic stability control and lift control. Enabling technologies, such as morphing, piezoelectric actuation and sensing, and fiber-optic sensing are selected to fulfill said objectives. The technology integration challenges are morphing and actuation integration, sensor integration, software and data integration, and control system integration. The built demonstrator shows the intended level of technology integration.

6.1. INTRODUCTION

Smart structures have been present since the dawn of aviation. The first heavier than air powered flight by the Wright brothers in 1903 was carried out with an aircraft that was able to twist morph its wings. Morphing was quite common in those pioneering years. However, aircraft became larger and heavier, and wing loading increased. This necessitated the wings to become stiffer to carry the increased loads, and this increased stiffness prevented the wing from morphing. The separation of functionalities in aircraft wings was introduced, where the wing load-carrying structure was separated from the rigid wing movables, which enabled the wing's high-lift and rolling capabilities [117]. Only a handful of later morphing aircraft examples can be found, and then mainly limited to experimental or military aircraft. Iconic examples are the F14 Tomcat and F111 Aardvark. However, since the 1980s, a renewed interest in smart structures for aviation has originated from the Active Flexible Wing (AFW), the Active Aeroelastic Wing (AAW), and the Aircraft Morphing and the Morphing Aircraft Structures programmes of the National Aeronautics and Space Administration (NASA) and the Defense Advanced Research Projects Agency (DARPA), amongst others [118–122]. On the civil aircraft side, the interest in smart structures for aviation has spiked in the European Union (EU) Framework Programmes (FP), more specifically FP5, FP6, FP7 and H2020. Much of the research in these programmes was focused on individual non-integrated morphing, actuation or sensing concepts. These programmes focused on topics such as, but not limited to, morphing using compliant mechanisms [123], span and chord morphing mechanisms [124] or aircraft sensing methods [125]. Only occasionally, hardware demonstrators contained multiple actuation or sensing concepts, such as, for example, in the EU FP7 Smart Intelligent Aircraft Structures (SARISTU) project [126]. A multitude of review articles has been written about the application of smart structures for aeronautical applications [2, 3, 127–130]. These review articles conclude that smart aeronautical structures for civil applications will be used for performance improvements of an aircraft to enhance the greening of aviation. They also stipulate that an integrated, multidisciplinary approach is needed. However, they observe that, relative to the numerical investigations that have taken place, very little smart structures concepts have been tested in the lab, wind tunnel or in-flight. An integrated closed-loop over-sensed and over-actuated wing hardware technology integrator is not investigated up to date. This is the aim of the technology that is described in this chapter.

6

A project called SmartX was started for this purpose at the Delft University of Technology, faculty of Aerospace Engineering, department of Aerospace Structures and Materials. The aim of this project is to investigate the feasibility of developing, manufacturing and testing such a multi-objective technology integrator with integrated smart sensing, actuation and control methodologies. The aim of this chapter was to provide an overview of the idea behind this next step in the development and maturing of smart structures of aeronautical applications, the SmartX project, as well as how this idea is translated concretely into a hardware technology integrator. More detailed descriptions of the individual contributing technologies and the results of the hardware test campaigns will be published in follow-up articles.

The philosophy behind these multiple objectives that this wing is designed for is explained in Section 6.2. The individual technologies that have contributed to this technology integrator are explained in Section 6.3. The way these technologies are integrated in a closed-loop sense is described in Section 6.4. Finally, the SmartX project overview is summarized in Section 6.5.

6.2. SMARTX PHILOSOPHY

The main objective of the SmartX project is the integration of smart sensing, smart actuation and smart control into one single hardware technology integrator meeting multi-objective purposes, defined below. The chosen integrator platform is a wing of a low-speed uninhabited aerial vehicle to be tested in the low-speed wind tunnels at the Delft University of Technology. The multiple objectives of the SmartX technology integrator are:

1. Drag reduction in cruise: the goal is to continuously optimize in real-time the wing shape during the cruise phase to constantly fly at minimum drag. This drag consists of two main components: (i) induced drag and (ii) profile drag. The shape of the wing is constantly adapted to generate a lift distribution that is close to elliptic to yield a constant downwash distribution and hence minimum induced drag. Secondly, the wing shape is adapted actively to increase the laminar boundary layer region over the wing surface, hence actively reducing skin friction drag, which is part of the profile drag.
2. Load control: minimization of dynamic and static flight loads will lead to a minimum structural mass to withstand the aerodynamic loads. Static flight loads are typically manoeuvre loads, while dynamic loads are gust loads. Static and quasi-static loads require low-frequency actuation, while gust loads require, depending on the gust length, high-frequency actuation. Hence, two types of (morphing) movables are necessary.
3. Aeroelastic stability control: the move towards aircraft structures of lower structural mass leads to more flexible wings. Such wings are more prone to aeroelastic instability such as flutter. Avoidance of flutter in a passive sense will lead to an increase in structural mass; hence the flutter phenomenon needs to be controlled in an active manner using the same control system that is used for gust loads control.
4. Lift control: in order to ensure that the aircraft lift always exceeds or is equal to its mass even in slow flight, the shape of the wing can be controlled automatically to provide high-lift capabilities.

The abovementioned multiple objectives are comparable to the objectives of the NASA Variable Camber Continuous Trailing Edge Flap (VCCTEF) project [131]. The three main differences are that (i) the SmartX objectives are to be achieved fully autonomously, that (ii) the closed-loop control to achieve these objectives is demonstrated using a hardware technology integrator and that (iii) the intended sensing, actuation and control technologies to be used are different. The main advantage of the SmartX project is the demonstration of the next step in Technology Readiness Level (TRL) of smart concept integration, which is a critical step in the development and maturing of the next generation of smart aeronautical structures.

To achieve the multiple objectives that are described above, we need to integrate several smart technologies in the areas of sensing and actuation. The goal of each actuation and sensing concept is explained here and elaborated further in Section 6.3.

1. **Slow morphing:** Morphing is chosen as the actuation concept instead of the use of discrete control surfaces. The reason is aerodynamic efficiency due to the seamless spanwise and chordwise morphing deformations. The slow morphing concept in this project should be able to seamlessly change the wing camber and twist in a distributed fashion. The morphing control surface is located at the wing trailing edge (TE) and can exhibit large deflections, which in this case means more than 20% of morphing flap length, at an operational quasi-steady frequency in the order of 0.1 Hz to 1 Hz.
2. **Fast morphing:** The fast morphing control surfaces are discrete tabs that are located at the very TE of the slow morphing control surfaces. The tab deflections are an order of magnitude smaller than the slow morphing control surface deflections, but their operational frequency is one order of magnitude higher, up to 50 Hz. This frequency range stems from the gust frequency requirements as specified by the certification specifications [132].
3. **Shape sensing:** Knowledge of the wing and morphing control surfaces shape is needed to obtain the exact control setting. This information is needed for closed-loop control purposes. It suffices for conventional rigid and discrete control surfaces to know the actuator setting since that determines the remainder of the control system behaviour unambiguously. This is no longer the case for morphing control surfaces since they exhibit a continuous and flexible deformation which is influenced by the actuator setting, the aerodynamic loads and the deflection of the neighboring seamless control surfaces. Therefore, knowledge about both the transient and steady-state wing and morphing control surface shapes is necessary.
4. **Boundary layer sensing:** Knowledge of the state of the boundary layer is important for the shape control both for in-flight cruise shape optimization and automated high-lift generation. Knowing whether the boundary layer is turbulent or laminar is important for cruise shape optimization, while knowing whether the boundary layer is attached or separated is important in case of automated high-lift. The flow sensing hardware must be integrated into the wing skin since it needs to be able to be operated in-flight.

An overview of which technology is used for which purpose is given in Table 6.1.

Table 6.1: SmartX objectives and related technologies

	Drag reduction	Load control	Aeroelastic stability control	Lift control
Slow morphing	✓	✓	-	✓
Fast morphing	-	✓	✓	-
Shape sensing	✓	-	-	✓
Boundary layer sensing	✓	-	-	✓

All of these interconnected technologies are to be realized on a wing with a span of 1.8 m and chord of 0.5 m, yielding an aspect ratio of 7.2 since the wing is cantilevered at the root. The dimensions of the wing are chosen such that it would fit into the Open Jet Facility (OJF) wind tunnel of the Delft University of Technology, which has a square cross-section of 2.85 m by 2.85 m. The design loads for the wing are determined by the maximum flow velocity of the OJF of 35 m s^{-1} . The wing is constructed of Glass Fiber Reinforced Plastic (GFRP) composite materials. More details about the wind tunnel model design can be found in [133].

6.3. SMARTX ENABLING TECHNOLOGIES

This section details the technologies introduced in Section 6.2. It discusses the slow morphing TE (6.3.1), the fast morphing TE (6.3.2), the fiber optic sensors (6.3.3) and the piezoelectric boundary layer sensors (6.3.4).

6.3.1. TRAILING EDGE SLOW MORPHING

The slow morphing concept is a concept that cambers and twists the TE of the wing in a frequency bandwidth of typically 0.1 Hz to 1 Hz. The SmartX slow morphing concept is based on the Translation Induced Camber (TRIC) concept that was developed at the Delft University of Technology [134]. The TRIC concept is a chordwise seamless morphing concept that exhibits large deformations and associated blocked force but, although being seamless, does not introduce locally large strains in the structure. This enables the use of off-the-shelf aerospace materials, which makes the morphing concept feasible and scalable for a wide range of aircraft classes.

The basic idea behind the TRIC concept is that the closed-cell of a control surface is cut to reduce its torsional stiffness. The cut that was introduced is closed using a linear actuator. Therefore, the control surface can be moved without virtually any resistance from the skin while the actuator is moving, but the control surface closed-cell obtains the actuator stiffness once the actuator is locked. The idea behind the concept is shown in Fig. 6.1. There, the slot in which the TE skin can move in the chordwise direction can be observed. The relative motion of the TE skin in the chordwise direction is ensured by the integrated linear actuator, which is located inside the wingbox. Each of the six morphing flaps is equipped with two actuators located at either side of the flap in the spanwise direction. The actuators are Volz DA 22-12-4112 servos selected for their high blocked force and position feedback capabilities, counting to 12 in total for all six modules. The cut-off frequency of the actuators is $\approx 2.6 \text{ GHz}$ (16.3 rad s^{-1}), and they allow an actuator peak-to-peak amplitude of 25° .

The SmartX hardware technology integrator is equipped with six TE flaps that contain the TRIC concept. These TE TRIC flaps cover the entire span of the wing and are equally spaced. The gap between each of the individual flaps is closed using a flexible elastomeric material to make the wing TE entirely seamless both in chordwise (due to the morphing concept) and spanwise (due to the elastomeric material) directions. The flexible elastomeric skin has been optimized such that a balance is found between the

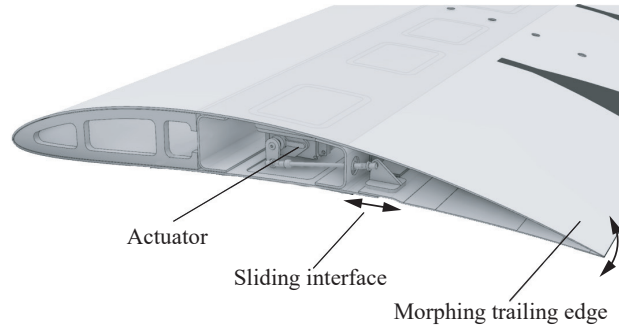


Figure 6.1: SmartX slow morphing concept: the TE can seamlessly move up and down.

desired tip flexibility and required actuator loads.

Within the intended bandwidth up to 1 Hz, the slow morphing concept can exhibit peak-to-peak TE deflections up to 15 mm upwards and 15 mm downwards and deliver a blocked force which is in the order of the applied loads that can be expected on a wing of the size of the SmartX hardware technology integrator.

6

Variable skin stiffness in the form of skin thickness tailoring ensures that the TE skin is sufficiently stiff to support the aerodynamic loads while it is flexible enough to allow the required deformations. The variable skin thickness is made possible by making use of ply drops of a composite skin. This is needed to obtain a smooth outer surface while matching a prescribed target shape for the control surface. A fluid-structure interaction routine was used to determine the most optimal ply dropping sequence. More details about this procedure can be found in Mkhoyan et al. [133]. The result of the optimization can be seen in Fig. 6.2 for a single slow morphing module.

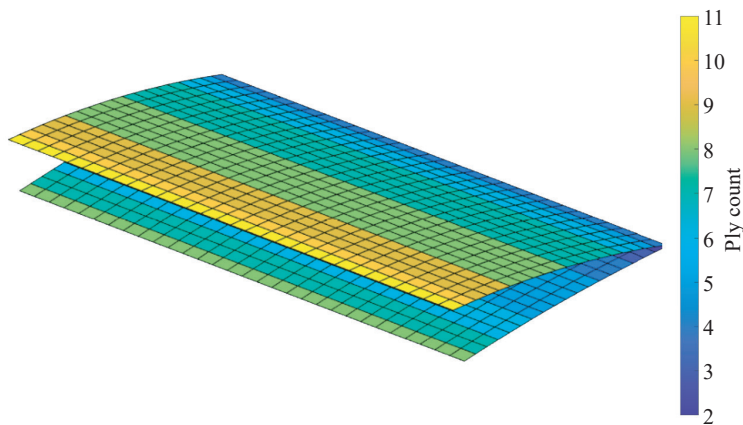


Figure 6.2: TRIC skin ply drop pattern (one layer has a thickness of 0.12 mm).

6.3.2. TRAILING EDGE FAST MORPHING

Along the morphing TE, 190 clustered piezoelectric bimorphs operating in the converse piezoelectric mode (i.e. an applied voltage induces a displacement) are installed to provide additional fast response morphing capabilities to the wing. Fig. 6.3 gives an overview of the bimorphs and how they were installed. Each bimorph was manufactured industrially and consists of a Pernifer 45 substrate layer, with PZT-5A4 piezoelectric ceramics bonded to either side. The choice of these materials was made because they are well-known proven technologies. The bimorphs have three free electrodes, one on either side and one connected to the Pernifer 45 substrate, making it able to connect the piezoelectric layers in parallel. The electrodes of ten bimorphs were connected in parallel using solder, resulting in 3 wire connections per 10 bimorphs. This means that separate actuation can be performed on each set of 10 bimorphs. They are fixed in the TE of the wing by filling the gap between the bimorphs and the top and bottom skins with epoxy resin, providing a free length outside the wing of about 35 mm. In total, 19 sets of 10 bimorphs are installed: three in the center of each of the six sections, with an additional one at the very tip.

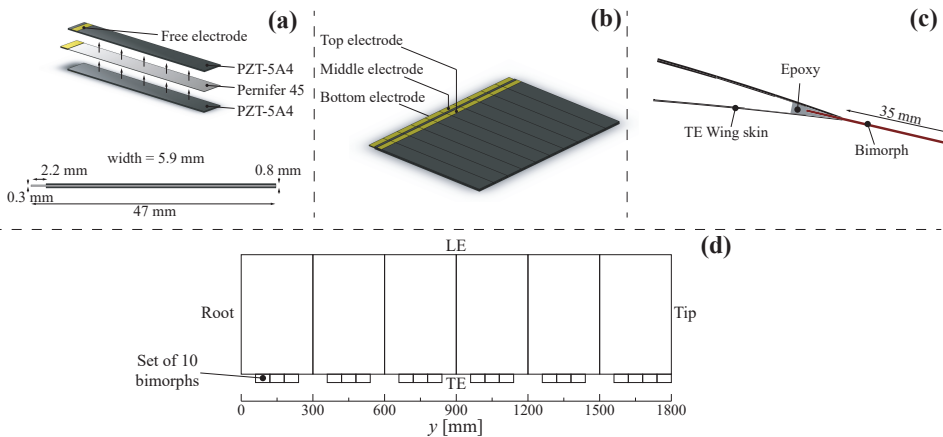


Figure 6.3: (a) Single piezoelectric bimorph. (b) Set of 10 bimorphs connected in parallel. (c) Cross-section of the TE. (d) Distribution of the 19 sets of 10 bimorphs in the SmartX wing.

Fig. 6.4 shows the circuit diagram connected to each set of 10 bimorphs. The inputs to the diagram are two drive signals, *Drive 1* and *Drive 2*, and one constant positive 200 V supply. The input drive signals are always 0 V or 5 V powering the switches, which are optical MOSFET switches. The input signals are directly coming from an Arduino controller. By powering *Drive1* or *Drive2* the bimorphs can be actuated up or down, while by powering none of the two, they are left in the neutral position. If for any reason both *Drive1* and *Drive2* are powered, they also keep their neutral position. The benefit of this circuit is that only one 200 V power supply is required to actuate the bimorphs, while the limitation is that only three settings can be realized: bend down, neutral and bend up.

The response time of the circuit is about 2 ms. However, a more limiting factor is

the amount of current the 200 V supply can provide. Whenever one set of 10 bimorphs is switched on, it draws a significant amount of current. The total amount of power required linearly scales with the number of sets switching simultaneously. The maximum power required is limited by limiting the maximum operating frequency to 50 Hz, yielding a system response time of 20 ms. Using frequencies up until 50 Hz, the bimorphs are able to obtain a peak-to-peak tip deflection of about 2.50 mm (+1.25 mm bend up and -1.25 mm bend down).

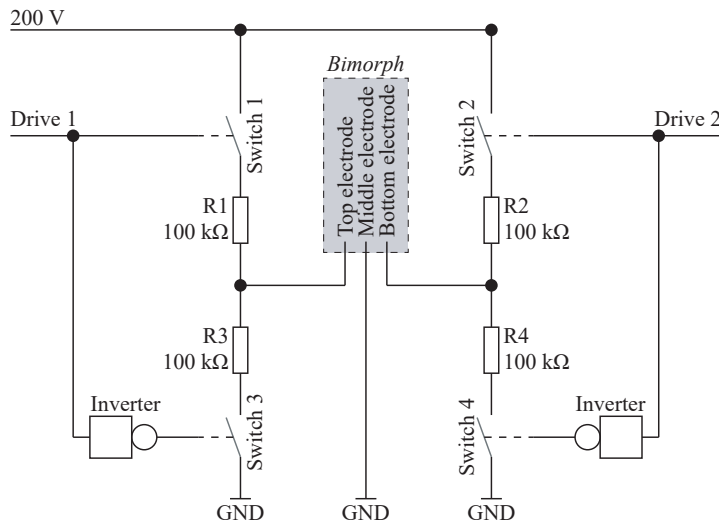


Figure 6.4: Circuit diagram powering one set of 10 piezoelectric bimorphs connected in parallel.

6.3.3. FIBER-OPTIC SHAPE SENSING

Wing shape changes influence the aerodynamics and are also considered as a source of load acting on the wing. For load alleviation purposes and closed-loop control, shape sensing and wing deformation monitoring are necessary.

The wing contains a total of 14 optical fibers. Fig. 6.5 shows the layout of the fibers that are bonded onto the skin and connected to the fiber connector hub. This layout was chosen to capture the morphing behavior including bending and torsion. The six independent morphing modules and the wingspan structure contain two fibers each, one on the upper surface and one on the lower surface.

A multi-modal fiber-optic principle is incorporated that involves a combination of spectral sensing for local sensor measurement and interferometric sensing for measuring between sensor pairs. This sensing method was chosen to measure simultaneously at particular points as well as along given pathlengths. This method also allows capturing more data while keeping the number of fiber Bragg grating (FBG) sensors to a minimum.

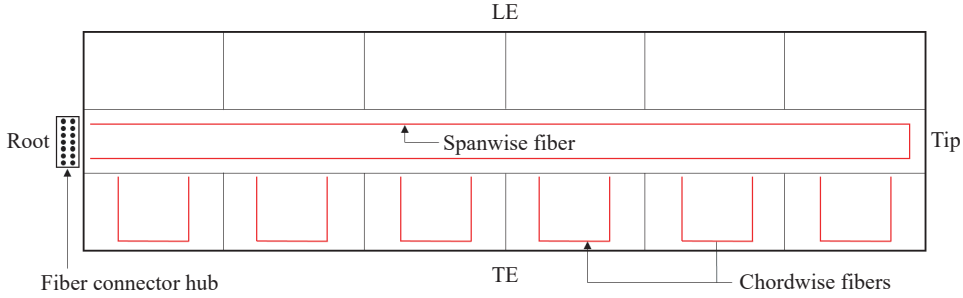


Figure 6.5: Layout of the spanwise and chordwise optical fibers (in red) on the SmartX wing. Connections to the 14 fibers are through the fiber connector hub.

Fig. 6.6 shows the fiber layout and FBG location of one of the morphing modules. All the fibers on the wing are custom (Corning ZBL SMF-28e) single-mode fibers with FC/APC connectors and contain 4 FBG sensors each. The FBGs have high reflectivity (>84 %) and bandwidth (>0.85 nm). Each grating is 3 mm long and operates in the C-band wavelength range (1530 nm - 1565 nm). These parameters were particularly chosen to conform with the capabilities of the interrogators used.

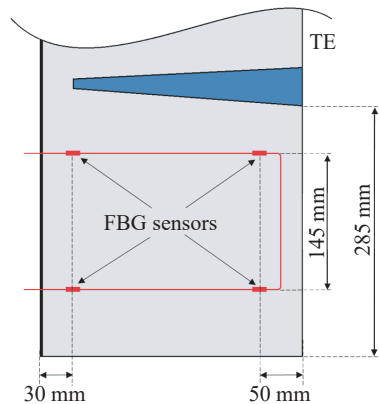


Figure 6.6: Location of the fibre (in red) and the FBG sensors on one of the morphing modules.

When the fibers, and in turn the gratings, are subjected to external mechanical (or thermal) perturbations, two optical changes are introduced that are vital for capturing the shape of the wing. The output of the first change gives the local strain measurement at the location of the grating measured by a spectral sensing interrogator. The second change gives the displacement between any two gratings measured by an interferometric sensing interrogator.

Each of the six morphing modules (and the wingspan) have a *U-shape* fiber layout parallel to the axis of bending and symmetric to their central axes (Fig. 6.6). During bend up and bend down, the two fibers undergo similar loading whilst during twisting,

one fiber experiences tension and the other experiences compression. The coupled motion of bend up, bend down and twist is analyzed to interpret the morphing nature and to estimate the current shape of the wing surface. To determine the shape, a 'Wing Section Morphing to Optical Fiber Strain to Deformed Shape' transfer function is used to relate the strain outputs to the final shape. As the ZBL SMF-28e fibers are capable of withstanding larger deflections due to their high tensile strength, the actual limitations are set by the morphing and structural design.

The hybrid sensing approach also aims to reduce the overall costs by considerably reducing the cost of the fibers. This is realized by using the least number of gratings per fiber. Additional studies using this sensing approach have shown that the total number of fibers required can essentially be reduced to seven for the SmartX wing without compromising the accuracy; i.e. one for each of the six morphing modules (chordwise) and one for the wing (spanwise) [135]. In short, a single morphing surface requires just one fiber containing four FBG sensors. Furthermore, once properly calibrated, this fiber-optic methodology is capable of identifying the position and magnitude of an external load acting on the morphing surfaces. The data acquired can be integrated with the control loop for real-time feedback for load monitoring and load alleviation purposes.

6

6.3.4. BOUNDARY LAYER SENSOR

Boundary layer sensors are installed to distinguish between various boundary layer states, which can be used for drag optimization. Sixteen boundary layer sensors, relying on piezoelectric bimorphs, are embedded in the top skin of the SmartX wing. In this case, the bimorphs have a size of 3 mm width and 10 mm length and are operated in the direct piezoelectric mode (i.e. an experienced load results in an electrical signal). Using a 3D printer (Ultimaker 3, Ultimaker B.V., Utrecht, The Netherlands), a polylactic acid (PLA) box was 3D printed to house the piezoelectric bimorph sensors. About 2 mm of the piezoelectric bimorph length was clamped in one of the walls of this box, leaving a free length of 8 mm. On the free end of the piezoelectric bimorph, a 3D printed PLA vane was glued using cyanoacrylate adhesive. This vane later pierced the skin of the airfoil to mechanically couple the boundary layer to the piezoelectric bimorph. The vane reached a height of about 1.7 mm above the airfoil skin and had a width of 6.0 mm. A schematic representation of the piezoelectric bimorph including the vane inside the box is given in Fig. 6.7. Under these boundary conditions, the natural frequency of the sensor was measured to be about 3 kHz in the direction of the flow.

An ultra-low input current CMOS amplifier was directly connected to both outer electrodes of the piezoelectric bimorph, connecting the piezoelectric layers in series, providing a resistive load of 100 M Ω . The amplifier copies the voltage obtained from the piezoelectric bimorph, amplifies it and drives a data acquisition unit without signal loss due to wiring and circuit load. To minimise the environmental noise, the wires between the piezoelectric bimorph and amplifier were taken as short as possible. The amplifiers were mounted on the bottom of the PLA box simply using double-sided tape, requiring only a couple of centimetres of wire between the bimorph and amplifier. To obtain as much information from the sensors as possible, frequencies up to the resonance

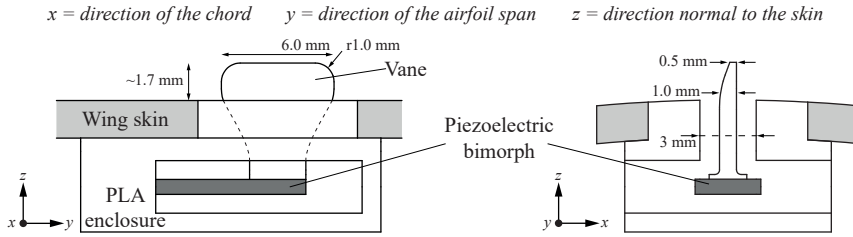


Figure 6.7: Schematic representation of a piezoelectric bimorph sensor mounted underneath the airfoil skin. The vane is piercing the skin to transfer the oscillations from the boundary layer to the piezoelectric bimorph.

frequency of 3 kHz have to be captured. This requires a sampling frequency of 6 kHz to prevent aliasing.

In total, sixteen sensors are installed, divided into two rows of eight. This way, information on the local boundary layer state in both chord and span direction can be obtained. One row is positioned near the root of the wing, while the other is located near the tip, as shown in Fig. 6.8. They are positioned such that the turbulent wedge created from one of the sensor vanes does not influence the measurement of any of the other sensors located downstream. The sensor boxes were mounted before the wing skins were joined together. The boxes were glued using epoxy resin in pre-drilled 9 mm holes on the inside of the top skin. The wires from the amplifiers were routed directly towards the leading edge (LE) through pre-drilled holes in the spars. They then move along the LE towards the root of the wing.

In the current configuration, the data of the 16 sensors sampled simultaneously are analyzed offline using fast Fourier transforms. This allowed the reconstruction of the location of laminar-to-turbulent transition in direction of the chord. Research towards more rapid data analysis is ongoing to be able to use the sensor signal as online input for the controller.

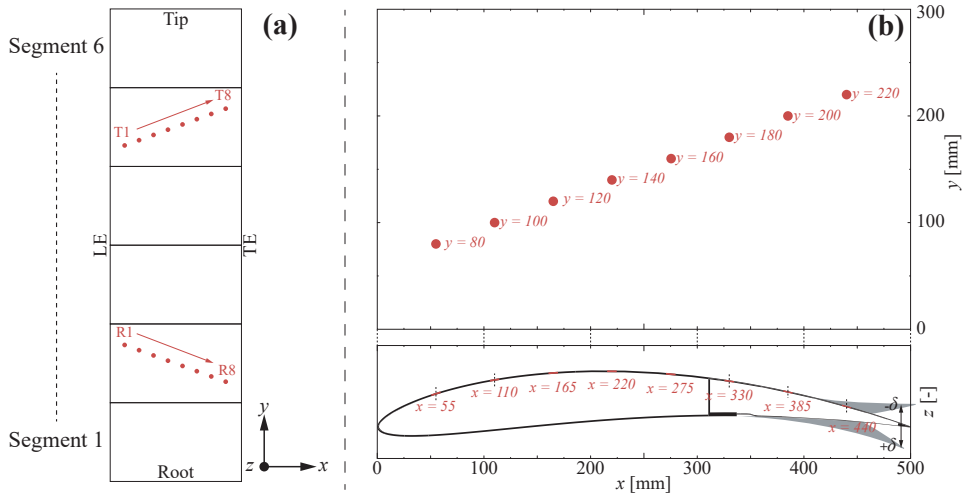


Figure 6.8: (a) Sensors locations (red circles) and wire paths (blue arrows) installed in the top skin of the SmartX wing. (b) Coordinates of sensors installed within a single section.

6

6.4. SMARTX TECHNOLOGY INTEGRATION

To achieve the objectives outlined in Section 6.2, SmartX integrates several state-of-the-art technologies, which were explained in Section 6.3, into a hardware technology integrator capable of continuous autonomous control. This wing technology integrator, called the SmartX-Alpha, is composed of several closely integrated building blocks as shown in Fig. 6.9. The technology integration can be divided into several system-level segments:

1. Morphing module and actuator system integration: the slow and fast morphing concepts;
2. Sensor system integration: the fiber optics and the flow sensors;
3. Software and data integration: streamlining the acquired signals and fusing redundant and distributed sensor information into a hybrid output;
4. Control system integration: sensor data fusion and feedback to the morphing modules.

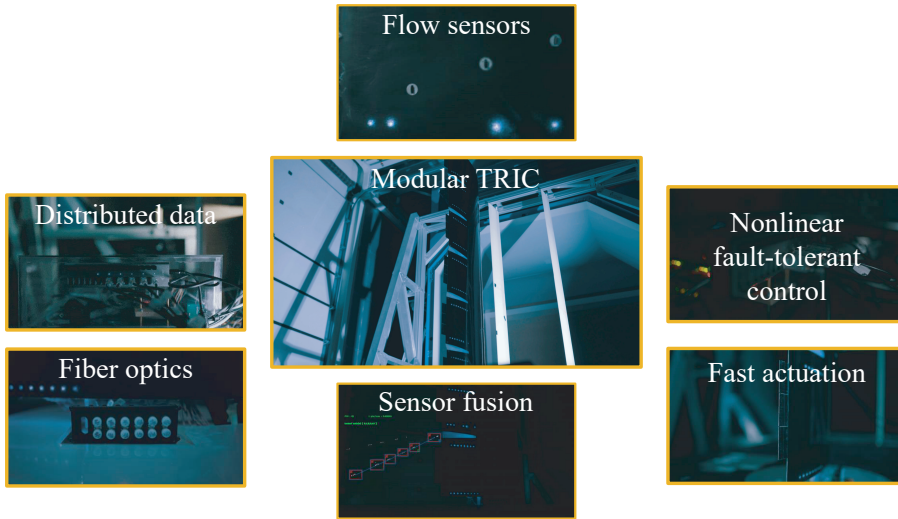


Figure 6.9: The SmartX integration blocks.

6.4.1. MORPHING MODULE AND ACTUATOR SYSTEM INTEGRATION

The SmartX technology integrator uses slow and fast morphing concepts, as described in Section 6.3. The arrangement of both morphing concepts is as follows. The TRIC morphing modules are located at the TE of the technology integrator while the fast morphing piezoelectric benders are mounted onto the TE of the TRIC morphing modules. An overview of the design of the wing is presented in Fig. 6.10 and described in more detail in [133].

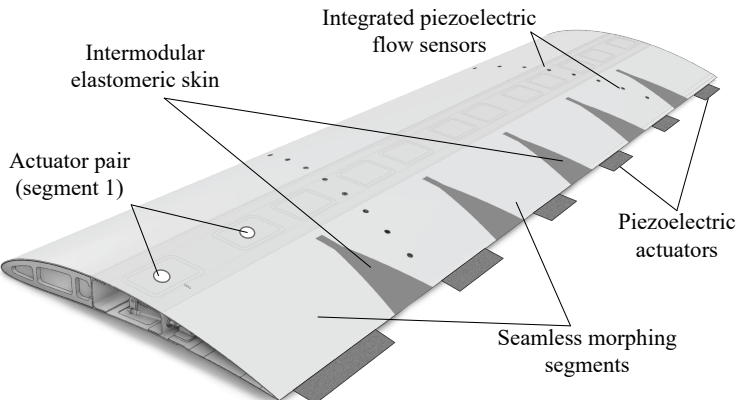


Figure 6.10: SmartX-Alpha sensor hardware integration.

6.4.2. SENSOR SYSTEM INTEGRATION

Next to the state-of-the-art sensor technologies described in Section 6.3 the wing was equipped with conventional strain gauges (for reference purposes only) and LEDs for a novel vision-based wing motion tracking system described in [136, 137]. These sensors are integrated into the wing at the early stage of the manufacturing process. Fig. 6.11 shows the integration of the components at the final stages of the manufacturing with the top and bottom wing halves exposed. The components are bonded with a thickened epoxy resin using cotton flocks and reinforced with a fiber-glass wrapped foam wedge. The cabling is routed from the TE via the rear spar and exited the root either via the D-box or the wing-box. The actuator base, holding the servos, LEDs circuit and the piezoelectric boundary layer sensors are bonded on the upper skin. The fast morphing actuators were bonded to the bottom. The fiber optic sensors are bonded with a fast curing bonding compound to both upper and lower skins. Sufficient slack is given to ensure that the wiring and optical fibers do not restrict the motion of the morphing modules.

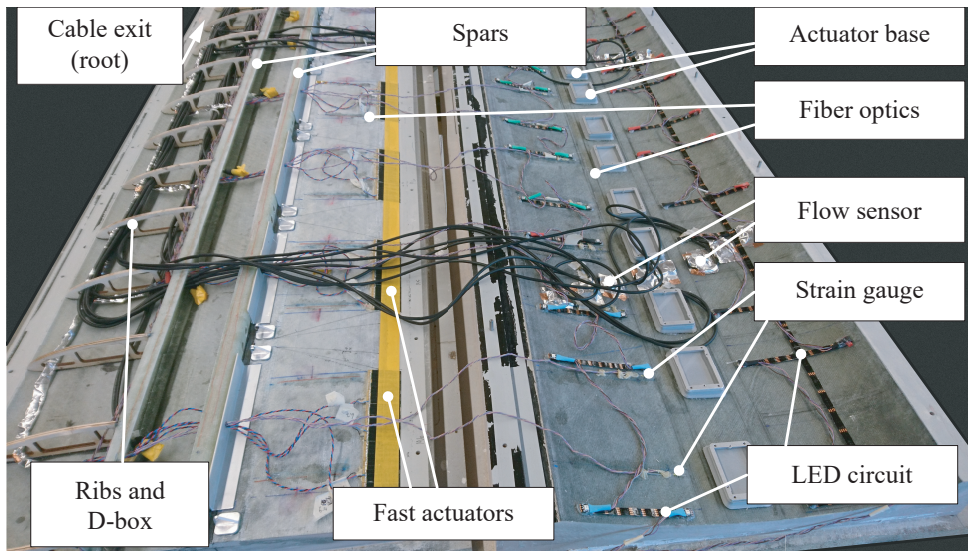


Figure 6.11: SmartX-Alpha sensor hardware integration and manufacturing.

6.4.3. SOFTWARE AND DATA INTEGRATION

Due to its modular design and multi-actuation and multi-sensing capabilities, the number of sensors and actuators and their hardware controlling components increase with multiples for each module. To allow real-time control of numerous actuators and sensors, a distributed data-sharing architecture is developed. The structure allows parallel integration of hardware and software components. The software architecture is developed in C++ with the real-time D-SIM framework, connecting several PC nodes over a local Ethernet network [138]. D-SIM is a framework written in C++, that facilitates the synchronisation of real-time variables over a distributed Ethernet network. The resulting architecture allows integration in native C++ software components as well as standard-

ised industry and academic software packages (LabView, MATLAB, Simulink). Various off the shelf boards and cards (microcontroller boards, digital-to-analogue converter systems) and custom-built components (driver circuits, microcontroller units) can be integrated into the architecture.

6.4.4. CONTROL SYSTEM INTEGRATION

At the center of the controller hardware are 12 servos commanding the morphing shapes of six TE modules. These actuators are connected to an array of RS-485 devices communicating serially via the RS-485 protocol over a single physical USB bus updating to a D-SIM node. With the given RS-485 hardware configuration, the maximum achievable communication update rate was 67 Hz. The actuation angles of the servo are constrained to $\pm 25^\circ$ as to not exceed the physical limits of the system. The TE fast morphing actuators are bundled into 19 sets of controllable actuator units requiring two logic level driver signals (0 - 5 V) each. These 38 signals are regulated by three micro-controllers boards equipped with Atmel 2560 Microcontroller [139]. Driver signal is frequency modulated on the microcontroller allowing independent control of the oscillating frequency for each actuator. A Simulink program is integrated into the software architecture running the control law real-time, with new control input updates entering at 200 Hz. An external balance system and integrated strain gauges allow measuring the three-axes root reaction forces and moments required for the controller. The central control law consists of an Incremental Nonlinear Dynamic Inversion (INDI) with Quadratic Programming (QP) control allocation [140]. The incremental control was designed to guarantee robustness against model uncertainties, external disturbances and fault tolerance in the event of actuator failure.

6.5. SUMMARY AND CONCLUSIONS

The present work shows that it is indeed possible to design and construct a wind tunnel model for an aircraft wing in which the following objectives are integrated simultaneously: (i) real-time drag reduction in cruise, (ii) static and dynamic load control, (iii) aeroelastic stability control and (iv) lift control. Selected smart technologies to enable these simultaneous objectives were: (i) slow morphing control surfaces, (ii) fast morphing actuators, (iii) fiber-optic sensors and (iv) piezoelectric flow sensors. The integration of the actuation and sensing is demonstrated, as well as the software and data fusion methods to make the sensor data of the over-sensed wing suitable for feedback control. The control methodology itself is also described in this chapter.

Future publications will detail the individual SmartX technologies as well as the bench tests and wind tunnel tests results.



7

IN-SITU BOUNDARY LAYER TRANSITION DETECTION ON MULTI-SEGMENTAL (A) SYNCHRONOUS MORPHING WINGS

This chapter presents an experimental method to detect in-situ the location of transition on a multi-segmental trailing edge camber morphing wing during synchronous and asynchronous morphing. The wing consists of six independently morphing segments with two of the segments instrumented with eight embedded piezoelectric sensors distributed uniformly along the chord. Using suitable data processing, each of the sensors gives a signal that can be used to determine the state of the boundary layer (laminar, transition, turbulent) at the location of that sensor. The results showed that the location of transition at a given angle of attack can be shifted significantly (up to 20%) by synchronous morphing, in particular for angles of attack below 9° . Modest differences in the location of transition are found between the near-root and near-tip segment. Using a dedicated data processing approach, the location of transition could be reconstructed in case of complex asynchronous morphing involving one to five segments. The results show a shift in the location of transition when morphing neighboring segments, but also show that non-neighboring segments have a minimal effect. The method holds significant promise for online advanced morphing control to move transition towards the trailing edge and thereby reducing skin friction drag.

7.1. INTRODUCTION

The aerodynamic efficiency of aircraft is defined by the lift-to-drag ratio, which is strongly influenced by the type of boundary layer the wing experiences [40, 105, 106]. A way of minimizing the drag is to make a large fraction of the flow over a wing laminar, which possesses lower skin friction drag compared to turbulent flow. This is therefore often the motivation to move the so-called laminar-to-turbulent transition towards the trailing edge (TE) of a wing. One way of achieving this is through passive means, i.e. by designing for it. Typical examples are natural laminar airfoils [107, 141]. Active means include the operation of micro-actuator devices such as jet or plasma actuators [108, 109, 111], and hybrid laminar flow [142].

Morphing wings provide another active way of moving transition, as they affect the boundary layer surrounding them upon changing shape [2, 3, 143]. Studies have shown that by using morphing wings with an active extradors structure transition can be moved with about 10% to 20% of the chord length [144]. The idea of a so-called morphing laminar wing is to have the wing change its shape such as to push the transition as close to the TE as possible to lower the overall skin friction drag. In order for such a system to work, one of the input variables required is the location of transition itself. However, the determination of the location of transition becomes complicated when considering a three dimensional flow, i.e. a wing with a free tip, as the tip vortex can locally lower the effective angle of attack. Because of this, the location of transition becomes a function of the spanwise location with transition closer to the TE near the tip of the wing [145]. Another complication occurs when a camber morphing wing has separate segments distributed along the span which can be actuated individually, enabling synchronous and asynchronous morphing, further increasing the dependence on spanwise location. Such an over-actuated wing has more variables than degrees of freedom, and hence is thought to be able to provide a higher lift-to-drag ratio by actuating appropriate patterns of segmental deflection.

One way to obtain the location of transition is through analytical models. This was proven to work for two-dimensional flows on morphing wings with an active extradors structure [144, 146, 147]. Unfortunately, the complications discussed above (three dimensional flow and asynchronous multi-segmental morphing) will make such models less accurate and wing-specific. Another way is to use sensor systems capable of detecting the location of transition. Typically such sensor systems rely on pressure or sound transducers [49, 50, 99], hot film sensors [51–53, 100], Infrared (IR) thermography [44–46], or shear stress measurements [54, 55, 101, 102]. Unfortunately, measurement techniques like these are either restricted to wind tunnel environments or require a high number of sensors to meet the required spatial resolution.

In recent work we have shown the use of piezoelectric bimorph sensors installed underneath the airfoil skin with small vanes piercing through the skin to detect vibrations in the boundary layer [58]. Such sensors were able to locally distinguish between laminar, turbulent and separated flow, and showed a clear amplitude peak at transition. Such sensors still suffer from the fact that the spatial resolution is limited to the number of

sensors installed, but this can mathematically be overcome by using the output of these sensors as a state variable. This can be done because, for a given free stream velocity and angle of attack, the value of their average amplitude over a well selected frequency domain is proven to be linked to the local boundary layer state. By installing multiple non-interacting sensors in a wing and recording their average amplitude for a range of angles of attack and morphing deflections, a database can be built containing typical state variable values of all sensors which can be related to the location of transition. The state variable values obtained during any new measurement can then be compared to the ones stored in the database. Using a minimization algorithm, unique combinations of the angle of attack and morphing deflection can be determined, which in turn relate to the location of transition. As the found angle of attack and morphing deflection can be regarded as the effective angle of attack and morphing deflection of the morphing wing segment, this method can also be applied to cases where asynchronous morphing is applied. In that case, the imposed angle of attack and morphing deflection possibly do not match the physical angle of attack and morphing deflection found in the database, because morphing neighboring segments can effectively change the boundary layer on the instrumented segment. Therefore, using this method, this difference can be quantified, and the location of transition can be detected on a complex asynchronous morphing wing with only a limited number of sensors.

In this work, sixteen piezoelectric sensors, identical to the ones shown in earlier work [58], are installed in a NACA 6510 TE camber morphing wing containing six morphing segments along the span. Due to an elastomeric interface in between the individual morphing segments, the wing has a seamless continuous TE even while actuating each segment independently [5, 133]. The wing is tested in a wind tunnel of the Delft University of Technology (TUD). Eight sensors are installed in direction of the chord in the second and the fifth morphing segment of the wing. First, measurements during synchronous morphing are performed, morphing all the segments equally. A broad range of angles of attack and morphing deflections is covered. Using these measurements, the database is built to identify the unique amplitude of each sensor per angle of attack and morphing deflection. This database is then used to investigate asynchronous morphing cases to detect how morphing one or more neighboring segments affects the local transition on the instrumented segment. This will grant us unique insight into the shifts in transition on multi-segmental morphing wings during asynchronous morphing. With a future speed-up of the data acquisition and processing protocols such sensors might be used for in-situ control loops to dynamically optimize the wing shape real-time.

To our knowledge, the deployment of such a sensory system on such a complex multi-segmental TE morphing wing has not been done before. Insights into the potential use of such a system and insight into the development of the location of transition on morphing wings will therefore act as the main contributions of the present work to the field.

7.2. EXPERIMENTAL SETUP

This section discusses the hardware setup (7.2.1), the procedure used to interpret the piezoelectric sensor signals (7.2.2), the method used to work with the created database of sensor amplitudes (7.2.3) and the experimental program (7.2.4).

7.2.1. HARDWARE SETUP

The wind tunnel experiments were performed in the Open Jet Facility (OJF) in the High Speed Laboratory at the Delft University of Technology (TUD). The OJF has a tunnel outlet of 2.85 x 2.85 m and can provide an airspeed up to 35 ms⁻¹. The wind tunnel features a rotation table which enables remote control over the angle of attack.

The morphing wing was developed at the TUD, called the SmartX wing. Under zero morphing conditions, the wing has a NACA 6510 profile with a chord length of 0.5 m and a span of 1.8 m. The morphing concept used in the SmartX wing is based on the Translation Induced Camber (TRIC) concept that was also developed at the TUD [134]. The cross section of the wing showing this concept is shown in Fig. 7.1. It uses a sliding interface where the skin can be retracted or extended in order to deflect the trailing edge down or up, respectively, using an actuator positioned in the wing box. The skin is made from glass fiber reinforced epoxy with a tapered thickness, which provides the desired balance between material stiffness and compliance in order to obtain seamless chordwise morphing. The wing is divided into six segments of an equal width of 0.3 m, each capable of morphing individually. In order to obtain a continuous TE under all morphing conditions, a silicone rubber interface connects two adjacent morphing segments. Each segment is capable of deflecting the tip of the TE, δ , from -15 mm to +15 mm from its neutral position, with positive deflections increasing lift, i.e. deflecting down [133]. It should be noted that these deflections were measured without any aerodynamic load applied, and therefore, actual in-flight deflections may differ. However, in this work the exact values of δ are not relevant, and we therefore simply use the values measured without any aerodynamic load. For a complete overview of the SmartX wing, see the SmartX overview paper [5], which is also presented in the previous chapter.

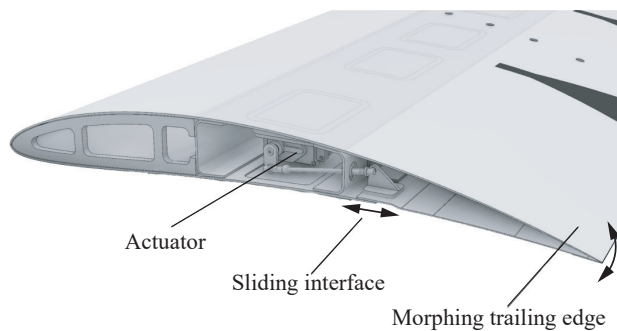


Figure 7.1: Trailing edge camber morphing concept of the SmartX wing [5, 148].

In order to measure transition on the suction side of the wing, two rows of eight piezoelectric sensors are installed. Fig. 7.2 provides an overview picture of the wing in the wind tunnel, with the red dots signifying the two rows of eight piezoelectric sensors (note that not all eight are visible due to the curvature of the wing). The first set of eight sensors were installed in the second segment near the root of the wing, as is shown in the schematic given in Fig. 7.3. They were spaced 55 mm apart in direction of the chord and 20 mm apart in direction of the span, resulting in an angle of about 20° behind one another. Such an angle is sufficient to make sure the turbulent wedges generated by a sensor to not influence the measurement by another sensor downstream. The second set of eight sensors were installed in the fifth segment near the tip of the wing, using the same spacing in a mirrored manner.

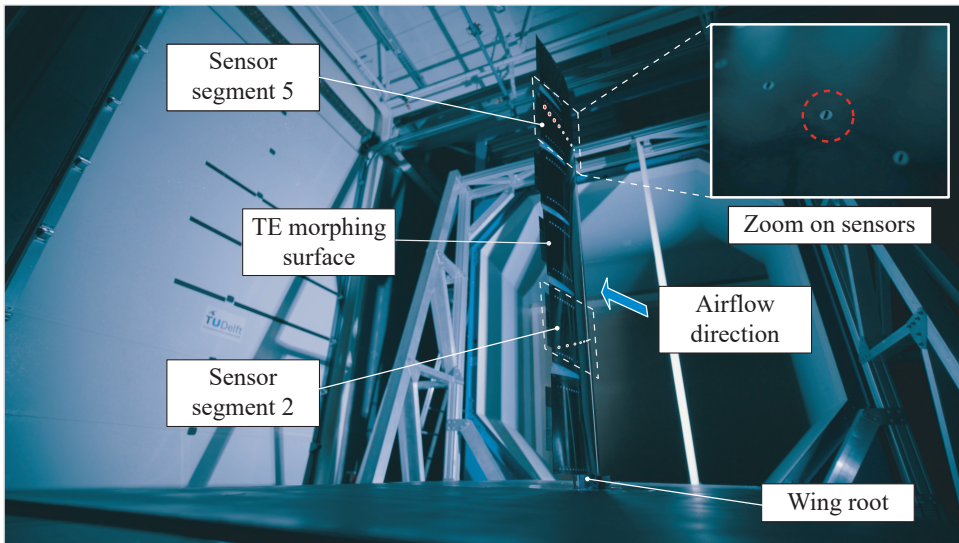


Figure 7.2: Experimental setup in the OJF wind tunnel of the TUD. The highlighted red dots signify the locations of the visible sensors.

The sensors used in this work are identical to the ones used in previous work [58]. In this earlier work, Particle Image Velocimetry (PIV) measurements proved that such sensors are able to measure the state of the boundary layer, such as transition, over a classical rigid NACA 0012 airfoil. The sensors rely on the direct piezoelectric effect, i.e. generating a charge upon an applied mechanical force. They consist of piezoelectric bimorphs clamped in a 3D printed (Ultimaker 3, Ultimaker B.V., Utrecht, The Netherlands) polylactic acid (PLA) enclosure mounted underneath the top skin of the wing. On the free end of the piezoelectric bimorph a 3D printed PLA vane was glued using cyanoacrylate adhesive. This vane was installed such to protrude through an opportune opening in the skin of the wing to mechanically couple the external flow to the piezoelectric bimorph. The vane reached a height of about 1.7 mm above the wing skin, and had a width of 6.0 mm. A schematic representation of the piezoelectric bimorph including the vane

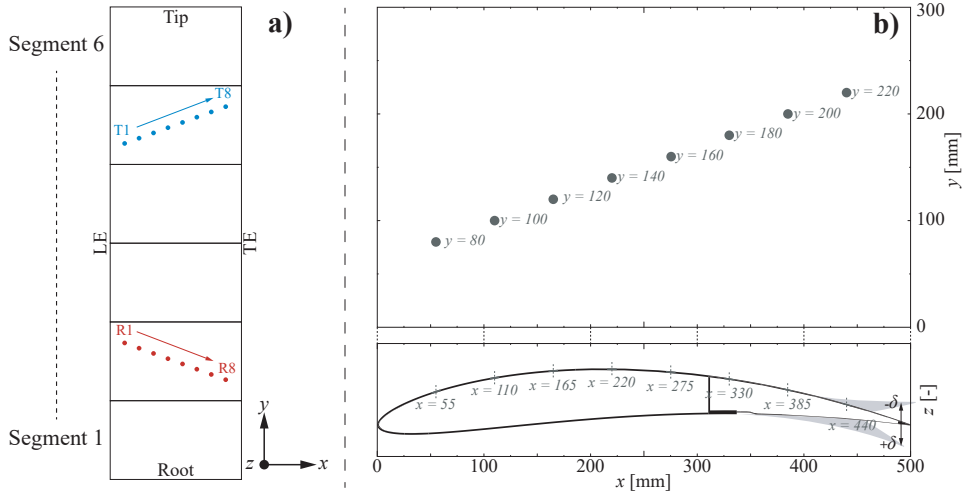


Figure 7.3: Schematic overview of the SmartX wing. (a) The piezoelectric sensors are installed in the second and the fifth segment. (b) Detailed sensor positions within a single segment.

inside the enclosure is given in Fig. 7.4. Using a shaker, the natural frequency (first mode) under these boundary conditions in the direction of the flow was measured to be about 3 kHz.

7

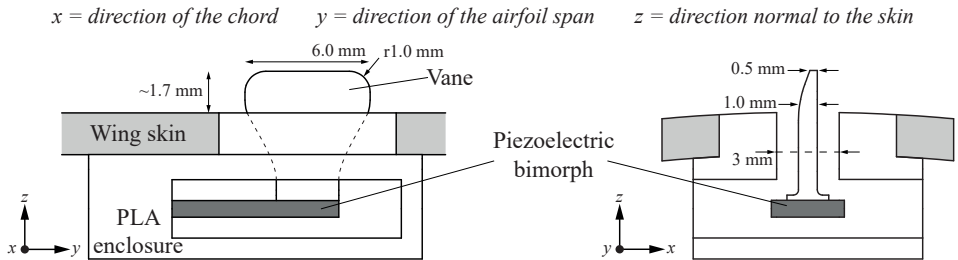


Figure 7.4: Schematic representation of the piezoelectric bimorph inside a PLA enclosure mounted underneath the wing skin.

An ultra-low input current CMOS amplifier was directly connected to both carbon electrodes of the piezoelectric bimorph, providing a resistive load of 100 M Ω . The amplifier copies the voltage obtained from the piezoelectric bimorph, amplifies it, and drives a data acquisition unit without signal loss due to wiring and circuit load. To minimize environmental noise, the wires between the piezoelectric bimorph and amplifier were kept as short as possible, in the range of a couple of centimeters. The amplifiers send the analogue signal to a data acquisition unit (Simcenter SCADAS Mobile, Siemens), which converts it to a digital signal, at a sampling frequency of 40 960 Hz per sensor channel. In each case all sixteen sensors measured simultaneously during a 10 s time window. After

that, data processing, including fast Fourier Transform (FFT), was performed offline.

7.2.2. PIEZOELECTRIC SIGNAL INTERPRETATION

Earlier work has shown the capability of the sensors used in this work to locate transition on a NACA 0012 airfoil in low Reynolds numbers [58]. Using the same technique, transition can be located on the SmartX wing as well. In the earlier study, it was found that frequencies above 100 Hz relate to transition. Examples of typical output signal profiles measured by a single sensor (sensor R7) at three angles of attack, are shown in Fig. 7.5. A clear output voltage dependence on the angle of attack is observed, which is directly caused by the state of the boundary layer exciting the sensor vane. Generally, laminar flow provides a low voltage, which in this case is at an angle of attack of 2° . At transition, vibrations in the flow tend to maximize [50]. This is measured by the piezoelectric sensors, and hence the highest voltage measured at an angle of attack of 6° signifies that transition lies closest to this sensor at this angle. The 3 kHz peak occurs due to the resonance frequency of the sensor itself. The frequencies in a turbulent boundary layer occur over a broad range of frequencies in the kHz range, causing to specifically amplify this resonance frequency. Therefore, this particular frequency has no relation to the boundary layer itself, but the magnitude of this peak does provide information about the turbulence in the boundary layer.

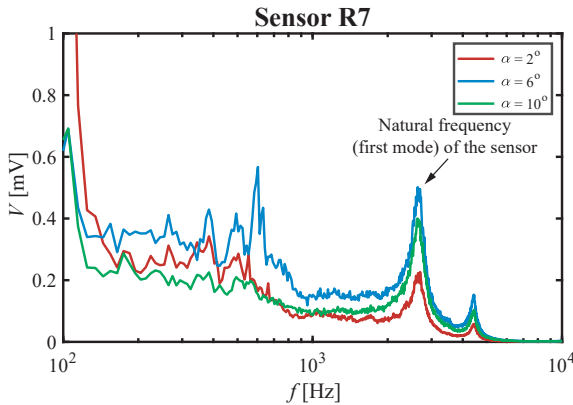


Figure 7.5: Measured voltage, V , of sensor R7 versus the frequency, f , and angle of attack, α , without morphing the wing ($\delta = 0$ mm).

Fig. 7.6 shows the same data as is shown in Fig. 7.5, but now as a contour plot including all measured angles and all eight sensors installed in segment 2. In general, moving along the y -axis from low to high angle of attack, first a low intensity region is encountered. This is the regime where the boundary layer is laminar. Sensors R5 to R8 show a regime where the output voltage peaks for certain angle of attack. This is when transition has shifted to the location of the sensor. For higher values of angle of attack the local flow remains turbulent.

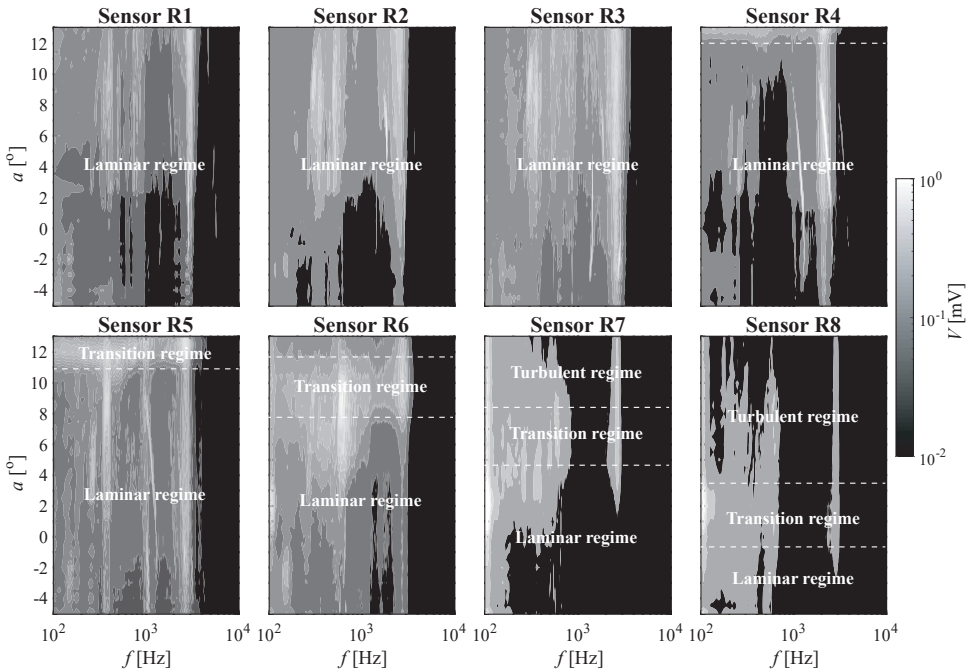


Figure 7.6: Measured voltage, V , of segment 2 as a function of frequency, f , and angle of attack, α , without morphing the wing ($\delta = 0$ mm).

7

As mentioned before, the transition process is related to the signals measured above 100 Hz. The complex information in Fig. 7.6 can be simplified by integrating over the frequency from 100 Hz to 5000 Hz. The signal above the upper limit of 5000 Hz is only related to noise. The average amplitude as a function of the angle of attack for each of the eight sensors in segment 2 (indicated by R1 to R8) and segment 5 (indicated by T1 to T8) are shown in Fig. 7.7. We now clearly see a maximum amplitude occurring at different angles of attack for each sensor, while for some sensors that maximum does not seem to occur in range of the measured angles. From these peaks, we can deduce at what angle of attack transition occurs at which fixed position on the chord.

Comparing the location of transition measured in segment 2 and 5, significant differences are found. In both cases, only sensors 5 through 8 find a clear transition peak, albeit at slightly different angles. This difference is not surprising as the tip vortex plays an important role in the location of transition, and segment 5 most likely experiences this tip vortex more intensely. Comparing sensor locations to one another, it is also observed that the peaks measured near the TE (sensor R8 and T8) are relatively broad, while they become more narrow as we move towards the LE. This is an indication that the transition process becomes more abrupt as we increase the angle of attack. This makes sense as increasing the angle of attack increases the adverse pressure gradient,

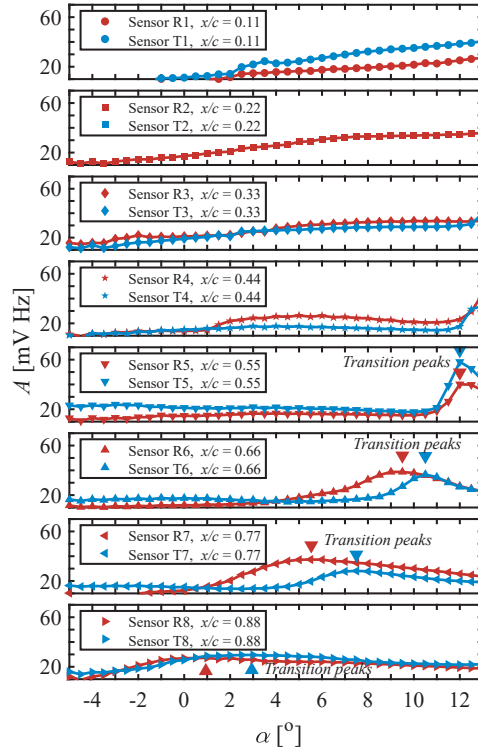


Figure 7.7: Average amplitudes, A , versus the angle of attack, α , for different sensor positions in segment 2 (R sensors) and segment 5 (T sensors), without morphing the wing ($\delta = 0$ mm).

which in turn is a driving force to trip the flow to become turbulent.

7.2.3. THE DATABASE

The obtained amplitude of each sensor, such as the ones shown in Fig. 7.7, can act as unique state variables of the boundary layer surrounding it. For instance, if we would measure an amplitude of nearly 40 mV/Hz using sensor T6, we know we have to be measuring near an angle of attack of 10.5° , and we know transition has to be positioned at the location of this sensor. On the other hand, if we would measure 15 mV/Hz using sensor T6, the angle of attack can still range between -5° and 8° , and hence multiple solutions can be true. However, when we consider a second sensor within the same segment, the number of possible solutions is reduced. If we consider all eight sensors within the same segments simultaneously, it is possible to extract the correct angle of attack, provided the database is properly filled. The data of Fig. 7.7 only considers zero morphing conditions. Upon morphing the wing, the peaks of Fig. 7.7 will shift to other angles and their maximum value can also change, and thus even more solutions present itself. However, we found that when considering all eight sensors per instrumented

segment simultaneously it is possible to extract both the correct angle of attack and morphing deflection. The location of transition is a function of these two values, and therefore can be extracted as well. In order to accurately do this, one would require a detailed database filled with data for many angles of attack and degrees of morphing deflection. This will therefore be the first step of the experimental program.

Once such a database is realized, it can be used to determine the change in the location of transition due to asynchronous morphing cases involving one or multiple segments in various patterns. In this case, the found values of the angle of attack and morphing deflection can be better defined as the local or fitted values, α_{fit} and δ_{fit} , as the sensing segment likely experiences a different angle of attack and morphing deflection as the imposed ones. To obtain α_{fit} and δ_{fit} , the following procedure is used:

1. The absolute difference of the amplitudes is calculated between the new measurement and the database. This is done per sensor and for all possible combinations of angle of attack and morphing deflection recorded in the database. So for example, the newly measured amplitude of sensor T1 is compared to all T1 amplitudes in the database. The found absolute difference, ΔA , as a function of the sensor, α and δ , can be calculated as follows:

$$\Delta A(sensor, \alpha, \delta) = |A(sensor) - A_d(sensor, \alpha, \delta)| \quad (7.1)$$

In here, A is the amplitude of the new measurement while A_d is the amplitude in the database. The output ΔA becomes a three dimensional matrix with the same dimensions as the database, being the sensor number, α and δ .

2. The total difference per sensing segment is calculated per angle of attack and morphing deflection, adding up the ΔA of all eight sensors within the same sensing segment. The found total difference, ΔA_{tot} , can be calculated as follows:

$$\Delta A_{tot}(segment, \alpha, \delta) = \sum_{sensor=1}^8 \Delta A(sensor, \alpha, \delta) \quad (7.2)$$

The outcome is again a three dimensional matrix, with the sensor dimension being replaced by the segment dimension.

3. The best fit is found by finding the minimum value within the ΔA_{tot} matrix. This is performed for each segment separately. The found angle of attack, α_{fit} , and found morphing deflection, δ_{fit} , are obtained as follows:

$$[\alpha_{fit}(segment), \delta_{fit}(segment)] = \min(\Delta A_{tot}(segment, \alpha, \delta)) \quad (7.3)$$

The obtained parameters, α_{fit} and δ_{fit} , represent the angle of attack and morphing deflection the sensing segment physically experiences.

4. During synchronous morphing α_{fit} and δ_{fit} should match the real and imposed values of α and δ , as the new measurements are duplicates of the settings used to fill the database. However, during asynchronous morphing, they most likely will not. The mismatch between them actually provides information about the effect

of asynchronous morphing on the sensing segment. We can therefore define shifts in angle of attack and morphing deflection, α_{shift} and δ_{shift} , as follows:

$$\alpha_{shift} = \alpha_{fit} - \alpha \quad (7.4)$$

$$\delta_{shift} = \delta_{fit} - \delta \quad (7.5)$$

In here, α and δ are the angle of attack and morphing deflection used as measurement condition, specifically of the sensing segment. It is expected that morphing a segment adjacent to the sensing segment will have a bigger impact on δ_{fit} compared to α_{fit} . We therefore expect that α_{shift} will stay relatively low while δ_{shift} could show significant values.

7.2.4. EXPERIMENTAL PROGRAM

For the experiments reported here, the tunnel was operating at 19.1 ms^{-1} , corresponding to a Reynolds number of 632×10^3 . The Reynolds number was calculated using a kinematic viscosity, ν , of $1.5111 \times 10^{-5} \text{ m}^2 \text{ s}^{-1}$, and a characteristic length, L , of 0.5 m, equal to the chord length of the wing.

First, a complete dataset of measurements was gathered using all sixteen piezoelectric sensors installed in the wing, varying the angle of attack and synchronous morphing deflection (i.e. all six segments were given the same deflection). These measurements are used to build the database and to locate transition on the wing. During each measurement the angle of attack and morphing deflection were kept constant, while all sixteen sensors measured simultaneously during a 10 s duration. The angle of attack was varied from -5° to 13° in 0.5° increments, yielding 37 measurement points. The synchronous morphing deflection was varied from -15 mm to $+15 \text{ mm}$ in 5 mm increments, yielding 7 measurement points. All possible combinations of angle of attack and morphing deflection were structurally measured, yielding 259 measurement points in total. To ensure reproducibility and prevent system drift, the first measurement was repeated halfway through the list of measurements and once again at the end. Nearly identical results were obtained during these three measurements, with a deviation less than 2%. Only the first of these three measurements was used to fill the dataset.

Secondly, measurements were performed using asynchronous morphing (i.e. each segment was morphed individually and not all segments had the same deflection). During each measurement the angles of attack and morphing deflections were maintained for a period of 10 s while all sixteen sensors were read out. The measurements were performed at three angles of attack of 3° , 7° and 11° . Asynchronous morphing deflection patterns as reported in Table 7.1 were imposed. The numbers shown in the table indicate the segment numbers which were given a deflection of $\delta = -15 \text{ mm}$. The adjacent segments to the actuated segments were left unactuated ($\delta = 0 \text{ mm}$), while all other segments were deflected in opposite direction ($\delta = +15 \text{ mm}$). For instance, double segment setting 45 means that segments 4 and 5 have a deflection of $\delta = -15 \text{ mm}$, while the adjacent segments (3 and 6) are kept at $\delta = 0 \text{ mm}$ and all other segments (1 and 2) are actuated to $\delta = +15 \text{ mm}$. To have the same number of segments morphing up and

down per set of asynchronous settings, segment 1 and 6 were considered to be adjacent to each other.

Table 7.1: Overview of asynchronous morphing settings, where the numbers indicate the segments morphing up, while adjacent segments do not morph and all other segments are morphed down.

Single segment setting	Double segment setting	Triple segment setting	Quadruple segment setting	Quintuple segment setting
1	12	123	1234	12345
2	23	234	2345	23456
3	34	345	3456	13456
4	45	456	1456	12456
5	56	156	1256	12356
6	16	126	1236	12346

7.3. RESULTS & DISCUSSION

This section discusses the detection of transition under zero morphing conditions (7.3.1), the detection while morphing all segments of the wing equally (7.3.2) and presents the assessment of the effects of asynchronous morphing (7.3.3).

7

7.3.1. TRANSITION UNDER ZERO MORPHING CONDITIONS

The location of transition of the SmartX wing under zero morphing conditions can directly be extracted from Fig. 7.7. The results are shown in Fig. 7.8 as a function of angle of attack for both segment 2 and 5. The figure also includes predicted transition positions using XFLR5, which is an airfoil analysis tool based on Xfoil [103, 149]. In these calculations a NACA 6510 profile was selected with matching dimensions to the unmorphed SmartX wing. To obtain the separate transition locations of segment 2 and 5, corresponding y -coordinates of 0.45 m (segment 2) and 1.35 m (segment 5) were used.

First, we address the difference between the data of segment 2 and segment 5. Both the experimental data and the XFLR5 predictions agree that transition occurs closer to the TE in segment 2 compared to segment 5. This can be explained by considering the development of the adverse pressure gradient on the suction side of the wing. The higher the adverse pressure gradient, the more they amplify instabilities in the flow and thus generate turbulence. Therefore, a higher adverse pressure gradient moves transition towards the LE. The adverse pressure gradient is not constant along the span of a finite wing. Near the tip of the wing, a strong effect of the tip vortex plays a role. Such a tip vortex occurs due to the overpressure on the pressure side of the wing to leak towards the suction side of the wing. This movement of air causes the effective angle of attack near the tip of the wing to be lower compared to the actual angle of attack [150].

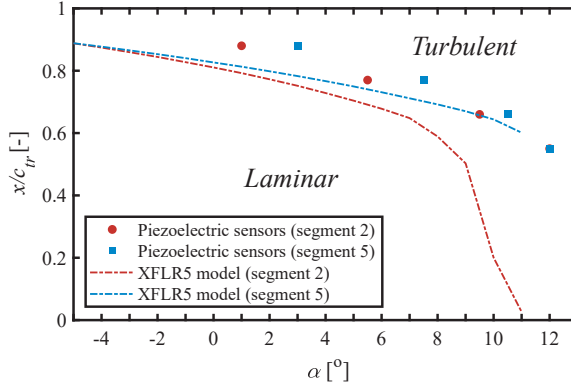


Figure 7.8: Location of transition, x/c_{tr} , versus angle of attack, α , without morphing the wing ($\delta = 0$ mm). The dash-dot lines represent the XFLR5 modelled data.

A lower angle of attack generally creates a smaller adverse pressure gradient, and thus moves transition towards the TE.

Second, the experimental data shows transition to be closer towards the TE compared to the XFLR5 predictions. One possible explanation for this is the imperfect wing-wall interface at the root of the wing, which was there because of various cables coming out of the wing preventing us to realize a perfect walled interface. This can cause a (small) tip vortex to occur on the side of the root as well, lowering the effective angle of attack, which in turn pushes transition downstream. Another reason for the difference between experimental data and the XFLR5 model could be that the SmartX wing does not resemble a perfect NACA 6510 profile due to a possible slight offset of the camber morphing TE.

7

7.3.2. TRANSITION SHIFTING DURING SYNCHRONOUS MORPHING

Using the procedure explained in the previous section, the location of transition as a function of angle of attack and the degree of morphing deflection (using seven deflection levels) for synchronous morphing (i.e. all segments are deflected equally) was determined. As described in the experimental section, the TE camber morphing part of the wing extends up to about 20% of the chord length. The results are shown in Fig. 7.9, for the measurements performed on segment 2 (Fig. 7.9a) and segment 5 (Fig. 7.9b). The lines connecting the data points are constructed by edge smoothing the linear fit lines between the data points.

From the figure it can be seen that a significant shift in the location of transition can be achieved by morphing the wing (up to about 20%). Both figures show the same general trend: increasing the morphing deflection (i.e. increasing lift) moves transition downstream towards the TE, up to an angle of attack of about 11°. This trend can again be explained considering the development of the adverse pressure gradient, with two

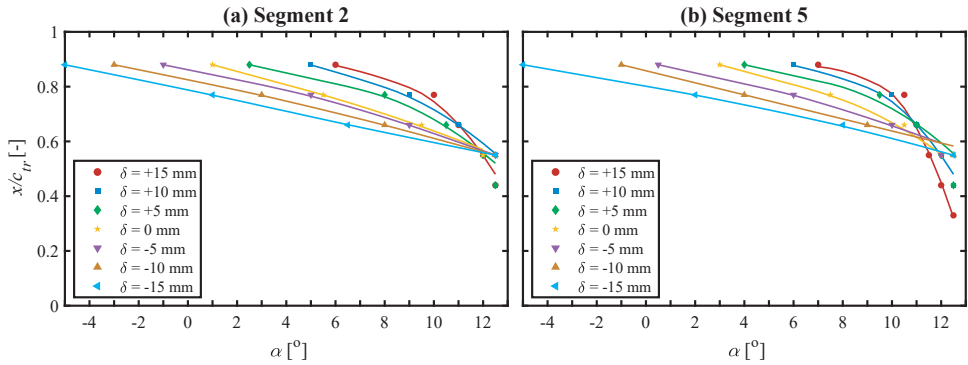


Figure 7.9: Location of transition, x/c_{tr} , versus the angle of attack, α , and synchronous morphing setting, δ , given for the sensors located in (a) segment 2 and (b) segment 5.

counteractive factors influencing it. First, by increasing α and/or δ , lift is increased, and directly with it, the adverse pressure gradient increases. This in turn will move transition upstream towards the LE. Second, while the increase of α and/or δ increases lift, so does the magnitude of the tip vortex. As described before, this inversely influences the adverse pressure gradient by lowering the effective angle of attack, and thus moves transition downstream towards the TE. One major difference between increasing α and δ is the development of the pressure distribution over the chord length. By increasing α the pressure distribution is affected over the whole chord length, while by increasing δ it mostly affects the pressure distribution in the vicinity of the morphing portion of the chord, which in case of the SmartX wing is about the last 20% of the chord. This means that the direct change of the adverse pressure gradient is more strongly affected by changing α in comparison to changing δ . In the end it seems from the figure that in most cases for a change in α the direct effect on the adverse pressure gradient is dominant, while by changing δ the inverse effect, due to the tip vortex, is dominant. Only at angles of attack higher than about 11° the trends get reversed.

All sensor amplitudes used to construct Fig. 7.9 are transferred to the database. This database then contains the amplitudes of all sensors at all combinations of α and δ and contains 4414 entries; 16 (number of sensors) by 7 (number of morphing deflections) by 37 (number of angles of attack).

7.3.3. TRANSITION DURING ASYNCHRONOUS SPANWISE MORPHING

The obtained values of α_{shift} and δ_{shift} for all asynchronous morphing cases are shown in Fig. 7.10. They show the difference between the actual imposed values of α and δ of the instrumented segment, and the α_{fit} and δ_{fit} found as closest match in the database. The number at the x -axis presents the segment numbers which are morphed up ($\delta = -15$ mm), while adjacent segments are not morphed ($\delta = 0$ mm) and all other segments are morphed down ($\delta = +15$ mm). Segment 1 is the segment at the root while segment 6 is the segment at the tip, and these two segments are considered to be adjacent to each

other.

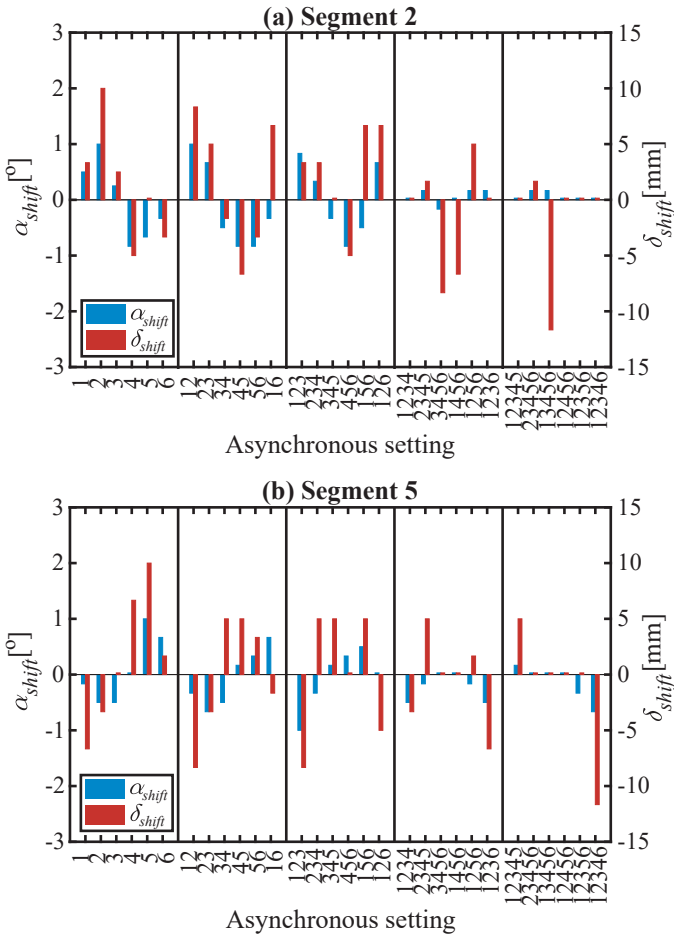


Figure 7.10: Angle of attack and morphing deflection shift, α_{shift} and δ_{shift} , versus asynchronous morphing setting, given for the sensors located in (a) segment 2 and (b) segment 5.

In almost all cases, α_{shift} stays within 1° . This shows the accuracy of the fingerprint of the sensor amplitudes, which most strongly relate the angle of attack. As expected, the value of δ_{shift} extends to relatively large numbers, generally having an offset of about 5 - 10 mm and sometimes even larger. These values basically quantify the difference between the actual asynchronous measured case and the case if all segments would have the morphing configuration of the sensing segment. This definition is easier explained considering the quintuple settings (i.e. right most settings) of Fig. 7.10a. The δ_{shift} of settings 12345 is small because it depicts the difference between setting 12345 and the case where all segments would have the condition of the sensing segment, i.e. all have the setting of segment 2. This is already almost the case (only segment 6 is

missing), and thus the shift value is low. Here, these low values of α_{shift} and δ_{shift} of the quintuple measurements show the repeatability of the sensor amplitudes, since the quintuple conditions are nearly identical to the synchronous morphing cases, with only a couple of exceptions. One of these exceptions is setting 13456 measured by segment 2, depicting a large δ_{shift} . Here the difference is shown between setting 13456 and the case where all segments would have the condition of segment 2. In this case, none of the segments have that condition, and thus the shift value is large.

Because of the definition of α_{shift} and δ_{shift} , the sign shows whether the sensing segment experiences a higher or lower α and δ as expected due to asynchronous morphing. For instance considering the single settings (i.e. left most settings) of segment 2, setting 2 shows a large positive δ_{shift} . Using this setting, the sensing segment (i.e. segment 2) has deflection $\delta = -15$ mm. The large positive δ_{shift} signifies that it actually experiences something closer to $\delta + \delta_{shift} = -5$ mm, which makes sense since the adjacent segments are both positioned at $\delta = 0$ mm. On the other hand, at setting 4 the sensing segment is at $\delta = 15$ mm, while the δ_{shift} is negative. This happens because one of the adjacent segments to the sensing segment, segment 3, has a morphing deflection of $\delta = 0$ mm, lowering the δ experienced by segment 2. It can also be seen that δ_{shift} of setting 5 is nearly zero. This makes sense, because at setting 5 segments 1, 2 and 3 are all in the same morphing position. While not all cases show such a perfect example as the once discussed in this paragraph, in general the same trends apply.

It is clear from Fig. 7.10 that in a lot of cases there is a significant shift. This means that in those cases the α , but mainly the δ , experienced by the sensing segment is affected by morphing segments other than the sensing segment itself. However, this does not necessarily affect the location of transition, as a positive α_{shift} could counteract the effect of a positive δ_{shift} .

In order to locate transition, the sensing segment is considered to be isolated, while α_{fit} and δ_{fit} act on it. In that case, Fig. 7.9 can be consulted in order to find the location of transition, using α_{fit} and δ_{fit} . The results are shown in Fig. 7.11 through Fig. 7.15 for four different asynchronous morphing patterns. Each figure shows an example picture of the wing underneath it depicting one of the settings for clarity. The gray dashed lines are the upper and lower limits of the location of transition which are found while morphing all segments synchronously to the most upward and most downward positions (see Fig. 7.9).

Starting at Fig. 7.11a, representing the sensors in segment 2, the actual data corresponds nicely to the expected behavior. The morphing settings can be divided into three groups, being setting 2, setting 4/5/6 and setting 1/3. The first is while morphing segment 2, in which case the segment the sensors are at (also segment 2) is morphed up, causing transition to be closest to the LE. The second is while morphing segment 4, 5 or 6, in which case the segment the sensors are at is morphed down, causing transition to be closest to the TE. The third is while morphing segment 1 or 3, in which case the instrumented segment is not morphed. In this case transition lies somewhere in between.

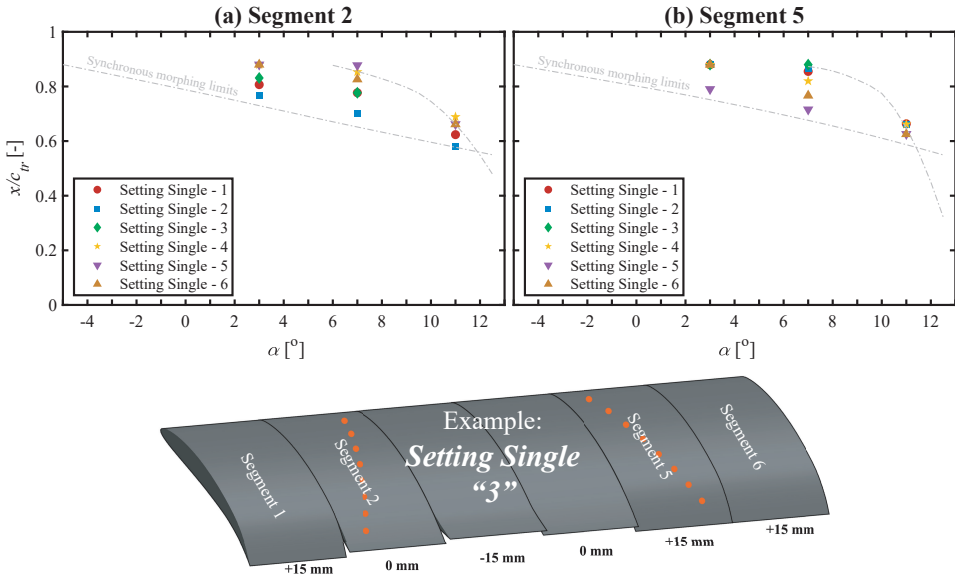


Figure 7.11: Location of transition, x/c_{tr} , versus the angle of attack, α , while morphing one segment up, given for the sensors located in (a) segment 2 and (b) segment 5.

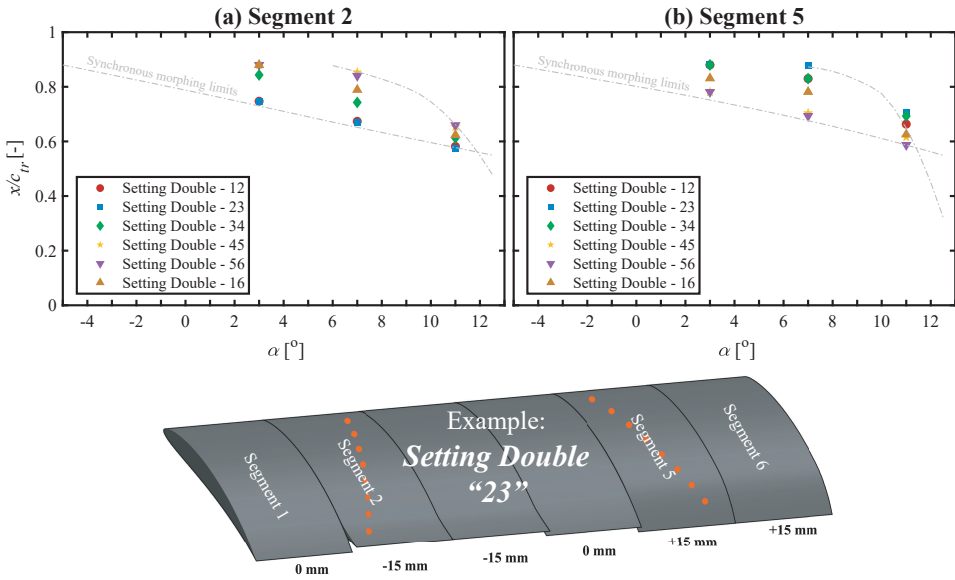


Figure 7.12: Location of transition, x/c_{tr} , versus the angle of attack, α , while morphing two segments up, given for the sensors located in (a) segment 2 and (b) segment 5.

This figure (Fig. 7.11a) therefore actually shows that in this case there is barely any effect of the adjacent segment morphing condition on the location of transition. A similar

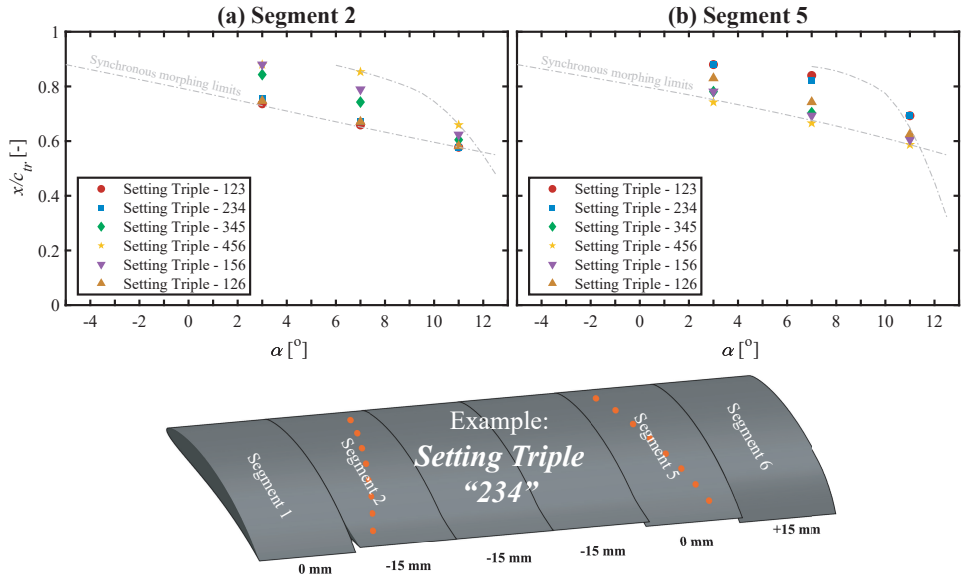


Figure 7.13: Location of transition, x/c_{tr} , versus the angle of attack, α , while morphing three segments up, given for the sensors located in (a) segment 2 and (b) segment 5.

7

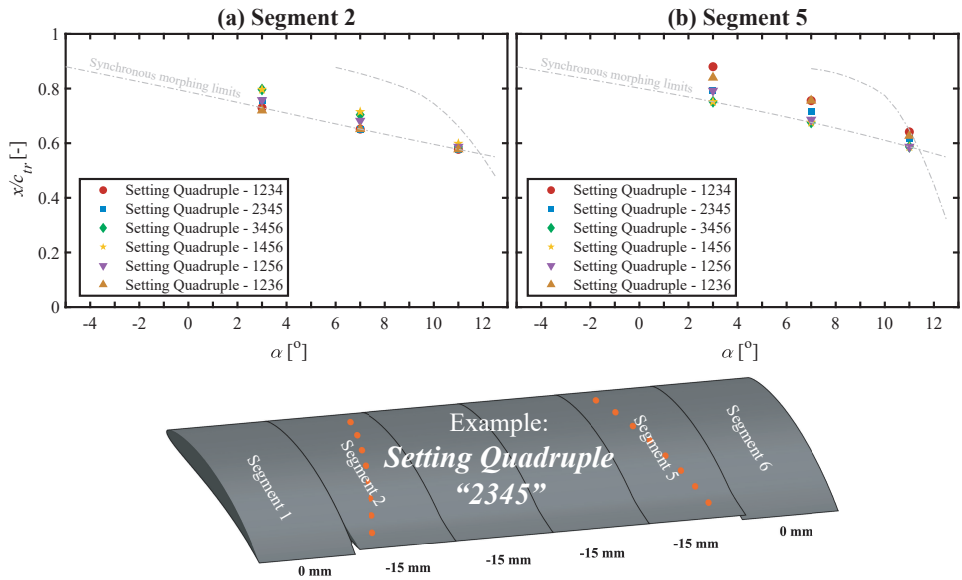


Figure 7.14: Location of transition, x/c_{tr} , versus the angle of attack, α , while morphing four segments up, given for the sensors located in (a) segment 2 and (b) segment 5.

comparison can be made using Fig. 7.13a, as the triple segment morphing is essentially the opposite of the single segment morphing. Here setting 456 means that those seg-

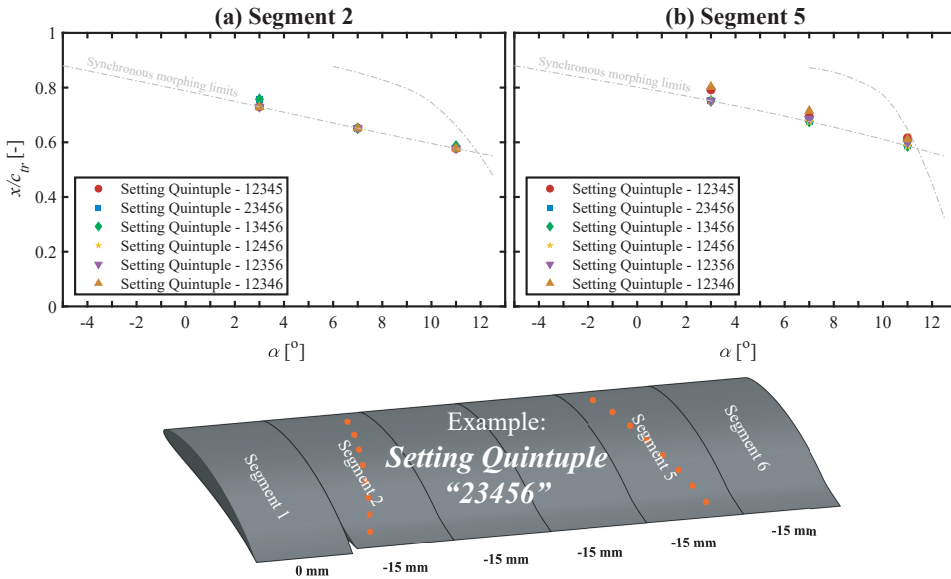


Figure 7.15: Location of transition, x/c_{tr} , versus the angle of attack, α , while morphing five segments up, given for the sensors located in (a) segment 2 and (b) segment 5.

ments are morphed up, while segment 2 is morphed down, and segment 1 and 3 are not morphed. This setting therefore pushes transition closest to the TE. On the other hand setting 123, 234, and 126 (all having segment 2 morphed down) all cause transition to be equally close to the LE. Again, the other settings have a behavior in between. In a similar way the data shown in Fig. 7.12a, Fig. 7.14a and Fig. 7.15a can be explained, all leading to the same conclusion: the location of transition detected on segment 2 mainly depends on the morphing setting of the segment itself, and seems nearly unaffected by adjacent segment morphing.

While the data for segment 5 (the near-tip segment) at first glance look similar to those of segment 2 (the near-root segment), closer inspection shows that there are some interesting differences. For instance in Fig. 7.11b it is expected that setting 4 and 6 result in similar transition locations. However, setting 4 seems to cause a transition location similar to those caused by setting 1, 2 and 3. In addition, from Fig. 7.13b it can be seen that setting 456 results in a different transition location compared to setting 345 or 156. In all three cases segment 5 is morphed down, but if also segments 4 and 6 morph down together with it (i.e. setting 456) the location of transition moves even closer to the LE compared to the other two settings. It seems that the adjacent segment morphing conditions for segment 5 do play a (minor) role.

One major difference between the sensors located in segment 2 and segment 5 is the magnitude of the effect that the tip vortex has on the local boundary layer. This effect is expected to be stronger near the tip, and thus stronger experienced by segment 5.

We stated earlier that increasing lift due to morphing actually moves transition towards the TE (for angles of attack up to about 11°) due to the increasing strength of the tip vortex. It is to be expected that segment 6 has the highest impact on the strength of the tip vortex, and thus morphing segment 6 should result in a larger transition location shift measured by segment 5 compared to morphing the other adjacent segment (segment 4).

Considering Fig. 7.12b, a couple of things can be compared. First considering setting 45 and 56, where in both cases the segment 5 is morphed up together with one of the adjacent segments. If segment 6 indeed has a bigger impact on the tip vortex, setting 56 should decrease the strength of the tip vortex more and thus move transition more towards the LE. Only a small difference between settings 45 and 56 is observed, but it happens to follow the expected trend. Similarly we can compare setting 12 and 23. With setting 12 segments 45 are morphed down while setting 23 morphs segments 56 down. Deflecting down increases lift, and thus moves transition towards the TE. As expected, line 23 indeed lies closer to the TE compared to line 12, and thus again the expected trend is followed by the measurements.

In a similar way setting 126 and 234 from Fig. 7.13b can be compared. Both settings keep segment 5 at the neutral position, but setting 234 clearly causes transition to be closer to the TE compare to setting 126. This happens again because segment 6 is morphed up (setting 126) which weakens the tip vortex and moves transition towards the LE. The same is observed comparing setting 1234 and 1236 of Fig. 7.14b, where setting 1234 causes transition to be closer to the TE compared to setting 1236. The difference in the location of transition between these settings is smaller because not any of the segments reach $\delta = +15$ mm, but are kept at $\delta = 0$ mm instead. Finally, also Fig. 7.15b shows the same trend. Here a comparison between settings 12345 and 12356 should be made, with the transition location of setting 12345 being closer to the TE because using this setting segment 6 is kept at $\delta = 0$ mm. It is also seen that setting 12346 is even closer to the TE, meaning that the effect on the location of transition is still most strongly affected by morphing segment 5 itself.

Summarizing; the data shows that the location of transition in sensor segment 2 is barely affected by adjacent segment morphing. This is however not the case for sensor segment 5, positioned near to the tip of the wing. Here the tip vortex plays an important role on the location of transition. Therefore, in terms of transition location control, a morphing wing would benefit from having more detailed spanwise distributed morphing near the tip, while near the root of the wing a lower level of detail is sufficient.

7.4. CONCLUSIONS

A method to locate transition on a complex three dimensional multi-segmental trailing edge camber morphing wing is presented. Only sixteen sensors were installed in the top skin of the morphing wing from which the signal amplitudes are used as state variables. With these state variables measured under arbitrary conditions, it is possible

to determine with a high spatial resolution the location of transition as a function of angle of attack and morphing deflection at the instrumented segment. Due to the reproducibility of the sensor amplitudes in combination with suitable data processing as described in the experimental section, we show highly consistent results, even while measuring complex asynchronous morphing conditions.

Upon morphing neighboring segments to the instrumented segment, it is found that the location of transition is barely affected near the root of the wing while a significant effect is observed near the tip. This behavior occurs due to the effect of the tip vortex, having more influence on the tip than the root of the wing. With this it can be concluded that laminar morphing wings, which are morphing wings meant to push transition towards the trailing edge for drag optimization, would benefit from having more spanwise distributed morphing segments near the tip, while a lower amount is sufficient near the root.

In the present work, the time used to measure the location of transition is set to 10 s, which was more than sufficient to obtain a strong signal-to-noise ratio. However, in order to use such a system in closed-loop control, the measurement time has to be reduced and the possibility of a sliding measurement window has to be investigated. Furthermore, parallel lift and drag measurements should be conducted to show the lift-to-drag ratio benefits such a system can provide.



8

CONCLUSIONS AND RECOMMENDATIONS

In the introduction of this thesis the main research goal was set to develop a functional piezoelectric sensor capable of measuring local flow conditions in the boundary layer of the SmartX morphing wing. This was translated into three sub-goals:

- Investigate the potential to increase the sensitivity of piezoelectric sensor materials and prevent the reliance on lead-based systems (*Chapter 2* and *Chapter 3*).
- Develop a sensor capable of measuring flow phenomena which can be installed within a wing (*Chapter 4* and *Chapter 5*).
- Realize a network of sensors to be installed in the SmartX wing and demonstrate their potential of analyzing the boundary layer under complex morphing patterns (*Chapter 6* and *Chapter 7*).

This chapter finalizes the thesis by reflecting on these three sub-goals, and focuses on possible future steps to further develop the piezoelectric sensor system.

8.1. CONCLUSIONS

Chapters 2 and 3 investigate the first sub-goal: investigate the potential to increase the sensitivity of piezoelectric sensor materials and prevent the reliance on lead-based systems. They describe the fabrication of piezoelectric composites which have the benefit of an increased sensor sensitivity, g_{33} , while also being lead-free. One could conclude that the first sub-goal was completed with success, and that piezoelectric composites indeed offer good alternatives for piezoelectric ceramics for sensor (and energy harvesting) applications. However, in Chapter 4 we encounter some intrinsic problems with the composite sensors; here we found that their sensitivity is actually lower compared to that of commercially available PZT ceramics. Although their g_{33} is higher, a problem occurs due to their low capacitance. This causes large losses in

the electronic circuitry behind the sensor, lowering the overall sensitivity. Since the g_{33} is the generally accepted figure of merit for piezoelectric sensors, this problem was not identified in earlier studies. A way to deal with this could have been by using high volume fraction composites, which generally have a somewhat lower g_{33} but also a higher capacitance, ideally making the overall sensor output better. The appendix of Chapter 5 shows a comparison between a PZT ceramic sensor and such a high volume fraction composite sensor. While using identical boundary conditions and dimensions, the amplitude of the composite sensor nearly reaches 75% of the amplitude of the PZT ceramic sensor. This result shows that in the current application composite sensors are likely able to measure the same phenomena as the PZT sensors. However, to make the composite approach work in general, a balance should be found between the nominal figure of merit, g_{33} , and the material capacitance. This is easier said than done, as these two variables are dependent on each other through Equation 1.3.

Chapters 4 and 5 address the second sub-goal: develop a sensor capable of measuring flow phenomena which can be installed within a wing. Chapter 4 describes the use of a piezoelectric patch, which can simply be applied to the top skin of a wing. However, after analyzing the wind tunnel experiments it was concluded that the sensitivity is not high enough to measure vibrations induced by the flow, and that the mechanical coupling between the piezoelectric materials and wing skin is too strong, causing large wing vibration signals not related to the boundary layer. However, we were still able to locate transition using the patch containing sensors based on PZT through the pyroelectric effect. These pyroelectric sensor signals are weak and ambient temperature fluctuations can easily disturb the signal. This therefore required an alternative route to increase the sensitivity, limit the mechanical coupling between the wing skin and piezoelectric material and limit the pyroelectric contribution of the sensor material. This was done by developing the piezoelectric bimorph setup shown in Chapter 5. Here, a sensor is built into the wing with a vane piercing through the skin to mechanically couple the piezoelectric bimorph to the boundary layer on top of the airfoil. A clear relation is found between the piezoelectric sensor measurements and the state of the boundary layer, confirmed by PIV measurements. With this validation of the signal processing method, we demonstrated to have successfully developed a sensor system which is able to locally determine the state of the boundary layer.

Chapters 6 and 7 address the third sub-goal: realize a network of sensors to be installed in the SmartX wing and demonstrate their potential of analyzing the boundary layer under complex morphing patterns. While Chapter 6 provides an overview of the design concepts behind and the technologies integrated in the SmartX wing, Chapter 7 describes the experiments used to locate transition on the wing. Using the sensors, we were able to directly detect transition while morphing all segments of the wing equally. From this we concluded that transition moves towards the trailing edge by increasing the morphing deflection (i.e. increasing curvature) of the wing. While this seems counterintuitive, this behavior occurs because the tip vortex strength increases with increasing morphing deflection, lowering the effective angle of attack. This effect also causes the location of transition to always be slightly closer to the trailing edge in

the near-tip segment compared to the near-root segment. This is because the near-tip segment experiences the tip vortex more intensely. Finally, by treating the suitably integrated amplitude of individual sensors as state variables, it is possible to assess what happens with the location of transition upon morphing segments individually. Here it is concluded that while the boundary layer is clearly being affected by morphing neighboring segments, this does not always result in a different location of transition. We found that the location of transition of the near-root segment is barely affected by morphing neighboring segments, while a significant effect is found at the near-tip segment. Again the effect of the tip vortex plays an important role for why this happens. This leads to the conclusion that, in terms of transition location control, morphing wings would generally benefit from having more spanwise distributed morphing segments near the tip of the wing, while a lower amount of segments should be sufficient near the root. In addition, the method of detecting transition developed in this chapter leads to a higher spatial resolution than the inter-sensor distance and makes it possible to assess any complicated morphing setting, as long as the values of the state variables are known for a broad range of flow conditions.

8.2. RECOMMENDATIONS FOR FUTURE WORK

The final product of this thesis has arrived at a fully working sensor system able to detect the location of transition on complex morphing wings. However, the work might be continued in the following areas to take it to the next level.

One of the next steps is to further investigate the possibility to completely move to lead-free sensors instead of the PZT ceramic sensors used in most of the studies presented in this work. In this work we investigated the possibility to use piezoelectric composites instead. From the appendix of Chapter 5 this seems like a viable option, as the amplitude of the composite sensor is in range of the one provided by the PZT sensor. By optimizing the balance between g_{33} , capacitance and electronic circuit components even better, composites might even turn out to be better sensors than PZT as the g_{33} of PZT itself is low. Other options might be the use of different lead-free piezoelectric ceramics. However, these currently suffer from having an even lower g_{33} , a limited T_c and/or are extremely moisture sensitive.

In this thesis, the dimensions of the sensor vane, bimorph and slit through which the vane pierces the skin, were all taken as fixed parameters. All of these affect the signal amplitude, the boundary layer downstream of the sensor, and geometric space required inside the wing. Further analysis of these dimensions is therefore important to optimize the resolution, stability and performance of the sensor.

Another next step for such a sensor system, regardless of the sensor material itself, would be to include it in an online control loop. This way, knowledge of the current location of transition can be used to optimize the morphing setting of the wing for transient airflow conditions. For this purpose, first the measurement time should be reduced significantly. In the present work, a typical measurement time of 10 s is being maintained simply to maximize the signal-to-noise ratio, but such a time would be too

long for a control loop. However, a preliminary test has shown that by going down to a measurement time of 0.1 s almost identical results were obtained. Determining the absolute minimum time for proper signal interpretation was not in the scope of this work.

Once an active online control loop is realized, one could use this to apply real-time drag optimization. In order to do this, accurate drag measurements have to be performed, and an algorithm should be written which uses sensor input and calculates a new morphing setting supposedly lowering the overall drag, while increasing the lift-to-drag ratio.

Finally, the environmental conditions in the wind tunnel are optimally controlled. No fluctuations in airspeed, temperature or pressure, and no rain or ice formation. These factors could all play vital roles in the signal strength and nature of the piezoelectric sensor making it hard to use a fixed protocol to detect the location of transition. Therefore, the effects environmental conditions should be determined. This especially plays an important role using short measurement times, as these are already easily affected by measurement errors.

By investigating these five topics in more detail, an environmentally friendly morphing wing which is capable of online drag optimization might be realized which can be used in ambient weather conditions.

SUMMARY

This thesis describes the development, validation and implementation of piezoelectric flow sensors. These sensors are meant to measure flow phenomena such as transition and separation in the boundary layer of an aircraft wing. Such information can be used as input variables to a control loop to push laminar-to-turbulent transition towards the trailing edge of a wing, thereby reducing the overall skin friction drag. The developed sensors are installed in the *SmartX* wing, which is a morphing wing developed at the Delft University of Technology (TUD).

In **Chapter 1** the aim and the motivation for the SmartX project are introduced. A brief literature review is presented about piezoelectric materials, piezoelectric sensors and boundary layers on airfoils. Finally, it provides an outline of the thesis work, introducing three sub-goals: (i) replacing widely used PZT ceramics with high-sensitivity lead-free composite materials, (ii) the design and validation of the new flow sensor concepts and (iii) the installation and usage of the flow sensor in the SmartX wing.

The first main part of this thesis, *Chapter 2* and *Chapter 3*, treats the first sub-goal: replacing widely used PZT ceramics with high-sensitivity lead-free composite materials.

In **Chapter 2** six piezoelectric composite materials are presented. These composites are fabricated using three piezoelectric filler materials (BT, KNLN and PZT) and two inert polymeric matrices (epoxy and PU). This chapter discusses how the matrix properties influence the piezoelectric charge constant, d_{33} , of the piezoelectric composites. Analytical models show that only the dielectric constant of the matrix affects the value of d_{33} when considering different matrix materials. However, even though the dielectric constant of epoxy and PU is nearly identical, the d_{33} of the composites fabricated using these matrices differs significantly. A missing factor of the analytical models appears to be the matrix electrical conductivity. The electrical conductivity of an epoxy matrix is larger compared to that of a PU matrix, which increases the effective electric field applied to the filler particles during poling. This in turn ensures that the filler particles in epoxy composites are better poled, and thus have a higher d_{33} . The electrical conductivity of a PU matrix can be increased through moisture absorption. This way, also the d_{33} of PU composites can be increased. The appendix of this chapter adds a third matrix material: PDMS. By fabricating a composite combining a PDMS matrix with KNLN filler particles a d_{33} is obtained which largely outperforms the predictions of analytical models. The exact reason why this is, is still unknown to date.

In **Chapter 3** one specific type of piezoelectric composite material is highlighted; a low volume fraction of dielectrophoretically aligned KNLN short fibers embedded in a PDMS matrix. Aligning the filler particles results in a significant increase of d_{33} in the

direction of alignment. The low volume fraction of filler particles keeps the dielectric constant of the composite material low. The low dielectric constant in combination with the relatively high d_{33} results in a high piezoelectric voltage constant, g_{33} , and a high efficiency constant for energy harvesters, $d_{33}g_{33}$. The highest value of $d_{33}g_{33}$ is found for composites with 6 volume percent filler particles. In this composite, the value of $d_{33}g_{33}$ is comparable to that of state-of-the-art PZT ceramics. The chapter finishes with a comparison between the 6 volume percent KNLN/PDMS composite and PZT. By applying an identical mechanical dynamical force to both materials while measuring the electrical energy stored in these materials, it is concluded that both materials indeed generate the same amount of energy. This chapter therefore proves the potential of piezoelectric composites to replace piezoelectric ceramics for energy harvesting applications.

The second main part of this thesis, *Chapter 4* and *Chapter 5*, treats the second sub-goal: the design and validation of the new flow sensor concepts.

In **Chapter 4** a patch containing eight PZT ceramic piezoelectric elements is presented. Such a patch can simply be bonded to the skin of an airfoil. However, we are not able to locate transition using this patch, possibly due to the low sensitivity of the PZT ceramics and/or due to the strong mechanical coupling between the PZT ceramics and the wing skin. Because of the latter, strong mechanical vibrations are measured which are not related to the boundary layer, which simply disturb the data and makes it even harder to read (possible) underlying boundary layer signals. However, it is possible to locate transition by means of the pyroelectric effect. The use of the pyroelectric effect is delicate as it requires a transient temperature difference between the airfoil and the incoming airflow. This increases the required measurement time and is sensitive to environmental temperature changes. Conclusions regarding the pyroelectric measurements are included in the appendix of this chapter. In addition, a patch containing eight composite piezoelectric elements is also developed and tested. Although based on Chapter 2 and Chapter 3 piezoelectric composites were expected to perform as good sensors due to their high sensitivity, they were found not to function properly in these wind tunnel experiments. This is caused by the low dielectric constant of the composite material causing large losses in the electronic circuit behind it.

In **Chapter 5** a new approach is presented to measure boundary layer states using a sensor based on a piezoelectric material. Here a piezoelectric bimorph is used in order to overcome the problems observed in *Chapter 4*, because such a bimorph can offer the following benefits: it amplifies the mechanical input energy, intrinsically cancels the pyroelectric contribution, and makes it possible to install the sensor (partially) free from the wing skin which limits the (interfering) signals measured due to vibrations of the wing. To increase the chance of success even more, it is decided to only work with PZT instead of using composite materials. A PZT bimorph is installed within an airfoil, with a vane attached to it which pierces through the airfoil skin. This vane mechanically couples the PZT bimorph to the boundary layer. It is shown that by using this method sufficient sensitivity is reached, and with it the location of transition and separation are successfully detected. The correctness of the data interpretation and handling is

confirmed using Particle Image Velocimetry (PIV) measurements. The appendix of this chapter shows a comparison between the performance of a PZT bimorph and that of a composite bimorph with identical dimensions in a laboratory setup. It is shown that by using a dedicated composite material it reaches an output voltage of about 75 % of that of the PZT bimorph. This is a good first indication that composite materials might be able to replace PZT in the current application.

The third main part of this thesis, *Chapter 6* and *Chapter 7*, treats the third sub-goal: the installation and usage of the flow sensors in the SmartX wing.

In **Chapter 6** an overview is given of the SmartX wing. It describes the integration of the various subsystems into a single wing, and provides technical details about which features the wing contains. Smart systems included in the wing are the trailing edge morphing for main actuation, fast tabs for small but fast actuation, fiber optics for strain measurements and the flow sensors from this work for boundary layer measurements. Finally, it describes the hardware and software integration for closed-loop control.

In **Chapter 7** the final wind tunnel experiments are presented, showing the potential of sixteen piezoelectric flow sensors installed on the suction side of the SmartX morphing wing. It is shown that the location of transition can be detected while morphing all six segments of the morphing wing simultaneously. By treating the suitably averaged amplitudes measured by the sensors as state variables, it is also possible to assess what happens when morphing each segment of the wing individually. From these measurements, it is concluded that the location of transition near the root of the wing is barely affected by morphing neighboring segments. However, near the tip of the wing a significant effect is observed. The effect is attributable to the tip vortex having a strong effect on the boundary layer near the tip of the wing. With this, it is concluded that laminar morphing wings, which are morphing wings with the aim to push transition towards the trailing edge, benefit from having more detailed segments near the tip of the wing, while a lower amount of segments is sufficient near the root. While in this work the sensors simply recorded data and the data analysis was done offline, these sensors are deemed promising candidates for use in an online control loop in order to actively push transition towards the trailing edge to increase the lift-to-drag ratio.

In **Chapter 8** the realization of the sub-goals which were stated in *Chapter 1* is assessed, and conclusions are drawn based on the results gathered throughout the thesis. The main conclusion is that the developed PZT based sensors are able to locate transition on the SmartX wing, even while performing complex morphing patterns. Implicitly it has been demonstrated that lead-free piezoelectric composites also can be used for this application. The chapter ends with a recommendations section, stating that possible future work can be spent on (i) the use of lead-free piezoelectric materials, (ii) optimizing the dimensions of the sensor components, (iii) using the sensors in an active control loop, (iv) adding a drag optimization algorithm and (v) investigating the use of these sensors in uncontrolled weather conditions.



SAMENVATTING

Dit proefschrift beschrijft de ontwikkeling, validatie en implementatie van piëzo-elektrische stromingsensoren. Deze sensoren zijn bedoeld om verschillende stromingsfenomenen, in het bijzonder laminair-naar-turbulent transitie, te meten aan een vliegtuigvleugel. De informatie uit deze metingen kan vervolgens gebruikt worden als invoer voor een regelkring om transitie naar de achterrand van de vleugel te verplaatsen. Hiermee kan de totale stromingsweerstand verlaagd worden. De ontwikkelde sensoren zijn vervolgens geïnstalleerd in de *SmartX* vleugel. Dit is een vervormbare (morphing) vleugel ontwikkeld aan de Technische Universiteit Delft (TUD).

In **Hoofdstuk 1** worden het doel en de motivatie voor het *SmartX* project geïntroduceerd. Het hoofdstuk geeft een korte beschrijving van zowel piëzo-elektrische materialen als grenslagen die voorkomen op vleugels. Het hoofdstuk sluit af met een overzicht van het proefschrift waarin de drie subdoelen van dit onderzoek benoemd worden: (i) het vervangen van het loodhoudende keramiek PZT door loodvrije composiet materialen met een hogere gevoeligheid, (ii) het ontwerpen en valideren van de nieuw ontwikkelde stromingssensoren en (iii) de installatie en het gebruik van de ontworpen sensoren in de *SmartX* vleugel.

Het eerste deel van het proefschrift, *Hoofdstuk 2* en *Hoofdstuk 3*, behandelt het eerste subdoel: het vervangen van het loodhoudende keramiek PZT door loodvrije composiet materialen met een hogere gevoeligheid.

In **Hoofdstuk 2** wordt de productie van zes verschillende piëzo-elektrische composiet materialen beschreven. Deze composiet materialen worden gemaakt door drie verschillende deeltjes (BT, KNLN en PZT) te combineren met twee verschillende matrix polymeren (epoxy en PU). Dit hoofdstuk laat zien hoe de eigenschappen van de matrix invloed hebben op de piëzo-elektrische ladingsconstante, d_{33} . Analytische modellen geven doorgaans alleen aan dat de diëlektrische constante van de matrix effect heeft op de waarde van d_{33} van het composiet. Het blijkt echter dat, ondanks dat de diëlektrische constante van epoxy en PU gelijk is, de d_{33} van de composieten die gemaakt zijn met deze matrixen behoorlijk verschillen. Een ontbrekende factor in de eerder genoemde analytische modellen is de elektrische geleiding van de matrix. De elektrische geleiding in een epoxy matrix is hoger dan dat van een PU matrix en daardoor stijgt het effectieve elektrische veld wat over de deeltjes staat tijdens het polariseren. Dit zorgt ervoor dat epoxy composieten beter gepolariseerd worden, en dus een hogere d_{33} hebben. De elektrische geleiding van een PU matrix kan verhoogd worden door deze vocht te laten absorberen. Op deze manier is het mogelijk om ook hier een hogere d_{33} te verkrijgen. In de bijlage van dit hoofdstuk wordt nog een derde matrix polymeer besproken, namelijk een PDMS matrix. Door deze matrix te combineren met KNLN deeltjes wordt een d_{33}

behaald die ver boven de voorspellingen van analytische modellen ligt. De exacte reden voor deze uitkomst is tot op heden niet gevonden.

In **Hoofdstuk 3** wordt één specifiek piëzo-elektrisch composiet beschreven: een composiet met een lage volumefractie KNLN korte vezels die diëlektroforetisch uitgelijnd zijn in een PDMS matrix. Het uitlijnen van de deeltjes zorgt ervoor dat de d_{33} significant wordt verhoogd in de richting van het uitlijnen. De lage volumefractie aan deeltjes zorgt ervoor dat de diëlektrische constante van het composiet laag blijft. De lage diëlektrische constante van het composiet, gecombineerd met een relatief hoge d_{33} , zorgt voor een hoge piëzo-elektrische spanningsconstante, g_{33} , en een hoge waarde voor piëzo-elektrische energieopwekking, $d_{33}g_{33}$. De hoogste $d_{33}g_{33}$ waarde wordt gevonden in composieten met 6 volumepercent deeltjes. Deze blijkt zelfs vergelijkbaar met de $d_{33}g_{33}$ van piëzo-elektrisch keramiek PZT van de hoogste kwaliteit. Het hoofdstuk sluit af met een vergelijking tussen het KNLN/PDMS composiet en PZT. Door een identieke mechanische dynamische kracht uit te oefenen op beide materialen en de opgewekte energie te meten, is vast komen te staan dat beide materialen een vergelijkbare hoeveelheid energie opwekken. Hiermee is bewezen dat piëzo-elektrische composieten loodhoudend keramiek kunnen vervangen als energieopwekkers.

Het tweede deel van het proefschrift, *Hoofdstuk 4* en *Hoofdstuk 5*, behandelt het tweede subdoel: het ontwerpen en valideren van de nieuw ontwikkelde stromingssensoren.

In **Hoofdstuk 4** wordt de ontwikkeling beschreven van een folie waarin acht PZT keramische piëzo-elektrische elementen geïntegreerd zijn. Het voordeel van het integreren van de sensoren in een folie is dat het als één geheel direct op een vleugel kan worden geplakt. Het blijkt echter niet mogelijk om de locatie van transitie te meten, mogelijk door de lage gevoeligheid van de PZT sensoren en/of door de sterke mechanische koppeling tussen de vleugel en de PZT sensoren. Door deze mechanische koppeling worden sterke signalen gemeten die niet grenslaag gerelateerd zijn, en dus mogelijke grenslaag signalen onleesbaar maken. Het blijkt wel mogelijk om transitie te meten door middel van het pyro-elektrisch effect. Deze manier van meten is niet verder onderzocht aangezien het gebruik van het pyro-elektrisch effect de minimale meettijd verhoogt en een temperatuurverschil vereist tussen de vleugel en de stroming. Een korte toelichting met betrekking tot de pyro-elektrische metingen van deze experimenten is beschreven in de bijlage van dit hoofdstuk. Naast deze patch is een tweede patch gemaakt en getest met acht piëzo-elektrische composiet materialen. Piëzo-elektrische composieten hebben doorgaans een hoge sensor gevoeligheid. Echter blijkt deze patch tijdens de windtunnelexperimenten niet te werken. Dit komt door de lage diëlektrische constante van de composieten waardoor grote elektrische verliezen optreden in het elektronisch circuit dat verbonden is aan de sensoren.

In **Hoofdstuk 5** is een nieuwe poging beschreven om transitie in de grenslaag te meten. Om de in *Hoofdstuk 4* ondervonden problemen te verhelpen, is dit keer gebruik gemaakt van een piëzo-elektrische bimorf. Het gebruik van een bimorf biedt diverse voordelen:

het verhoogt de mechanische invoerenergie, het heft het pyro-elektrisch effect op en het maakt het mogelijk om de sensor (deels) vrij van de vleugel zelf te monteren, wat de doorgegeven vibraties beperkt. Om de slagingskans te vergroten is er besloten hier alleen gebruik te maken van PZT. Een PZT bimorf is binnen in de vleugel geïnstalleerd. Op het uiteinde van de bimorf is een vaantje gemonteerd dat door een klein gaatje in de vleugel naar buiten steekt. Het vaantje verbindt zo de grenslaag met de bimorf. Met deze opstelling zijn we in staat om transitie en loslating te meten. Dit is gevalideerd met Particle Image Velocimetry (PIV) metingen. De bijlage van dit hoofdstuk presenteert een compositen bimorf. In een laboratoriumopstelling zijn beide bimorf sensoren met elkaar vergeleken en het blijkt dat de compositen bimorf ongeveer 75 % van het voltage behaalt in vergelijking met de PZT bimorf. Dit is een goede eerste indicatie dat composit materialen over enige tijd mogelijk PZT zouden kunnen vervangen in de huidige toepassing.

Het derde deel van het proefschrift, *Hoofdstuk 6* en *Hoofdstuk 7*, behandelt het derde subdoel: de installatie en het gebruik van de in *Hoofdstuk 5* ontworpen sensoren in de SmartX vleugel.

In **Hoofdstuk 6** wordt de SmartX vleugel beschreven. Het hoofdstuk beschrijft de technische details van verschillende subsystemen en hoe deze in één vleugel zijn gemonteerd. De beschreven systemen zijn de vervormende achterrand van de vleugel welke bestaat uit zes onafhankelijke segmenten als hoofdbesturing, kleine piëzo-elektrische bimorfen voor snelle subtiele actuatie, glasvezels voor vervormingsmetingen en de stromingssensoren voor grenslaagmetingen zoals beschreven in dit proefschrift. Het hoofdstuk eindigt met een beschrijving van de integratie van hardware en software voor het waar maken van een gesloten regelkring.

In **Hoofdstuk 7** worden de windtunnelexperimenten gepresenteerd die de potentie laten zien van de zestien stromingssensoren die zijn geïnstalleerd in de SmartX vleugel. De locatie van transitie op de vleugel kon worden gemeten terwijl alle zes de vormveranderende segmenten tegelijk worden bediend. Door de amplitudes die door de sensoren gemeten worden te behandelen als toestandsvariabelen, wordt het ook mogelijk om te bekijken wat er gebeurt wanneer elk segment apart wordt bediend. Hieruit blijkt dat de locatie van transitie bij de wortel van de vleugel amper wordt beïnvloed door het bedienen van aanliggende segmenten. Dit geldt echter niet voor het uiteinde van de vleugel waar wel degelijk een effect op de locatie van transitie wordt gevonden. Dit effect komt door de tipwervel, die een sterk effect heeft op de grenslaag bij het uiteinde van de vleugel. Op grond van deze resultaten wordt geconcludeerd dat een laminaire vervormbare vleugel, dat wil zeggen een vleugel met als doel om transitie naar de achterrand te verplaatsen, baat heeft bij een fijnere verdeling van bedieningspanelen bij het uiteinde van de vleugel, terwijl een grovere verdeling bij de wortel genoeg is. Hoewel de sensoren in dit hoofdstuk enkel gebruikt worden om data te verzamelen en de data verwerking na afloop van het experiment offline gebeurde, zijn deze sensoren veelbelovend voor gebruik in een online regelkring met als doel om transitie naar de achterrand van de vleugel te verplaatsen en daarmee de stromingsweerstand te verlagen.

In **Hoofdstuk 8** wordt een samenvatting gegeven van de resultaten van het onderzoek naar de drie subdoelen en worden de resultaten bij elkaar gebracht. De hoofdconclusie is dat de ontwikkelde sensoren in staat zijn om transitie te meten aan de SmartX vleugel, ook als complexe vervormingspatronen toegepast worden. Verder is indirect de potentie van loodvrije composieten voor gebruik in deze applicatie aangetoond. Dit hoofdstuk sluit af met enige aanbevelingen. Hier wordt aangegeven dat toekomstig onderzoek uitgevoerd zou moeten worden aan (i) de overstap naar volledig loodvrij piëzo-elektrische materialen, (ii) het optimaliseren van de afmetingen van de diverse componenten van de sensor, (iii) het gebruik van de ontwikkelde sensoren in een online regelkring, (iv) het toevoegen van een wrijvingsweerstandminimalisatiealgoritme en (v) het gebruik van deze sensoren in variabele weersomstandigheden.

REFERENCES

- [1] C. Thill, J. Etches, I. Bond, K. Potter, and P. Weaver, "Morphing skins," *The Aeronautical Journal*, vol. 112, pp. 117–139, 2008.
- [2] J. Sun, Q. Guan, Y. Liu, and J. Leng, "Morphing aircraft based on smart materials and structures: A state-of-the-art review," *Journal of Intelligent Material Systems and Structures*, vol. 27, no. 17, pp. 2289–2312, 2016.
- [3] S. Barbarino, O. Bilgen, R. M. Ajaj, M. I. Friswell, and D. J. Inman, "A review of morphing aircraft," *Journal of Intelligent Material Systems and Structures*, vol. 22, no. 9, pp. 823–877, 2011.
- [4] X. Lachenal, S. Daynes, and P. M. Weaver, "Review of morphing concepts and materials for wind turbine blade applications," *Wind Energy*, vol. 16, pp. 283–307, 2013.
- [5] R. De Breuker, T. Mkhoyan, N. Nazeer, V. L. Stuber, R. M. Groves, S. van der Zwaag, and J. Sodja, "Overview of the SmartX wing technology integrator," *Submitted to AIAA Journal*, 2021.
- [6] H. Elahi, K. Munir, M. Eugeni, M. Abrar, A. Khan, A. Arshad, and P. Gaudenzi, "A Review on Applications of Piezoelectric Materials in Aerospace Industry," *Integrated Ferroelectrics*, vol. 211, no. 1, pp. 25–44, 2020.
- [7] X. Qing, W. Li, Y. Wang, and H. Sun, "Piezoelectric transducer-based structural health monitoring for aircraft applications," *Sensors (Switzerland)*, vol. 19, no. 3, p. 545, 2019.
- [8] D. Li, Y. Wu, A. Da Ronch, and J. Xiang, "Energy harvesting by means of flow-induced vibrations on aerospace vehicles," *Progress in Aerospace Sciences*, vol. 86, pp. 28–62, 2016.
- [9] J. Holterman and P. Groen, *An introduction to piezoelectric materials and applications*. Stichting Applied Piezo, Apeldoorn, the Netherlands, 2013.
- [10] S. B. Lang, "Pyroelectricity: From ancient curiosity to modern imaging tool," *Physics Today*, vol. 58, pp. 31–36, 2005.
- [11] D. B. Deutz, *Flexible piezoelectric composites*. PhD thesis, Delft University of Technology, Delft, the Netherlands, 2017.
- [12] "An american national standard IEEE standard definitions of terms associated with ferroelectric and related materials," *IEEE Transactions on Ultrasonics, Ferroelectrics and Frequency Control*, vol. 50, no. 12, pp. 1–32, 2003.

- [13] J. Valasek, "Piezo-electric and allied phenomena in Rochelle salt," *Physical Review*, vol. 17, no. 4, pp. 475–481, 1921.
- [14] E. Sawaguchi, G. Shirane, and Y. Takagi, "Phase transition in lead zirconate," *Journal of the Physical Society of Japan*, vol. 6, pp. 333–339, 1951.
- [15] B. Jaffe, *Piezoelectric transducers using lead titanate and lead zirconate*. U.S. Patent 2708244 A, May 10, 1955.
- [16] R. Guo, L. E. Cross, S. E. Park, B. Noheda, D. E. Cox, and G. Shirane, "Origin of the high piezoelectric response in $\text{PbZr}_{1-x}\text{Ti}_x\text{O}_3$," *Physical Review Letters*, vol. 84, no. 23, pp. 5423–5426, 2000.
- [17] B. Noheda, J. Gonzalo, L. Cross, R. Guo, and S. Park, "Tetragonal-to-monoclinic phase transition in a ferroelectric perovskite: The structure," *Physical Review B - Condensed Matter and Materials Physics*, vol. 61, no. 13, pp. 8687–8695, 2000.
- [18] M. Acosta, N. Novak, V. Rojas, S. Patel, R. Vaish, J. Koruza, G. A. Rossetti, and J. Rödel, "BaTiO₃-based piezoelectrics: Fundamentals, current status, and perspectives," *Applied Physics Reviews*, vol. 4, no. 4, p. 041305, 2017.
- [19] T. R. Shrout and S. J. Zhang, "Lead-free piezoelectric ceramics: Alternatives for PZT?," *Journal of Electroceramics*, vol. 19, no. 1, pp. 111–124, 2007.
- [20] J. Rödel, K. G. Webber, R. Dittmer, W. Jo, M. Kimura, and D. Damjanovic, "Transferring lead-free piezoelectric ceramics into application," *Journal of the European Ceramic Society*, vol. 35, no. 6, pp. 1659–1681, 2015.
- [21] P. Kumari, R. Rai, S. Sharma, M. Shandilya, and A. Tiwari, "State-of-the-art of lead free ferroelectrics: A critical review," *Advanced Materials Letters*, vol. 6, no. 6, pp. 453–484, 2015.
- [22] J. Wu, D. Xiao, and J. Zhu, "Potassium-sodium niobate lead-free piezoelectric materials: Past, present, and future of phase boundaries," *Chemical Reviews*, vol. 115, no. 7, pp. 2559–2595, 2015.
- [23] Y. Saito, H. Takao, T. Tani, T. Nonoyama, K. Takatori, T. Homma, T. Nagaya, and M. Nakamura, "Lead-free piezoceramics," *Nature*, vol. 432, pp. 84–87, 2004.
- [24] J. F. Li, K. Wang, F. Y. Zhu, L. Q. Cheng, and F. Z. Yao, "(K, Na)NbO₃-based lead-free piezoceramics: Fundamental aspects, processing technologies, and remaining challenges," *Journal of the American Ceramic Society*, vol. 96, no. 12, pp. 3677–3696, 2013.
- [25] Y. Saito and H. Takao, "High Performance Lead-free Piezoelectric Ceramics in the (K,Na)NbO₃-LiTaO₃ Solid Solution System," *Ferroelectrics*, vol. 338, no. 1, pp. 17–32, 2006.
- [26] H. Kawai, "The Piezoelectricity of Poly (vinylidene Fluoride)," *Japan. J. Appl. Phys.*, vol. 8, pp. 975–976, 1969.

- [27] T. Furukawa, "Piezoelectricity and Pyroelectricity in Polymers," *IEEE Transactions on Electrical Insulation*, vol. 24, no. 3, pp. 375–394, 1989.
- [28] I. Katsouras, K. Asadi, M. Li, T. B. Van Driel, K. S. Kjær, D. Zhao, T. Lenz, Y. Gu, P. W. Blom, D. Damjanovic, M. M. Nielsen, and D. M. De Leeuw, "The negative piezoelectric effect of the ferroelectric polymer poly(vinylidene fluoride)," *Nature Materials*, vol. 15, no. 1, pp. 78–84, 2016.
- [29] P. Martins, A. C. Lopes, and S. Lanceros-Mendez, "Electroactive phases of poly(vinylidene fluoride): Determination, processing and applications," *Progress in Polymer Science*, vol. 39, no. 4, pp. 683–706, 2014.
- [30] C. Dias, D. K. Das-Gupta, Y. Hinton, and R. J. Shuford, "Polymer/ceramic composites for piezoelectric sensors," *Sensors and Actuators: A. Physical*, vol. 37-38, no. C, pp. 343–347, 1993.
- [31] A. Peláiz-Barranco and P. Marin-Franch, "Piezo-, pyro-, ferro-, and dielectric properties of ceramic/polymer composites obtained from two modifications of lead titanate," *Journal of Applied Physics*, vol. 97, no. 3, p. 034104, 2005.
- [32] G. Sa-Gong, A. Safari, S. J. Jang, and R. E. Newnham, "Poling flexible piezoelectric composites," *Ferroelectrics Letters Section*, vol. 5, no. 5, pp. 131–142, 1986.
- [33] R. Newnham, D. Skinner, and L. Cross, "Connectivity and piezoelectric-pyroelectric composites," *Materials Research Bulletin*, vol. 13, pp. 525–536, 1978.
- [34] D. A. van den Ende, S. E. van Kempen, X. Wu, W. A. Groen, C. A. Randall, and S. van Der Zwaag, "Dielectrophoretically structured piezoelectric composites with high aspect ratio piezoelectric particles inclusions," *Journal of Applied Physics*, vol. 111, no. 12, p. 124107, 2012.
- [35] H. Khanbareh, S. van Der Zwaag, and W. A. Groen, "Effect of dielectrophoretic structuring on piezoelectric and pyroelectric properties of lead titanate-epoxy composites," *Smart Materials and Structures*, vol. 23, no. 10, p. 105030, 2014.
- [36] N. K. James, D. B. Deutz, R. K. Bose, S. van der Zwaag, and P. Groen, "High Piezoelectric Voltage Coefficient in Structured Lead-Free (K,Na,Li)NbO₃ Particulate-Epoxy Composites," *Journal of the American Ceramic Society*, vol. 99, no. 12, pp. 3957–3963, 2016.
- [37] D. B. Deutz, N. T. Mascarenhas, J. B. J. Schelen, D. M. de Leeuw, S. van der Zwaag, and P. Groen, "Flexible Piezoelectric Touch Sensor by Alignment of Lead-Free Alkaline Niobate Microcubes in PDMS," *Advanced Functional Materials*, vol. 27, no. 24, p. 1700728, 2017.
- [38] V. L. Stuber, D. B. Deutz, J. Bennett, D. Cannell, D. M. de Leeuw, S. van der Zwaag, and P. Groen, "Flexible lead-free piezoelectric composite materials for energy harvesting applications," *Energy Technology*, vol. 7, pp. 177–185, 2019.

- [39] T. R. Mahon, V. L. Stuber, S. K. Ammu, S. van der Zwaag, P. Groen, T. Hoeks, and S. Guhathakurtha, "Flexible, printed, Pb-free piezo-composites for haptic feedback systems," in *IEEE International Symposium on Applications of Ferroelectrics (ISAF)*, pp. 1–4, IEEE, 2019.
- [40] H. Schlichting and K. Gersten, *Boundary-Layer Theory*. Springer, Berlin, Germany, 2017.
- [41] N. Mayrhofer and J. Woisetschlager, "Frequency analysis of turbulent compressible flows by laser vibrometry," *Experiments in Fluids*, vol. 31, no. 2, pp. 153–161, 2001.
- [42] A. P. Broeren and M. B. Bragg, "Flowfield measurements over an airfoil during natural low-frequency oscillations near stall," *AIAA Journal*, vol. 37, no. 1, pp. 130–132, 1999.
- [43] M. Gaster, "Laminar separation bubbles," In: *Govindarajan R. (eds) IUTAM Symposium on Laminar-Turbulent Transition, Fluid Mechanics and Its Applications*, vol. 78, 2006.
- [44] C. Mertens, C. C. Wolf, A. D. Gardner, F. F. Schrijer, and B. W. van Oudheusden, "Advanced infrared thermography data analysis for unsteady boundary layer transition detection," *Measurement Science and Technology*, vol. 31, no. 1, p. 015301, 2020.
- [45] C. Dollinger, M. Sorg, N. Balaesque, and A. Fischer, "Measurement uncertainty of IR thermographic flow visualization measurements for transition detection on wind turbines in operation," *Experimental Thermal and Fluid Science*, vol. 97, pp. 279–289, 2018.
- [46] A. D. Gardner, C. Eder, C. C. Wolf, and M. Raffel, "Analysis of differential infrared thermography for boundary layer transition detection," *Experiments in Fluids*, vol. 58, no. 9, p. 122, 2017.
- [47] S. Yarusevych and M. Kotsonis, "Steady and transient response of a laminar separation bubble to controlled disturbances," *Journal of Fluid Mechanics*, vol. 813, pp. 955–990, 2017.
- [48] F. Scarano, "Tomographic PIV: Principles and practice," *Measurement Science and Technology*, vol. 24, no. 1, p. 012001, 2013.
- [49] A. D. Gardner and K. Richter, "Boundary layer transition determination for periodic and static flows using phase-averaged pressure data," *Experiments in Fluids*, vol. 56, no. 6, p. 119, 2015.
- [50] ˆ. S. ˆzakmak, N. N. Sørensen, H. A. Madsen, and J. N. Sørensen, "Laminar-turbulent transition detection on airfoils by high-frequency microphone measurements," *Wind Energy*, vol. 22, no. 10, pp. 1356–1370, 2019.

- [51] F. Hausmann and W. Schröder, "Coated hot-film sensors for transition detection in cruise flight," *Journal of Aircraft*, vol. 43, no. 2, pp. 456–465, 2006.
- [52] H. Sturm, G. Dumstorff, P. Busche, D. Westermann, and W. Lang, "Boundary layer separation and reattachment detection on airfoils by thermal flow sensors," *Sensors (Switzerland)*, vol. 12, no. 11, pp. 14292–14306, 2012.
- [53] A. A. Haghiri, N. Fallahpour, M. Mani, and M. Tadjfar, "Experimental study of boundary layer in compressible flow using hot film sensors through statistical and qualitative methods," *Journal of Mechanical Science and Technology*, vol. 29, no. 11, pp. 4671–4679, 2015.
- [54] D. Roche, C. Richard, L. Eyraud, and C. Audoly, "Piezoelectric bimorph bending sensor for shear-stress measurement in fluid flow," *Sensors and Actuators, A: Physical*, vol. 55, no. 2-3, pp. 157–162, 1996.
- [55] K. Liu, W. Yuan, J. Deng, B. Ma, and C. Jiang, "Detecting boundary-layer separation point with a micro shear stress sensor array," *Sensors and Actuators, A: Physical*, vol. 139, no. 1-2 SPEC. ISS., pp. 31–35, 2007.
- [56] B. V. Oudheusden, *Integrated Silicon Flow Sensors*. PhD thesis, Delft University of Technology, Delft, the Netherlands, 1992.
- [57] V. L. Stuber, T. R. Mahon, S. van der Zwaag, and P. Groen, "The effect of the intrinsic electrical matrix conductivity on the piezoelectric charge constant of piezoelectric composites," *Materials Research Express*, vol. 7, p. 015703, 2019.
- [58] V. L. Stuber, M. Kotsonis, and S. van der Zwaag, "Boundary layer state detection using piezoelectric sensors," *Submitted to Smart Materials and Structures*, 2021.
- [59] V. L. Stuber, T. Mkhoyan, R. De Breuker, and S. van der Zwaag, "In-situ boundary layer transition detection on multi-segmental (a)synchronous morphing wings," *Submitted to AIAA Journal*, 2021.
- [60] C. R. Bowen, H. A. Kim, P. M. Weaver, and S. Dunn, "Piezoelectric and ferroelectric materials and structures for energy harvesting applications," *Energy and Environmental Science*, vol. 7, no. 1, pp. 25–44, 2014.
- [61] T. Rödiger, A. Schönecker, and G. Gerlach, "A survey on piezoelectric ceramics for generator applications," *Journal of the American Ceramic Society*, vol. 93, no. 4, pp. 901–912, 2010.
- [62] S. P. Beeby, M. J. Tudor, and N. M. White, "Energy harvesting vibration sources for microsystems applications," *Measurement Science and Technology*, vol. 17, no. 12, pp. 175–195, 2006.
- [63] D. B. Deutz, N. T. Mascarenhas, S. van der Zwaag, and W. A. Groen, "Enhancing energy harvesting potential of (K,Na,Li)NbO₃-epoxy composites via Li substitution," *Journal of the American Ceramic Society*, vol. 100, no. 3, pp. 1108–1117, 2017.

- [64] D. B. Deutz, J.-A. Pascoe, B. Schelen, S. van der Zwaag, D. M. de Leeuw, and P. Groen, "Analysis and experimental validation of the figure of merit for piezoelectric energy harvesters," *Materials Horizons*, vol. 5, pp. 444–453, 2018.
- [65] M. C. Araújo, C. M. Costa, and S. Lanceros-Méndez, "Evaluation of dielectric models for ceramic/polymer composites: Effect of filler size and concentration," *Journal of Non-Crystalline Solids*, vol. 387, pp. 6–15, 2014.
- [66] G. Rujijanagul, S. Jompruan, and A. Chaipanich, "Influence of graphite particle size on electrical properties of modified PZT-polymer composites," *Current Applied Physics*, vol. 8, no. 3-4, pp. 359–362, 2008.
- [67] H. Gong, Y. Zhang, J. Quan, and S. Che, "Preparation and properties of cement based piezoelectric composites modified by CNTs," *Current Applied Physics*, vol. 11, no. 3, pp. 653–656, 2011.
- [68] N. Jayasundere and B. V. Smith, "Dielectric constant for binary piezoelectric 0-3 composites," *Journal of Applied Physics*, vol. 73, no. 5, pp. 2462–2466, 1993.
- [69] N. Jayasundere, B. V. Smith, and J. R. Dunn, "Piezoelectric constant for binary piezoelectric 0-3 connectivity composites and the effect of mixed connectivity," *Journal of Applied Physics*, vol. 76, no. 5, pp. 2993–2998, 1994.
- [70] D. A. van den Ende, W. A. Groen, and S. Van Der Zwaag, "The effect of calcining temperature on the properties of 0-3 piezoelectric composites of PZT and a liquid crystalline thermosetting polymer," *Journal of Electroceramics*, vol. 27, no. 1, pp. 13–19, 2011.
- [71] Z. Wang, J. Keith Nelson, H. Hillborg, S. Zhao, and L. S. Schadler, "Dielectric constant and breakdown strength of polymer composites with high aspect ratio fillers studied by finite element models," *Composites Science and Technology*, vol. 76, pp. 29–36, 2013.
- [72] Ceramtec, *Datasheet Ceramtec soft PZT*. <https://www.ceramtec.com/ceramic-materials/soft-pzt>, accessed 25-03-2019.
- [73] Epoxy Technology Inc., *Epoxy Epotek 302-3M TDS*. <https://www.epotek.com/site/>, accessed 25-03-2019.
- [74] Smooth-on Inc., *PU Crystal Clear 202 TDS*. <https://www.smooth-on.com/>, accessed 25-03-2019.
- [75] D. B. Deutz, N. T. Mascarenhas, S. van der Zwaag, and W. A. Groen, "Poling piezoelectric (K,Na,Li)NbO₃ -polydimethylsiloxane composites," *Ferroelectrics*, vol. 515, no. 1, pp. 68–74, 2017.
- [76] A. F. Barzegar, D. Damjanovic, and N. Setter, "The effect of boundary conditions and sample aspect ratio on apparent d_{33} piezoelectric coefficient determined by direct quasistatic method," *Ultrasonics, Ferroelectrics and Frequency Control, IEEE Transactions on*, vol. 51, no. 3, pp. 262–270, 2004.

- [77] T. Zangina, J. Hassan, K. A. Matori, R. S. Azis, U. Ahmadu, and A. See, "Sintering behavior, ac conductivity and dielectric relaxation of $\text{Li}_{1.3}\text{Ti}_{1.7}\text{Al}_{0.3}(\text{PO}_4)_3$ NASICON compound," *Results in Physics*, vol. 6, pp. 719–725, 2016.
- [78] Y. Xu, *Ferroelectric Materials and Their Applications*. North Holland Elsevier Sci.Publ., Amsterdam, the Netherlands, 1991.
- [79] T. Yamada, T. Ueda, and T. Kitayama, "Piezoelectricity of a high-content lead zirconate titanate/polymer composite," *Journal of Applied Physics*, vol. 53, no. 6, pp. 4328–4332, 1982.
- [80] M. Wahbah, M. Alhawari, B. Mohammad, H. Saleh, and M. Ismail, "Characterization of human body-based thermal and vibration energy harvesting for wearable devices," *IEEE Journal on Emerging and Selected Topics in Circuits and Systems*, vol. 4, no. 3, pp. 354–363, 2014.
- [81] H. Abdi, N. Mohajer, and S. Nahavandi, "Human passive motions and a user-friendly energy harvesting system," *Journal of Intelligent Material Systems and Structures*, vol. 25, no. 8, pp. 923–936, 2014.
- [82] C. H. Wong, Z. Dahari, A. Abd Manaf, and M. A. Miskam, "Harvesting raindrop energy with piezoelectrics: A review," *Journal of Electronic Materials*, vol. 44, no. 1, pp. 13–21, 2015.
- [83] H. A. Sodano, D. J. Inman, and G. Park, "A review of power harvesting from vibration using piezoelectric materials," *Shock and Vibration Digest*, vol. 36, no. 3, pp. 197–205, 2004.
- [84] K. a. Cook-Chennault, N. Thambi, M. a. Bitetto, and E. Hameyie, "Piezoelectric Energy Harvesting: A Green and Clean Alternative for Sustained Power Production," *Bulletin of Science, Technology and Society*, vol. 28, no. 6, pp. 496–509, 2008.
- [85] H. Li, C. Tian, and Z. D. Deng, "Energy harvesting from low frequency applications using piezoelectric materials," *Applied Physics Reviews*, vol. 1, no. 4, p. 041301, 2014.
- [86] R. A. Islam and S. Priya, "Realization of high-energy density polycrystalline piezoelectric ceramics," *Applied Physics Letters*, vol. 88, no. 3, p. 032903, 2006.
- [87] D. A. van den Ende, B. F. Bory, W. A. Groen, and S. van der Zwaag, "Improving the d_{33} and g_{33} properties of 0-3 piezoelectric composites by dielectrophoresis," *Journal of Applied Physics*, vol. 107, no. 2, p. 024107, 2010.
- [88] D. Y. Wang, K. Li, and H. L. W. Chan, "High frequency 1-3 composite transducer fabricated using sol-gel derived lead-free BNBT fibers," *Sensors and Actuators, A: Physical*, vol. 114, no. 1, pp. 1–6, 2004.
- [89] A. Abrar, D. Zhang, B. Su, T. W. Button, K. J. Kirk, and S. Cochran, "1-3 Connectivity piezoelectric ceramic-polymer composite transducers made with viscous polymer processing for high frequency ultrasound," *Ultrasonics*, vol. 42, no. 1-9, pp. 479–484, 2004.

- [90] C. P. Bowen, R. E. Newnham, and C. A. Randall, "Particulate-Polymer Composites," *Journal of Materials Research*, vol. 13, pp. 205–210, 1998.
- [91] T. Furukawa, K. Fujino, and E. Fukada, "Electromechanical properties in the composites of epoxy resin and PZT ceramics," *Japanese Journal of Applied Physics*, vol. 15, no. 11, pp. 2119–2129, 1976.
- [92] S. A. Wilson, G. M. Maistros, and R. W. Whatmore, "Structure modification of 0-3 piezoelectric ceramic/polymer composites through dielectrophoresis," *Journal of Physics D: Applied Physics*, vol. 38, no. 2, pp. 175–182, 2005.
- [93] N. D. Spencer and J. H. Moore, *Encyclopedia of chemical physics and physical chemistry*. Institute of physics, Bristol, United Kingdom, 2001.
- [94] M. A. Gutiérrez, H. Khanbareh, and S. Van Der Zwaag, "Computational modeling of structure formation during dielectrophoresis in particulate composites," *Computational Materials Science*, vol. 112, pp. 139–146, 2016.
- [95] K. Han, A. Safari, and R. E. Riman, "Colloidal Processing for Improved Piezoelectric Properties of Flexible 0-3 Ceramic-Polymer Composites," *Journal of the American Ceramic Society*, vol. 74, no. 7, pp. 1699–1702, 1991.
- [96] SmartMaterial, *Datasheet Smart Material 1-3 Composites*. <https://www.smart-material.com/Datasheets.html>, accessed 16-04-2018.
- [97] Piezotech, *Datasheet Piezotech PVDF*. <https://www.piezotech.eu/en/Technical-center/Documentation/>, accessed 16-04-2018.
- [98] H. Du, Z. Li, F. Tang, S. Qu, Z. Pei, and W. Zhou, "Preparation and piezoelectric properties of $(K_{0.5}Na_{0.5})NbO_3$ lead-free piezoelectric ceramics with pressure-less sintering," *Materials Science and Engineering B: Solid-State Materials for Advanced Technology*, vol. 131, no. 1-3, pp. 83–87, 2006.
- [99] A. V. Popov, R. M. Botez, and M. Labib, "Transition Point Detection from the Surface Pressure Distribution for Controller Design," *Journal of Aircraft*, vol. 45, no. 1, pp. 23–28, 2008.
- [100] B. Sun, B. Ma, P. Wang, J. Luo, J. Deng, and C. Gao, "High sensitive flexible hot-film sensor for measurement of unsteady boundary layer flow," *Smart Materials and Structures*, vol. 29, no. 3, p. 035023, 2020.
- [101] B. Sun, P. Wang, J. Luo, J. Deng, S. Guo, and B. Ma, "A flexible hot-film sensor array for underwater shear stress and transition measurement," *Sensors*, vol. 18, no. 10, p. 3469, 2018.
- [102] C. Ghouila-Houri, A. Talbi, R. Viard, Q. Gallas, E. Garnier, A. Merlen, and P. Pernod, "High temperature gradient micro-sensors array for flow separation detection and control," *Smart Materials and Structures*, vol. 28, no. 12, p. 125003, 2019.

- [103] M. Drela, "Implicit Implementation of the Full e^n Transition Criterion," *AIAA Journal Applied Aerodynamics Conference*, no. June, 2003.
- [104] S. Mittal and P. Saxena, "Hysteresis in flow past a NACA 0012 airfoil," *Computer Methods in Applied Mechanics and Engineering*, vol. 191, no. 19-20, pp. 2207–2217, 2002.
- [105] F. M. White, *Viscous Fluid Flow*. McGraw-Hill, New York, United States, 2006.
- [106] M. Gad-el Hak, "Flow control: The future," *Journal of Aircraft*, vol. 38, no. 3, pp. 402–418, 2001.
- [107] Y. Zhang, X. Fang, H. Chen, S. Fu, Z. Duan, and Y. Zhang, "Supercritical natural laminar flow airfoil optimization for regional aircraft wing design," *Aerospace Science and Technology*, vol. 43, pp. 152–164, 2015.
- [108] L. Cortelezzi, K. H. Lee, J. Kim, and J. L. Speyer, "Skin-friction drag reduction via robust reduced-order linear feedback control," *International Journal of Computational Fluid Dynamics*, vol. 11, no. 1-2, pp. 79–92, 1998.
- [109] A. Abbas, G. Bugeda, E. Ferrer, S. Fu, J. Periaux, J. Pons-Prats, E. Valero, and Y. Zheng, "Drag reduction via turbulent boundary layer flow control," *Science China Technological Sciences*, vol. 60, no. 9, pp. 1281–1290, 2017.
- [110] S. Grundmann and C. Tropea, "Active cancellation of artificially introduced Tollmien-Schlichting waves using plasma actuators," *Experiments in Fluids*, vol. 44, no. 5, pp. 795–806, 2008.
- [111] H. J. Tol, C. C. De Visser, and M. Kotsonis, "Experimental model-based estimation and control of natural Tollmien-Schlichting waves," *AIAA Journal*, vol. 57, no. 6, pp. 2344–2355, 2019.
- [112] V. Kumar, M. Hays, E. Fernandez, W. Oates, and F. S. Alvi, "Flow sensitive actuators for micro-air vehicles," *Smart Materials and Structures*, vol. 20, no. 10, p. 105033, 2011.
- [113] M. Kotsonis, R. K. Shukla, and S. Pröbsting, "Control of natural Tollmien-schlichting waves using dielectric barrier discharge plasma actuators," *International Journal of Flow Control*, vol. 7, no. 1-2, pp. 37–54, 2015.
- [114] R. Merino-Martínez, A. Rubio Carpio, L. T. Lima Pereira, S. van Herk, F. Avallone, D. Ragni, and M. Kotsonis, "Aeroacoustic design and characterization of the 3D-printed, open-jet, anechoic wind tunnel of Delft University of Technology," *Applied Acoustics*, vol. 170, p. 107504, 2020.
- [115] A. Sciacchitano, D. R. Neal, B. L. Smith, S. O. Warner, P. P. Vlachos, B. Wieneke, and F. Scarano, "Collaborative framework for PIV uncertainty quantification: Comparative assessment of methods," *Measurement Science and Technology*, vol. 26, no. 7, p. 074004, 2015.

- [116] P. D. Welch, "The use of Fast fourier transform for the estimation of power spectra: a method based on time averaging over short, modified periodograms," *IEEE Transactions on Audio and Electroacoustics*, vol. 15, pp. 70–73, 1967.
- [117] A. Concilio, I. Dimino, L. Lecce, and R. Pecora, *Morphing wing technologies: Large commercial aircraft and civil helicopters*. Butterworth-Heinemann, Oxford, United Kingdom, 2017.
- [118] B. Perry III, S. Cole, and G. Miller, "A summary of the active flexible wing program," *NASA Technical Memorandum*, vol. NASA/TM-19, 1992.
- [119] K. L. Bonnema and W. A. Lokos, "AFTI/F-111 mission adaptive wing flight test instrumentation overview," in *Proceedings of the ISA Aerospace Instrumentation Symposium*, vol. 35, pp. 809–840, 1989.
- [120] B. Sanders, R. Crowe, and E. Garcia, "Defense advanced research projects agency - Smart materials and structures demonstration program overview," *Journal of Intelligent Material Systems and Structures*, vol. 15, no. 4, pp. 227–233, 2004.
- [121] A.-M. McGowan, L. Horta, J. Harrison, and D. Raney, "Research activities within NASA's morphing program," in *Research and Technology Agence*, 1999.
- [122] A.-M. McGowan, A. Washburn, L. Horta, R. Bryant, D. Cox, E. Siochi, S. Padula, and N. Holloway, "Recent results from NASA's morphing project," in *Proceedings of the SPIE Conference on Smart Structures and Materials*, pp. 97–111, 2002.
- [123] A. De Gaspari, L. Riccobene, and S. Ricci, "Design, manufacturing and wind tunnel validation of a morphing compliant wing," *Journal of Aircraft*, vol. 55, no. 6, pp. 2313–2326, 2018.
- [124] A. Ciarella, C. Tsotskas, M. Hahn, N. P. Werter, R. De Breuker, C. S. Beaverstock, M. I. Friswell, Y. Yang, S. Özgen, A. Antoniadis, P. Tsoutsanis, and D. Drikakis, "A multi-fidelity, multi-disciplinary analysis and optimization framework for the design of morphing UAV wings," *16th AIAA/ISSMO Multidisciplinary Analysis and Optimization Conference*, no. June, 2015.
- [125] H. Pfeiffer and M. Wevers, "The European project "Aircraft integrated structural health assessment II"," in *Innovation for Sustainable Aviation in a Global Environment: Proceedings of the Sixth European Aeronautics Days, Madrid*, 2012.
- [126] P. Wölcken and M. Papadopoulos, *Smart intelligent aircraft structures (SARISTU): proceedings of the final project conferece*. Springer, Cham, Switzerland, 2015.
- [127] T. A. Weisshaar, "Morphing aircraft systems: Historical perspectives and future challenges," *Journal of Aircraft*, vol. 50, no. 2, pp. 337–353, 2013.
- [128] D. Li, S. Zhao, A. Da Ronch, J. Xiang, J. Drofelnik, Y. Li, L. Zhang, Y. Wu, M. Kintscher, H. P. Monner, A. Rudenko, S. Guo, W. Yin, J. Kirn, S. Storm, and R. D. Breuker, "A review of modelling and analysis of morphing wings," *Progress in Aerospace Sciences*, vol. 100, no. September 2017, pp. 46–62, 2018.

- [129] I. Chopra, "Review of state of art of smart structures and integrated systems," *AIAA Journal*, vol. 40, no. 11, pp. 2145–2187, 2002.
- [130] R. G. Loewy, "Recent developments in smart structures with aeronautical applications," *Smart Materials and Structures*, vol. 6, no. 5, pp. 11–42, 1997.
- [131] N. Nguyen, S. Lebofsky, E. Ting, U. Kaul, D. Chaparro, and J. Urnes, "Development of variable camber continuous trailing edge flap for performance adaptive aeroelastic wing," in *SAE Technical paper*, 2015.
- [132] "CS-25 Large Aeroplanes," tech. rep., European Union Aviation Safety Agency, 2008.
- [133] T. Mkhoyan, N. R. Thakrar, R. D. Breuker, and J. Sodja, "Design and development of a seamless smart morphing wing using distributed trailing edge camber morphing for active control," *AIAA Scitech 2021 Forum*, no. January, 2021.
- [134] N. P. Werter, J. Sodja, G. Spirlet, and R. De Breuker, "Design and experiments of a warp induced camber and twist morphing leading and trailing edge device," *24th AIAA/AHS Adaptive Structures Conference*, no. January, 2016.
- [135] N. Nazeer, R. M. Groves, and R. Benedictus, "Simultaneous position and displacement sensing using two fibre Bragg grating sensors," in *Proceedings of SPIE*, no. March 2019, 2019.
- [136] T. Mkhoyan, C. C. de Visser, and R. De Breuker, "Adaptive real-time clustering method for dynamic visual tracking of very flexible wings," *Journal of Aerospace Information Systems*, vol. 18, no. 2, pp. 58–79, 2021.
- [137] T. Mkhoyan, C. de Visser, and R. D. Breuker, "Adaptive state estimation and real-time tracking of aeroelastic wings with augmented kalman filter and kernelized correlation filter," *AIAA Scitech 2021 Forum*, 2021.
- [138] MultiSIM, *multiSIM: Distributed simulation D-SIM*. <https://multisim.nl/d-sim/>, accessed 18-09-2020.
- [139] Atmel, *IDiSI-B Optical Distributed Sensor Interrogator*. <http://ww1.microchip.com/>, accessed 18-09-2020.
- [140] X. Wang, E. Van Kampen, Q. P. Chu, and R. De Breuker, "Flexible aircraft gust load alleviation with incremental nonlinear dynamic inversion," *Journal of Guidance, Control, and Dynamics*, vol. 42, no. 7, pp. 1519–1536, 2019.
- [141] M. Fujino, Y. Yoshizaki, and Y. Kawamura, "Natural-laminar-flow airfoil development for a lightweight business jet," *Journal of Aircraft*, vol. 40, no. 4, pp. 609–615, 2003.
- [142] T. M. Young, B. Humphreys, and J. P. Fielding, "Investigation of hybrid laminar flow control (HLFC) surfaces," *Aircraft Design*, vol. 4, no. 2-3, pp. 127–146, 2001.

- [143] A. Y. Sofla, S. A. Meguid, K. T. Tan, and W. K. Yeo, "Shape morphing of aircraft wing: Status and challenges," *Materials and Design*, vol. 31, no. 3, pp. 1284–1292, 2010.
- [144] D. Coutu, V. Brailovski, and P. Terriault, "Optimized design of an active extrados structure for an experimental morphing laminar wing," *Aerospace Science and Technology*, vol. 14, no. 7, pp. 451–458, 2010.
- [145] G. E. Fujiwara and N. T. Nguyen, "Aerostructural design optimization of a subsonic wing with continuous morphing trailing edge," *35th AIAA Applied Aerodynamics Conference, 2017*, no. June, 2017.
- [146] T. L. Grigorie, R. M. Botez, and A. V. Popov, "Self-adaptive morphing wing model, smart actuated and controlled by using a multiloop controller based on a laminar flow real time optimizer," *24th AIAA/AHS Adaptive Structures Conference*, no. January, 2016.
- [147] A. Koreanschi, O. Sugar-Gabor, and R. M. Botez, "Drag optimisation of a wing equipped with a morphing upper surface," *Aeronautical Journal*, vol. 120, no. 1225, pp. 473–493, 2016.
- [148] T. Mkhoyan, N. R. Thakrar, R. de Breuker, and J. Sodja, "Design of a smart morphing wing using integrated and distributed trailing edge camber morphing," *ASME 2020 Conference on Smart Materials, Adaptive Structures and Intelligent Systems, SMASIS 2020*, no. September, 2020.
- [149] A. Deperrois, "Analysis of foils and wings operating at low Reynolds numbers," *Guidelines for XFLR5*, 2009.
- [150] J. D. Anderson, *Introduction to Flight*. McGraw-Hill, New York, United States, 2016.

ACKNOWLEDGEMENTS

For four years I have been working in this thesis, and during that time a lot of people have made it possible for me to bring it to a successful end. Here, I like to thank those people.

First and above all, I would like to thank my initial first promotor Pim Groen. You were the one to offer me a PhD position. Because I already got to know you during my master's graduation project, I was certain that I would have a great time working for you once again. You were a motivating supervisor to have, always had time for questions and discussions, and brought fun and exciting ideas to try ourselves in the labs. Besides the professional relation we had, we also have had various occasions for a beer (preferably not a basic lager), conversations about your cats, or mandatory slide-shows with pictures of your latest vacation. While you are the person responsible for the start of my journey as PhD candidate, you are sadly not able to see it end. I know you are deeply missed by me and the other NovAM members who have worked with you. In short, thank you Pim for being part of my journey.

Sybrand van der Zwaag, while you were already my promotor before Pim passed away, our relation fundamentally changed when you became my first promotor. I want to express my deepest respect and thanks for the way you helped me in bringing my work to the highest possible level. Your insights, critical thinking, second guessing, high level of feedback and fast responses never cease to amaze me. I believe that a great deal of the growth I have experienced over the last years I owe to you. For all of this, you have my deepest thanks.

Roeland De Breuker, you stepped in as my second promotor which I am grateful for. Your aerospace background was a valuable addition to this work, as your different approaches and way of thinking (compared to the NovAM group) have made this thesis a more complete piece of work. In addition I would like to thank you for taking on the role as the head of the SmartX project. I believe this was of vital importance for the success of the project.

Staying on topic of the SmartX project, I would like to thank Tigran Mkhoyan, Nakash Nazeer, Sherry Wang, Irèn Mkhoyan, Nisarg Thakrar, Jurij Sodja and Roger Groves for their contributions in bringing the project to a successful end. In particular Tigran, while at the start we did not always agree with one another and even had a fair share of conflict, I feel like we grew out to be good colleagues with nothing but respect for each other. In addition, I also want to thank Martin Weberschock for one of the most crucial parts of the project: helping us build the SmartX wing. Your patience and experience made it possible for us to manufacture such a complex wing.

Ben Schelen, you have proven to be a vital connection throughout the years to various PhD students of the piezo-group, and were indispensable for the development of the piezoelectric sensors of this work. Thank you for the numerous times you traveled to Delft, for explaining to me how piezoelectric materials work from an electronics point of view, and your assistance in multiple wind tunnel experiments.

Dago de Leeuw, I am glad I got to work with you for about a year time. My first publication was in collaboration with you, and I owe you a big thanks for your lessons on technical writing and your advice on handling reviewer responses. Our discussions about piezoelectric composites really brought my understanding of the subject to the next level.

Daniella Deutz, this acknowledgement would not be complete without you being mentioned in it. Back in the day, Pim tricked us both into believing that I specifically asked for you to be my daily supervisor, while I did not even know you existed. However, I am glad he did, because I enjoyed working with you each day again. You got me into the topic of piezoelectric materials, and I decided to stay. Thank you for planting the seed.

Many more people at the TUD made it possible to finish this thesis. Shanta Visser, thank you for helping me with numerous organizational tasks. Leo Veldhuis, thank you for multiple brainstorm sessions in the initial phase of the project. Marios Kotsonis, thank you for extensive help with the PIV wind tunnel experiments and the publication that came out of it. I also would like to thank Frans, Durga, Berthil, Marlies, Johan and all others from the ASM laboratory for their help throughout the years.

Satya Ammu and Gawel Kus, besides a couple of temporary colleagues, you two have been my main office mates. With both of you I was able to have a laugh on a daily basis, and thus I can easily say that I enjoyed your company very much. I wish both of you the best of luck in finishing your own thesis. Hopefully I can act as some sort of example to you.

While the research topic should be the main drive behind a thesis, another reason I enjoyed my work so much was because of the group I got to do my work in: the NovAM group. I will never forget the Friday afternoons at our faculty bar, de Atmosfeer, which more than once resulted in long nights of fun. In addition, I was able to enjoy our coffee breaks and lunches on a daily basis. Thank you Anton, Dimos, Gawel, Hugo, Jingjing, Mariana, Paul, Satya, Tadhg, Vincenzo, Yifan, and many more of the earlier generation, for making the NovAM group unforgettable.

In addition to the people bound to the university, I also would like to thank my parents, Marjolein and Rolant. Marjolein, you have always believed that I was destined to work as a scientist, far before I even believed I wanted or could do that. Rolant, your own aerospace background and general interest in science clearly made an impact on me.

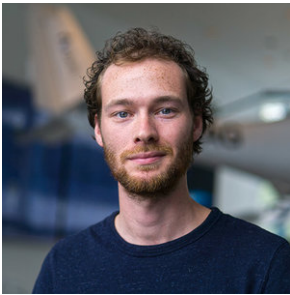
The two of you therefore made it possible for this thesis (and me!) to exist.

Finally, Rosa, I would like to thank you too. Over the last four years we started to live together, took a cat (which felt like a big step to me), and only continued to grow together. Together we created a place to call home; a place where I was able to recharge myself daily in order to get back to work again the next day for four years long. While a home is generally defined as a place, I would certainly also define it as people. Thank you Rosa for being my home.



CURRICULUM VITÆ

Vincent Leo STUBER

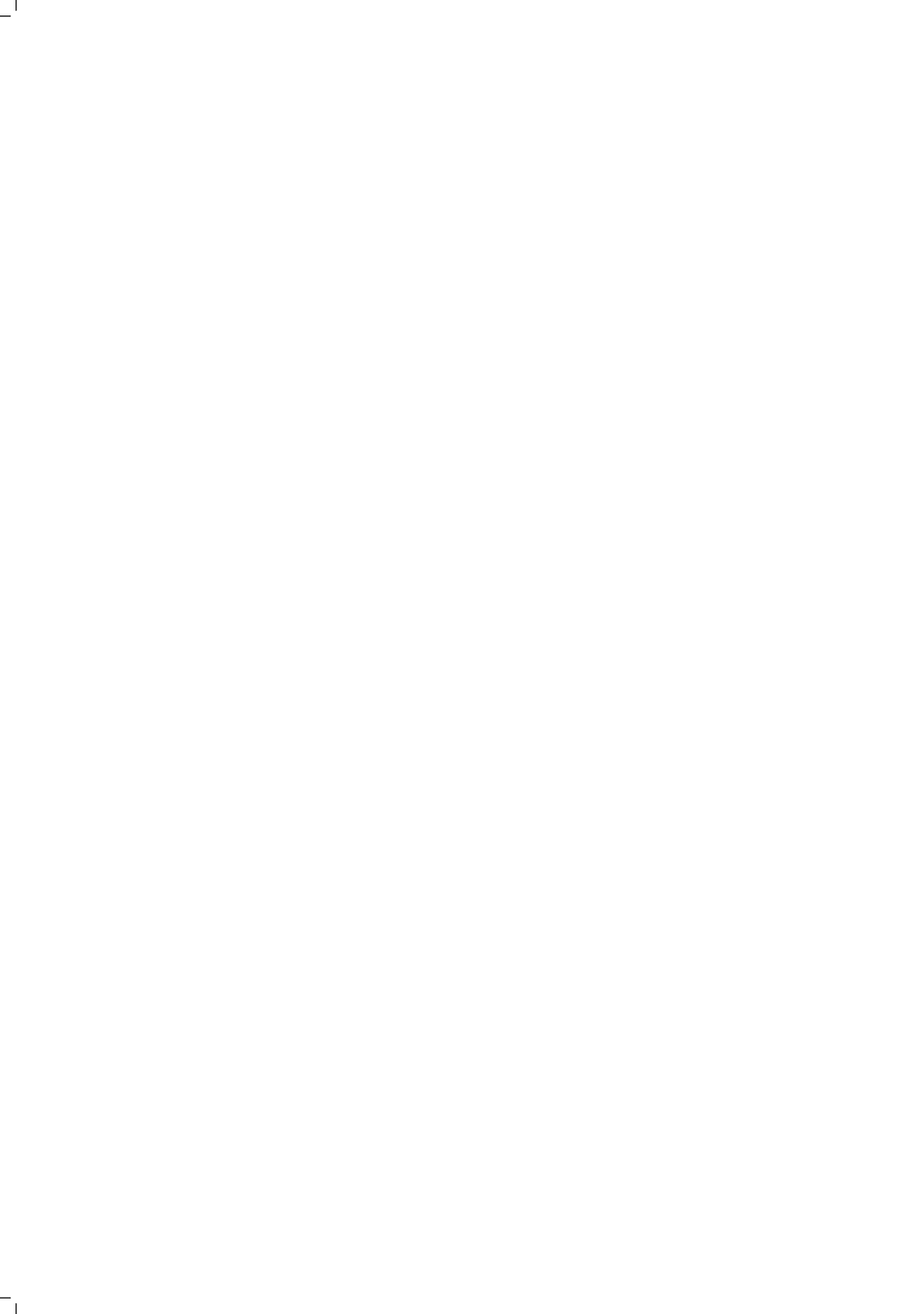


I was born on the 8th of February 1989 and grew up in Amersfoort, the Netherlands. In 2012 I obtained my BSc degree Aviation Studies at the Amsterdam University of Applied Sciences. I decided to pursue a MSc degree at the Delft University of Technology at the faculty of Aerospace Engineering. Before I could start my master's education, I had to pass a bridging year. During that time I got introduced to Materials Sciences, and got interested in this field. This sudden interest which was triggered in me got to me by total surprise. I therefore decided to take a leap of faith,

and specialize in this direction. I never regretted this decision.

In 2014 I moved to Delft, and started my master's in the Aerospace Structures and Materials (ASM) track, within the Novel Aerospace Materials (NovAM) profile. I performed my graduation project in 2016 under supervision of Prof. dr. Pim Groen, working on piezoelectric composites. I graduated in 2017 presenting my MSc thesis entitled *Lead-free Piezoelectric Composites for Energy Harvesting Applications*. Although I spent about nine months on my master thesis, I felt like I only scratched the surface of the topic. I therefore decided to accept the generous offer made by my professor to stay as a PhD candidate.

In the same year, 2017, I therefore started on my doctoral trajectory initially under supervision of Prof. dr. Pim Groen and Prof. dr. ir. Sybrand van der Zwaag. Sadly, halfway through my PhD Pim Groen passed away, and Dr. ir. Roeland De Breuker became my second supervisor. The topic of my work was about introducing piezoelectric materials into the *SmartX* morphing wing. This was a joint project involving two other PhD candidates funded by the university itself. The aim was to develop a morphing wing with integrated smart sensing technologies. During the project, we traveled to Gleichen, Germany, in order to build the wing with the help of Martin Weberschock. In the summer of 2020 we were able to finish the wing and experimentally put it to the test in one of the wind tunnels of the university. As a finishing milestone, we were able to win the Best Student Hardware Competition at the American conference on Smart Materials, Adaptive Structures and Intelligent Systems (SMASIS) 2020, using our *SmartX* wing as hardware demonstrator.



LIST OF PUBLICATIONS

JOURNAL PUBLICATIONS

7. **V. L. Stuber**, T. Mkhoyan, R. De Breuker and S. van der Zwaag
In-situ transition detection on multi-segmental (a)synchronous morphing wings
Submitted to Measurement: Sensors, (2021)
6. T. Mkhoyan, X. Wang, I. Mkhoyan, **V. L. Stuber** and R. De Breuker
Bio-inspired distributed and decentralized real-time control and sensing architecture for a seamless active morphing wing
To be submitted
5. **V. L. Stuber**, M. Kotsonis and S. van der Zwaag
Boundary layer state detection using piezoelectric sensors
Smart Materials and Structures, (2021), *under review*
4. R. De Breuker, T. Mkhoyan, N. Nazeer, **V. L. Stuber**, R. M. Groves, S. van der Zwaag and J. Sodja
Overview of the SmartX wing technology integrator
Submitted to AIAA Journal, (2021)
3. T. R. Mahon, **V. L. Stuber**, S. K. Ammu, S. van der Zwaag, P. Groen, T. Hoeks and S. Guhathakurtha
Flexible, printable, Pb-free piezo-composites for haptic feedback systems
2019 IEEE International Symposium on Applications of Ferroelectrics, ISAF 2019 - Proceedings, (2019)
2. **V. L. Stuber**, T. R. Mahon, S. van der Zwaag and P. Groen
The effect of the intrinsic electrical matrix conductivity on the piezoelectric charge constant of piezoelectric composites
Materials Research Express 7, 1-14 (2019)
1. **V. L. Stuber**, D. B. Deutz, J. Bennett, D. Cannel, D. M. de Leeuw, S. van der Zwaag and P. Groen
Flexible lead-free piezoelectric composite materials for energy harvesting applications
Energy Technology 7, 177-185 (2019)

CONFERENCE CONTRIBUTIONS

5. **V. L. Stuber**, S. van der Zwaag and P. Groen
Oral presentation: *Boundary layer state detection on airfoils using piezoelectric sensors*
Conference on Smart Materials, Adaptive Structures and Intelligent Systems (SMASIS), Los Angeles, USA, September 2020
4. **V. L. Stuber**, T. R. Mahon, S. K. Ammu, A. Tuluk, S. van der Zwaag and P. Groen
Oral presentation: *Robust easily fabricated piezoelectric composite materials*
F²C π ² Joint Conference, Lausanne, Switzerland, September 2019

3. **V. L. Stuber**, T. R. Mahon, S. K. Ammu, D. Giannopolous, S. van der Zwaag and P. Groen
Oral presentation: *Flexible piezoelectric composite materials*
Nederlandse Keramische Vereniging (NKV), Delft, the Netherlands, April 2019
2. **V. L. Stuber**, D. M. de Leeuw, S. van der Zwaag and P. Groen
Oral presentation: *Flexible lead-free piezoelectric composites for energy harvesting applications*
Electroceramics XVI, Hasselt, Belgium, July 2018
1. **V. L. Stuber**, D. B. Deutz, S. van der Zwaag and P. Groen
Oral presentation: *Lead-free piezoelectric composites for energy harvesting applications*
Nederlandse Keramische Vereniging (NKV), Ermelo, the Netherlands, April 2017

AWARDS

3. **Best student hardware competition** for the SmartX wing demonstrator
SMASIS 2020 conference, Los Angeles, USA, 2020
2. **Best of Energy Technology 2019** for the paper: *Flexible lead-free piezoelectric composite materials for energy harvesting applications*
Energy Technology journal, 2019
1. **Best poster award** for the poster: *Piezoelectrics & energy harvesting*
Aerospace Engineering PhD event, Delft, the Netherlands, 2018

NOMENCLATURE

SYMBOLS

A	Signal amplitude between 100 Hz and 5000 Hz	[VHz]
A_d	Signal amplitude recorded to the database	[VHz]
A_{elec}	Electrode area	[m ²]
C_c	Capacitance of the cable	[F]
C_p	Capacitance of the piezoelectric element	[F]
C_r	Capacitance of the charge amplifier	[F]
\mathbf{D}	Dielectric displacement matrix	[Cm ⁻²]
\mathbf{d}	Piezoelectric charge constant matrix	[CN ⁻¹] or [mV ⁻¹]
d_{ij}	Piezoelectric charge constant (ij-direction)	[CN ⁻¹] or [mV ⁻¹]
d_{33f}	Piezoelectric charge constant of the filler (33-direction)	[CN ⁻¹] or [mV ⁻¹]
d_{33r}	Relative piezoelectric charge constant (33-direction)	[%]
\mathbf{E}	Electric field matrix	[Vm ⁻¹]
E	Electric field	[Vm ⁻¹]
E_{eff}	Electric field applied to the filler particles	[Vm ⁻¹]
F	Force	[N]
f	Frequency	[Hz]
g_{ij}	Piezoelectric voltage constant (ij-direction)	[VmN ⁻¹]
H	Shape factor	[-]
I_{sc}	Short circuit current	[A]
L	Chord length	[m]
P	Polarization	[Cm ⁻¹]
P_r	Remnant polarization	[Cm ⁻¹]
P_s	Saturated polarization	[Cm ⁻¹]
\overline{P}_2	Orientational order parameter	[-]
q_p	Charge generated by the piezoelectric element	[C]
R	Resistance	[Ω]
Re	Reynolds number	[-]
\mathbf{S}	Strain matrix	[-]
STD	Standard deviation	[-]
\mathbf{s}^E	Compliance matrix under constant electric field	[m ² N ⁻¹]

\mathbf{T}	Stress matrix	$[\text{Nm}^{-2}]$
T	Temperature	$[^{\circ}\text{C}]$
T_c	Curie temperature	$[^{\circ}\text{C}]$
t	Time	$[\text{s}]$
t_{disk}	Thickness of piezoelectric disk	$[\text{m}]$
$\tan(\delta)$	Dielectric loss	$[-]$ or $[\%]$
U_e	Boundary layer edge velocity	$[\text{ms}^{-1}]$
U_{in}	Input voltage	$[\text{V}]$
U_{oc}	Stored electrical energy per unit volume	$[\text{Wm}^{-3}]$
U_{out}	Output voltage	$[\text{V}]$
U_{∞}	Free stream velocity	$[\text{ms}^{-1}]$
u	Normalized velocity component (x -direction)	$[-]$
$u(x, y)$	Stream velocity	$[\text{ms}^{-1}]$
V	Voltage	$[\text{V}]$
V_{oc}	Open circuit voltage	$[\text{V}]$
v	Normalized velocity component (y -direction)	$[-]$
x/c	Position along the chord	$[-]$
x/c_{tr}	Location of transition	$[-]$
Z	Impedance	$[\Omega]$
α	Angle of attack	$[^{\circ}]$
α_{fit}	Fitted angle of attack found in the database	$[^{\circ}]$
α_{shift}	Difference between α and α_{fit}	$[^{\circ}]$
β	Angle between fiber chain and the surface normal	$[^{\circ}]$
δ	Morphing tip deflection	$[\text{m}]$
δ^*	Displacement thickness	$[\text{m}]$
δ_{fit}	Fitted morphing tip deflection found in the database	$[\text{m}]$
δ_{shift}	Difference between δ and δ_{fit}	$[\text{m}]$
ΔA	Difference between A and A_d per sensor	$[\text{VHz}]$
ΔA_{tot}	Difference between A and A_d per segment	$[\text{VHz}]$
ϵ^T	Permittivity matrix under constant stress	$[\text{Fm}^{-1}]$
ϵ^T	Permittivity under constant stress	$[\text{Fm}^{-1}]$
ϵ_f	Dielectric constant of the filler	$[-]$
ϵ_m	Dielectric constant of the matrix	$[-]$
ϵ_r	Relative permittivity, or dielectric constant	$[-]$
θ	Momentum thickness	$[\text{m}]$
ν	Kinematic viscosity	$[\text{m}^2\text{s}^{-1}]$
ρ_r	Relative density	$[\%]$
σ	Electric conductivity	$[\text{Sm}^{-1}]$
σ_m	Electric conductivity of the matrix	$[\text{Sm}^{-1}]$
φ	Volume fraction	$[-]$ or $[\%]$

ABBREVIATIONS

AAW	Active Aeroelastic Wing
AFW	Active Flexible Wing
BDS	Broadband Dielectric Spectrometer
BNT	Bismuth sodium titanate
BT	Barium titanate
CFRP	Carbon Fiber Reinforced Plastic
DARPA	Defense Advanced Research Projects Agency
EU	European Union
FBG	Fiber Bragg Grating
FFT	Fast Fourier Transform
FP	Framework Programmes
GFRP	Glass Fiber Reinforced Plastic
INDI	Incremental Nonlinear Dynamic Inversion
IR	Infrared
KNLN	Lithium doped potassium sodium niobate
KNN	Potassium sodium niobate
LE	Leading edge
LSB	Laminar Separation Bubble
MPB	Morphotropic Phase Boundary
NASA	National Aeronautics and Space Administration
OJF	Open Jet Facility
PDMS	Polydimethylsiloxane
PET	Polyethylene terephthalate
PIV	Particle Image Velocimetry
PLA	Polylactic acid
PPT	Polymorphing Phase Transition
PSD	Power Spectral Density
PT	Lead titanate
PU	Polyurethane
PVDF	Polyvinylidene-fluoride
PZT	Lead zirconate titanate
QP	Quadratic Programming
SARISTU	Smart Intelligent Aircraft Structures
SEM	Scanning Electron Microscope
SVHC	Substance of Very High Concern
TE	Trailing edge
TRIC	Translation Induced Camber
TRL	Technology Readiness Level
TUD	Delft University of Technology
VCCTEF	Variable Camber Continuous Trailing Edge Flap